Chair of Metal Forming
Department Product Engineering,
University of Leoben, Austria

MASTERS THESIS

On modelling the local damage evolution in hot work tool steels

Friedrich Krumphals

Materials Science G 970

Under supervision of Doz. Dr. Christof Sommitsch

June, 2007

I hereby declare that myself composed this thesis without any assistance from third parties. Furthermore, I confirm that no sources and resources have been used in the preparation of this thesis other than those indicated in the thesis itself. All references have been cited as appropriate.

Leoben, June 2007 Friedrich Krumphals

Acknowledgements

The present thesis was constructed at the Christian Doppler Laboratory for Materials Modelling and Simulation under supervision of Doz. Dr. Christof Sommitsch to whom I want to especially thank for expert support and always reachable and friendly cooperation when assistance was needed.

Many thanks to DI. Bernhard Buchner for an everytime quick trouble shooting in Latex, not even on workdays and encouraging words, which gave me the impression that he wants me to finish study as quickly as possible.

I also want to thank DI. Candic for start up tipps with Latex and funny amusement and suggestions during hard days, Albert for assistance with graphical matters as well as my other colleagues at the institute with them I always spent my improtant and sometimes extensive lunchtimes.

Thanks to my further material science colleagues at the other institutes for motivating one another to do exams and sporting activities made together. I want to especially thank my chinese collegue for motivation and showing me how to work intensively like a chinese when time is critical and the amusing advices therefore.

I also want to thank my grandparents who are always asking me when I'm going to finish, my parents who gave me the freedom to decide everything in my life by my own since the primary school, my younger brother and sister who activate my personal ambition to finish my study earlier within a certain time inbetween, my relatives and also our animals at home, which are a welcome relief to the habitual life.

And last but not least, looking into the future, I want to thank Doz. Dr. Christof Sommitsch for the leap of faith to perform a PhD-thesis under his supervision.

Abstract

Hot work tool steels are exposed to high temperatures and are additionally mechanically loaded. Suchlike cyclic load spectra with overlapping of thermal and mechanical loads cause different damage mechanisms, as caused by only time dependent creep or time independent fatigue mechanisms. This literature survey tasks with the microstructure of hot work tool steels in general, the change of the same at thermo-mechanical loads, and the resulting damage mechanisms. Using microstructure models, based on metal physics as well as plasticity models, damage can be described and lifetime, i.e. cycles to failure, can be calculated. Different approaches of microstructure and damage modelling as well as simulation, like crystal plasticity, cellular automata and the Monte Carlo method, are shown. Forward looking, in a PhD-thesis, hardening mechanisms, connected with an increase of dislocation density and softening processes, which influence the material properties, are going to be modelled by microplane and crystal plasticity methods.

Kurzfassung

Werkzeuge, eingesetzt für Warmumformprozesse, werden bei erhöhten Temperaturen beansprucht und sind zusätzlich mit mechanischen Lasten beaufschlagt. Aus zyklischen Lastkollektiven mit Überlagerung von thermischen und mechanischen Beanspruchungen resultieren andere Schädigungsverhalten als aus rein zeitabhängigem Kriechen oder zeitunabhängiger Ermüdungsbeanspruchung. Dieser Literaturüberblick beschäftigt sich mit der Mikrostruktur von Warmarbeitsstählen allgemein, der Änderung derselben im Einsatz, und den sich daraus ergebenden Schädigungsmechanismen. Mittels Mikrostrukturmodellen basierend auf metallpysikalischer Basis wie auch plastomechanischer Modelle kann diese Schädigung beschrieben und die Lebensdauer bzw. Anzahl der Zyklen bis zum Versagen berechnet werden. Verschiedene Ansätze zur Mikrostruktur- und Schädigungsmodellierung sowie zue Simulation, wie z.B. die Kristallplastizitätstheorie, zelluläre Automaten oder die Monte-Carlo Methode, werden vorgeschlagen. Zukünftig sollen in einer Dissertation Verfestigungsmechanismen, verbunden mit einer Steigerung der Versetzungsdichte und Entfestigungsmechanismen, welche die mechanischen Eigenschaften beeinflussen, mittels Schnittebenenverfahren und kristallplastischen Ansätzen modelliert werden.

Contents

List of Abbreviations

Abreviation	Meaning
AC	accumulation of creep damage
bcc	body centered cubic
CA	cellular automata
DCCW	diamond counter clockwise
DCW	diamond clockwise
EBSD	electro back scatter diffraction
e.g.	example given
Eq.	equation
fcc	face centered cubic
Fig.	figure
FMDF	frequency modified damage function
GND	geometrically necessary dislocations
HCF	high cycle fatigue
i.e.	that is
IMC	intermetallic compound
IMLP	incremental multiaxial life prediction law
IP	in phase
LCF	low cycle fatigue
LEDS	low energy dislocation structure
MC	metal carbide
MDA	multiaxial damage accumulation law
NLK	nonlinear kinematic hardening rule
NN	nearest neighbours
NNN	next nearest neighbours
OP	out of phase
PDF	probability density function
PVW	principal virtual work
SAGB	small angle tilt grain boundary
SRP	strain rate partitioning
SSD	secondary stored dislocations
TME	thermo-mechanical experiments
TVBO	thermoviscoplasticity based on overstress

List of Symbols

Symbol	*Meaning*	*Unit*
A	point	[-]
a	lattice parameter	[m]
A_0	constant	[1]
a_0	initial crack length	[m]
A_c	circular area	[m^2]
a_f	critical crack length	[m]
A_i	integral boundary	[-]
a_r	aspect ratio	[s^{-1}]
ΔA	surface element	[-]
B	point	[-]
b	Burgers vector	[m]
B_i	integral boundary	[-]
B_p	substitute grain boundary surface	[m^2]
b_s	summation index	[1]
c	fatigue ductility exponent	[1]
$^\circ C$	degree, celsius	[$^\circ C$]
$\mathbf{C}^{-1}$	compliance matrix	[1]
c_1, c_2	material parameters	[1]
C_i	damage variables	[1]
c_j^e	concentration of jogs in thermodynamic equilibrium	[m^{-3}]
C_k	kinetic constant	[1]
c_m	material parameter	[1]
C_ν	void volume fraction	[m^3]
D	diffusion coefficient	[m^2s^{-1}]
D_0	initial diffusion coefficient	[m^2s^{-1}]
$d_{annihil-c}$	critical distance for spontaneous annihilation	[m]
D_{cr}	creep damage parameter	[1]
d_{dipol}	critical spacing for the formation of dipoles	[m]
D_{gb}	grain boundary diffusion coefficient	[m^2s^{-1}]
d_{lock}	critical distance for spontaneous lock formation	[m]
D_p	mobile dislocations to serve a reaction partner	[1]
D_{SD}	self diffusion coefficient	[m^2s^{-1}]
D_{sub}	subgrain diameter	[m]
$\tilde{d}^\alpha$	slip direction	[1]
E	young's modulus	[Pa]
E_0	subgrain diameter	[m]
$\mathbf{E}$	Green-Lagrange strain tensor	[MPa]
F	gradient	[1]

Symbol	*Meaning*	*Unit*
$\vec{F}$	vector of forces	$[N]$
f^*	equivalent frequency	$[s^{-1}]$
f_i	volume fraction of cell interiors	$[m^{-3}]$
$f_i(\psi)$	$(i = V_p, S_p, B_p, P_p)$ formfunctions	[-]
f_h	volume fraction of hard zones	$[m^{-3}]$
f^k	frequency term	$[s^{-1}]$
f_s	volume fraction of soft zones	$[m^{-3}]$
f_v^i	volume fraction of the phase category i	$[m^{-3}]$
f_v^∞	volume fraction of precipitates in thermodynamic equilibrium	$[m^{-3}]$
f_v^p	volume fraction of particles	$[m^{-3}]$
f_w	volume fraction of cell walls	$[m^{-3}]$
G	shear modulus	$[Pa]$
$\mathbf{g}$	equilibrium stress vector	$[Pa]$
ΔG_n	free energy	$[J]$
$\Delta G_{n,c}$	critical value of free energy	$[J]$
h	height of dipoles	$[m]$
h_b	distance between dislocations in the subgrain boundary	$[m]$
ΔH_j^f	formation energy of a jog	$[J]$
H_m	activation enthalpy	$[J]$
j	jog	[-]
k	elastic limit	[1]
K	kinematic hardening parameter	[1]
k_0	constant	[1]
K^{-1}	viscosity matrix	[1]
k_1	parameter	[1]
K_1	constant	[1]
K_{Ic}	fracture toughness	$[MPa\ m^{-2}]$
k_B	Boltzmann factor	$[JK^{-1}]$
$K_{G,eff}$	effective grain size	$[m]$
$k[\Gamma]$	viscosity function	[-]
L	slip length	$[m]$
L_{eff}	effective glide distance	$[m]$
$L_f^\pm$	fatigue loading function	[-]
$L_c^\pm$	creep loading function	[-]
L_i	forest dislocation spacing in the cell interior	$[m^{-1}]$
L_i^{obst}	obstacle spacing	$[m]$
L_{ij}	symmetric tensor	[1]
L_p	spacing of precipitates	$[m^{-3}]$
$\mathbf{L}^p$	plastic velocity gradient	$[ms^{-2}]$
L_w	forest dislocation spacing in the cell walls	$[m^{-2}]$
L_α	distance between dislocations in the glide system α	$[m]$
δl	elongation	$[m]$

Symbol	*Meaning*	*Unit*
MF_f	multiaxiality factor	[1]
MF_c	multiaxiality factor	[1]
M_{ij}	symmetric tensor	[1]
M_{sg}	mobility of subgrain boundary	$[m^3N^{-1}s^{-1}]$
n	number	[1]
$\mathbf{n}$	normal vector	[1]
N_f	cycles to fracture	[1]
n_{GS}	number of active glide systems	[1]
N_i	relative subgrain density of the category i	$[m^{-3}]$
N_{ij}	symmetric tensor	[1]
n_i	unit normal	[1]
N_s^p	number of precipitations per unit of area	[1]
N_v^p	number of precipitations per unit of volume	[1]
$\tilde{n}^\alpha$	slip plane normal	[1]
P	part of a Frank-Read source	[-]
P'	part of a Frank-Read source	[-]
$\dot{p}$	reaction rate of an individual moving dislocation	$[s^{-1}]$
P_p	perimeter of a pore	$[m]$
p_{sg}	driving force of subgrain growth	$[Nm^{-2}]$
Δp	driving force	$[N]$
Q	activation energy	$[J]$
Q_{bulk}	activation energy for bulk diffusion	$[J]$
Q_{cross}	activation energy for cross slip (screw dislocations)	$[J]$
Q_{SD}	activation energy for self diffusion	$[J]$
r	isotropic hardening variable	[1]
R	body	[-]
r_0	initial pore size	$[m]$
R_0	body in reference configuration	[-]
R_1, R_2	parts of a separated body R	[-]
r_c	critical radius	$[m]$
r_f	critical pore size	$[m]$
R_h	increase of the elastic limit due to hardening	$[s^{-1}]$
r_p	particle radius	$[m]$
$r_{p,max}$	maximum axis length ratio of a particle	$[m]$
$r_{p,min}$	minimum axis length ratio of a particle	$[m]$
r_{sub}	subgrain radius	$[m]$
RT	ambient temperature	$[K]$
r_v	radius, determining the distance between two dislocations	$[m]$
S	surface	$[m^2]$
$\mathbf{S}$	vector of all microstructure parameters	[-]
S_D	surface of microcracks or microcavities	$[m^2]$
S_i	microstructure parameter	[1]

Symbol	*Meaning*	*Unit*
S_i^j	temporal variation of S_i due to the mechanism j	$[s^{-1}]$
S_p	pore surface	$[m^2]$
t	time	$[s]$
T	temperature	$[K]$
$\hat{t}$	characteristic time	$[s]$
t_0	initial time	$[s]$
t_{cr}	time to creep induced fracture	$[s]$
Δt	time increment	$[s]$
T_m	melting temperature	$[K]$
T_F	triaxiality factor	$[1]$
u	displacement vector	$[m]$
u_{ij}	partial derivations of the displacement vector u	$[m]$
u_{kl}	partial derivations of the displacement vector u	$[m]$
$\dot{u}_n$	displacement rate	$[s^{-1}]$
v	average dislocation glide velocity	$[ms^{-1}]$
V	volume, activation volume	$[m^3]$
$\dot{V}$	temporal derivation of the pore volume	$[m^3s^{-1}]$
v_c^l	climb velocity due to diffusion of vacancies	$[ms^{-1}]$
v_D	rate of dislocation glide	$[s^{-1}]$
v_g	glide velocity of mobile dislocations	$[ms^{-1}]$
v_{climb}	velocity of climb	$[ms^{-1}]$
$v_{c,m}$	climb velocity of mobile dislocations	$[ms^{-1}]$
$v_{c,m}^l$	climb velocity of mobile dislocations due to lattice diffusion	$[ms^{-1}]$
$v_{c,m}^p$	climb velocity of mobile dislocations	$[ms^{-1}]$
$v_{c,s}$	climb velocity of static dislocations	$[ms^{-1}]$
$v_{c,s}^l$	climb velocity of static dislocations due to lattice diffusion	$[ms^{-1}]$
$v_{c,s}^p$	climb velocity of static dislocations due to pipe diffusion	$[ms^{-1}]$
V_p	pore volume	$[m^3]$
v_{sg}	velocity of subgrain boundary	$[ms^{-1}]$
v^α	average velocity of dislocations in the slip system α	$[ms^{-1}]$
w_i	weight factor	$[1]$
W^{macro}	macroscopic virtual work	$[J]$
W^{micro}	work of all microstress components	$[J]$
ΔW_T	hysteresis energy	$[J]$
x	variable	$[1]$
$\mathbf{x}$	overstress	$[Pa]$
$\mathbf{X}_{bs}$	back stress	$[Pa]$
$\bar{x}_i$	median of variables x_i	$[1]$
dX	line element in reference configuration	$[1]$
y_c	critical annihilation distance	$[m]$
Z	Zeldovich coefficient	$[1]$

Symbol	*Meaning*	*Unit*
$\mathbf{Z}$	matrix	[1]
$\vec{Z}_\alpha$	vertical matrix	[1]
$\vec{Z}_\alpha^T$	transposed matrix	[1]
α	slip system	[-]
α^*	parameter, describes stress dependence of creep load	[1]
α_{FR}	Taylor factor at active Frank-Read mechanism	[1]
α_i	related kinematic hardening variable	[1]
α_m	Taylor factor	[1]
$\alpha[T]$	temperature coefficient	$[K^{-1}]$
β^*	parameter, describes the damaging effect of compression phases	[1]
β_i	constant, relating the internal spacing of dislocations i	[1]
β_w	constant, relating the spacing of dislocations in cell walls w	[1]
Γ	hemisphere	[-]
$\dot{\gamma}$	shear rate	$[s^{-1}]$
γ^*	parameter, specifies the influence of the load character	[1]
$\dot{\gamma}_{in}$	inelastic shear strain rate	$[s^{-1}]$
$\gamma^{'}$	phase, commonly Ni_3(Al, Ti, Nb)	[-]
γ_{gb}	grain boundary energy of the matrix material	$[Jm^{-2}]$
γ_{ip}	interface energy matrix/particle	$[Jm^{-2}]$
γ_s	surface energy of the matrix material	$[Jm^{-2}]$
γ_{SFE}	stacking fault energy	$[Jm^{-2}]$
γ_{sg}	interface energy of a small angle grain boundary	$[Jm^{-2}]$
γ_{sp}	interface energy particle/pore	$[Jm^{-2}]$
$\dot{\gamma}^\alpha$	glide rate on glide system α	$[s^{-1}]$
$d\gamma$	slip rate on all active glide systems in the grain	$[s^{-1}]$
δ	subgrain size	$[m]$
δ_{gb}	grain boundary thickness	$[m]$
ε	strain	[1]
$\dot{\varepsilon}$	strain rate	$[s^{-1}]$
$\bar{\varepsilon}$	effective strain	[1]
$\Delta\varepsilon$	strain increment	$[s^{-1}]$
ε_D	deviatoric strain	[1]
$\dot{\varepsilon}_e^\infty$	equivalent strain rate in the grain interior	$[s^{-1}]$
ε_e^μ	strain vector acting on the microplane	[1]
ε_{el}	elastic strain	[1]
$\dot{\varepsilon}_{el}$	elastic strain rate	$[s^{-1}]$
$\varepsilon_f^{'}$	fatigue ductility coefficient	[1]
$\bar{\varepsilon}_f$	effective fracture strain	[1]
ε_{ij}	macroscopic strain tensor	[1]
ε_{in}	inelastic (plastic) strain	[1]

Symbol	*Meaning*	*Unit*
$\dot{\varepsilon}_{in}$	inelastic strain rate	$[s^{-1}]$
$\dot{\varepsilon}_{in}^{n}$	normalised inelastic strain rate	$[s^{-1}]$
$\dot{\varepsilon}_{in}^{s}$	normalised inelastic shear strain rate	$[s^{-1}]$
$\bar{\varepsilon}_M$	effective matrix strain	$[1]$
ε_n	critical nucleation strain	$[1]$
ε_N	normal strain	$[1]$
ε_ν	volumetric strain	$[1]$
$\dot{\varepsilon}_{ss}$	steady state creep rate	$[s^{-1}]$
ε_{th}	thermal strain	$[1]$
$\dot{\varepsilon}_{th}$	thermal strain rate	$[s^{-1}]$
ε_V	volumetric strain	$[1]$
θ	misorientation	$[rad,^\circ]$
λ	jump width, i.e. mean spacing of obstacles	$[m]$
λ_m	distance between mobile dislocations	$[m]$
λ_p	distance between particle centres	$[m]$
λ_s	effective distance between particles	$[m]$
μ	median	$[1]$
μ	angle	$[rad,^\circ]$
ν_0	attack frequency	$[s^{-1}]$
ξ_j^t	value of variable at time t and node j	$[1]$
π	constant	$[1]$
$\dot{\rho}$	evolution of dislocation density	$[s^{-1}]$
ρ_b	related dislocation density in subgrains	$[m^{-2}]$
ρ_b^l	related dislocation density defined as break-through points per unit of length	$[m^{-1}]$
ρ_c	critical radius of curvature	$[m]$
ρ_i	dislocation density in the interior cells	$[m^{-2}]$
$\dot{\rho}_i^-$	reduction rate of dislocation density inside the cells	$[s^{-1}]$
$\dot{\rho}_i^+$	formation rate of dislocation density inside the cells	$[s^{-1}]$
ρ_m	mobile dislocation density	$[m^{-2}]$
$\dot{\rho}_m^-$	reduction rate of the mobile dislocation density	$[s^{-1}]$
ρ_w	dislocation density in cell walls	$[m^{-2}]$
$\dot{\rho}_w^+$	increase of dislocation density inside the cells	$[s^{-1}]$
$\dot{\rho}_x$	evolution of dislocations	$[s^{-1}]$
$\dot{\rho}_x^-$	reduction terms of dislocations	$[s^{-1}]$
$\dot{\rho}_x^+$	production terms of dislocations	$[s^{-1}]$
ρ^α	dislocation density in the glide system α	$[m^{-2}]$
$\dot{\rho}^\alpha$	evolution of dislocation density in the glide system α	$[s^{-1}]$
ρ_F^α	forest dislocation density in the glide system α	$[m^{-2}]$
ρ_P^α	density of parallel dislocations in the glide system α	$[m^{-2}]$
σ	stress	$[Pa]$
$\boldsymbol{\sigma}$	Cauchy stress tensor	$[Pa]$
Σ^I	1. Piola-Kirchhoff stress tensor	$[Pa]$

Symbol	*Meaning*	*Unit*
Σ^{II}	2. Piola-Kirchhoff stress tensor	$[Pa]$
σ_D	deviatoric stress	$[Pa]$
σ_{ext}	external stress	$[Pa]$
$\hat{\sigma}$	effective stress on the remaining surface	$[Pa]$
$\sigma_{eff,M}$	Von Mises effective stress	$[Pa]$
σ_{eq}	Von Mises equivalent stress	$[Pa]$
σ_f	macroscopic flow stress	$[Pa]$
σ_H	hydrostatic stress	$[Pa]$
σ_{kk}	first stress invariant	$[Pa]$
$\bar{\sigma}_M$	effective stress on the matrix material	$[Pa]$
σ_N	normal stress	$[Pa]$
$\sigma_{standard}$	standard deviation	[-]
σ_V	volumetric stress	$[Pa]$
τ	shear stress	$[Pa]$
τ	acting shear stress on the slip system α	$[Pa]$
$\hat{\tau}$	athermal shear stress	$[Pa]$
τ_c	annihilation time	$[s]$
τ_{dc}	duration of one cycle	$[s]$
τ_{eff}	effective shear stress	$[Pa]$
$\tau_{eff,i}$	effective shear stresses in the cell interiors	$[Pa]$
$\tau_{eff,w}$	effective shear stresses in the cell walls	$[Pa]$
$\tau_{H,c}$	twell time under compressive load	$[s]$
$\tau_{H,t}$	twell time under tensile load	$[s]$
τ_i	effective shear stress in the cell interiors	$[Pa]$
τ_i^j	sum of the internal stresses	$[Pa]$
τ_i^m	backstress due to mobile dislocations	$[Pa]$
τ_{loop}	line tension of a dislocation loop	$[Pa]$
τ_{or}	Orowan stress	$[Pa]$
τ_p	Peierls stress	$[Pa]$
τ_{pass}^{α}	passing stress	$[Pa]$
τ_{sc}	scale factor	[1]
τ_{th}	threshold stress	$[Pa]$
τ_w	effective shear stress in the cell walls	$[Pa]$
ψ	wetting angle of contact	$[rad,^\circ]$
ϕ	degree of buckling	$[rad,^\circ]$
ω	damage parameter	[1]
Ω_c	macro continuum	[-]
ω_c	creep damage	[-]
$\dot{\omega}_c$	creep damage rate	$[s^{-1}]$
ω_D	material damage, damage function	[-]
ω_f	fatigue damage	[-]
$\dot{\omega}_f$	fatigue damage rate	$[s^{-1}]$

1 Introduction

The alloying concept as well as the characteristic structure and mechanical properties of hot work tool steels are described at the beginning and subsequently the microstructure configuration is qualified. During application, the material is generally exposed to cyclic mechanical and thermal loads, which has an influence on the structure. The material hardening due to generation of dislocations (e.g. Frank-Read mechanism) and softening, like recovery processes (annihilation of dislocations, subgrain formation and growth) is described. These competing mechanisms have a lasting influence on the material structure and structure evolution. Cyclic mechanical and thermal loads can cause creep-fatigue interaction, which is the dominating load mechanism acting on tools which are exposed to accordant load conditions. Local damage and material defects such as micropores and cracks are initiated in the material after a certain operation time at the highest thermal, mechanical or thermo-mechanical loaded regions of the tool. In most cases regions of both high thermal and mechanical loads are critical for failure. The nucleation, growth and coagulation of pores to cracks are described extensively in chapter 5 and subsequently in chapter 6 void based damage criteria according to McClintock, Rice and Tracey and yield criteria based on void volume fraction, respectively, according to Gurson and Gurson-Tvergaard-Needleman are mentioned as well as continuum damage mechanics criteria like the effective stress concept according to LeMaitre and the model by Yeh and Krempl are described. In the subsequent chapter 7, ideas of modelling the lifetime at cyclic mechanical and thermal loading are mentioned. This can be done by empiric models which are based on the principle of implementating a damage parameter (e.g. the accumulation of creep damage, the strain rate modified accumulation of time dependent damage and the frequency modified damage function model) , damage mechanic models (e.g. the damage rate model and the modified damage rate model) which are based on the implementation of a damage function, physical approaches and fracture mechanical methods, respectively. Creep fatigue simulation especially, can be performed by finite element modelling (e.g. the elastic-viscoplastic Chaboche model), crystal plasticity finite element modelling, which detailly describes the dislocation mechanisms in one single crystal (i.e. grain or subgrain), or the microplane method where the reaction forces on an ascertained microplane are considered. Furthermore cellular automata based material models for finite element simulations, the representative volume element method and experimental simulations can be arranged. Finally conclusions out of this literature survey are drawn and an outlook on proceeding work is given.

2 Hot Work Tool Steels

Common for the two manufacturing processes, hot forging and die casting, is that they both have a die or a tool, which gives the product its final shape. These tools are usually very complex and expensive and in order to lower the production costs, they need to last for a long time. The materials used in the dies for hot forming are nowadays completely made of a special type steel, called tool steels. The developement of tool steel history is generally regarded to the evolution of steels in general, but the beginning of tool steel history is generally regarded to the year 1740 [1]. Much has happened in the developement since then and today there exist numerous types of tool steels, but the desire to increase the performance of the tool steels still remains.

The steels used for hot forming is a special type of tool steel, made to withstand a combination of heat, pressure and abrasion and has been classified hot-work tool steel, AISI type H. All hot work tool steels are used in a quenched and tempered condition. The most essential properties for these types of steels are high levels of hot strength 2.1, ductility, toughness, thermal conductivity, creep strength, temper resistance and also low thermal expansion [2]. Steels that need to maintain their properties at high temperatures, i.e. hot work tool steels require an increased temper resistance, so that an appropriate strength can be achieved after tempering at 550 – 650°C. The most convenient method is to use a secondary hardening reaction involving the precipitation of alloy carbides [2, 3].

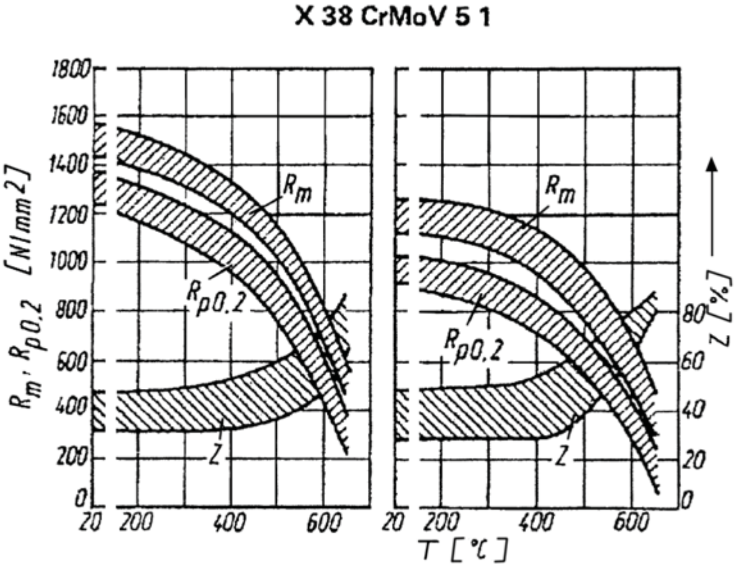

Figure 2.1: Tensile strength R_m and $R_{p0.2}$ as well as reduction in area vs. temperature for an annealed W300 with an initial tensile strength of 1500 MPa (left diagram) and 1200 MPa [4].

A good secondary hardening effect is achieved by strong carbide forming elements such as chromium, molybdenum, tungsten and vanadium. These elements play an important role when the tool steel is subjected to high temperatures, since they precipitate as fine alloy carbides, which not only retards the softening but also increases the hardness.

The temperature of tools in use is permanently above 200°C, thereby billets with temperatures of about 400 to 1200°C are converted. The contact times are from milliseconds to minutes and the longer the contact with the hot billet lasts, and the shorter the relative cooling time is, the higher becomes the surface temperature of tools, converging to the billet temperature. For a good performance, hot work tool steels have to exhibit four main properties [5]:

- A high tempering resistance to avoid a decrease in hardness due to thermal loads during use, which is maintained by a deceleration of martensite dissolution by alloying elements, precipitation of secondary carbides (Cr, W, Mo, V) and special heat treatment.
- A demanding hot strength, hardness and wear resistance at high temperatures to ensure deformation and wear resistance. It is achieved by the mechanisms mentined before and at temperatures above 600°C only by solid solution strengthening and precipitation of intermetallic compounds.
- A demanding toughness to prevent brittle fractures in zones with high concentrated stresses. Homogeneity and purity as well as microstructure parameters are necessary to be considered.
- Thermoshock resistance to avoid cracks caused by thermal alteration is improved by a good thermal conductivity and low thermal expansion, high toughness, homogeneity and hot strength.

2.1 Alloying Concept

The category of hot work tool steels contains a multiplicity of steels, which makes a classification not easy. According to the thermal loads, hot and high strength heat treatable steels with or without distinctive secondary hardness are in use. For extremly high temperatures, hot strength high temperature corrosion resistable austenitic steels and Ni-based alloys are demanded, which have a lower tendency to diffusion creep due to their closer packed atoms. Depending on the properties, hot work tool steels can be classified into following categories: impact resistant steels, wear resistant, ductile steels and high temperature strength steels and alloys [2, 5]:

- Impact resistant steels are Ni alloyed CrMoV-heat treatable steels with 0.5 to 0.6% C.
- Wear resistant, ductile steels are CrMoV or WCrV heat treatable steels with alloying contents up to 8% and 0.3 to 0.4 % C and CoCrMo(W,V) heat treatable steels with alloying contents more than 8% and up to 0.5% C.

- high temperature strength steels and alloys which exhibit γ' hardening and Ni based alloys like X 6 NiCrTi 26-15 and NiCr 20 Co 18 Ti.

Category	**Steel**	**Application**
low alloyed heat treatable steels	56 NiCrMoV 7	die holder and ram for extrusion, hammer dies
medium alloyed CrMoV and WCrV steels	X40 CrMoV 5-1 X 32 CrMoV 3-3 X 30 WCrV 9-3	die casting and extrusion tools for light and partly non-ferrous heavy metals, forging tools
high alloyed CoCrMo(W,V) steels	X 20 CoCrWMo 10-9 X 45 CoCrWV 5-5-5 X 15 CrCoMoV 10-10-5	die casting and extrusion tools for light and partly non- ferrous heavy metals, tools for forging machines at temperatures up to 700°C
high temperature strength steels and alloys	X 6 NiCrTi 26-15 X 50 NiCrWV 13-13 NiCr 19 CoMo	liners for extrusion of copper and Cu-alloys for billet temperatures above 750°C, die blocks for open die forging with longer durations

Table 2.1: Typical steel categories and applications for hot work tool steels [5].

The steels of the CrMoV category have the greatest importance for the application as materials for hot work tools which is because of their importance on extrusion and die casting, where they perform very well. WCrV steels exhibit a higher deformation resistance than CrMoV steels but they have a lower toughness, so their application is only then advantageous when CrMoV steels, despite their good ability to cooling, indicate insufficient deformation resistance. Typical steel categories and examples for application are given above in Tab. 2.1.

Hot work tool steels can also be classified by the main alloying element, the AISI type H steel is divided into three subgroups named after the dominant alloying element [2]:

Chromium hot work tool steels (types H10 to H19) are well adapted to hot work of all kinds. Especially dies for the extrusion of aluminium and magnesium, but also as die-casting dies, forging dies and hot shears.

Tungsten hot work tool steels (types H21 to H26) are used to make mandrels and extrusion dies for high temperature applications, such as the extrusion of brass, nickel alloys and steel. They are also suitable for use in hot-forging dies of rugged design.

Molybdenum hot work tool steels (types H42 and H43) are almost similar to tungsten hot work steels with almost identical characteristics and uses, but have their principal advantage in their lower initial cost. These alloys, especially molybdenum and the low carbon content, make the steel more resistent to heat checking.

The properties of hot work tool steels result from the chemical composition and heat treatment, which determines the microstructure of the steel. The main alloying elements and their effectiveness are described in the following [5]:

Cr	- increases hardenability - secondary hardening maximum at higher contents - inhibits high temperature corrosion and enhances wear resistance - extends transformation inactive range between pearlite and bainite
W,Mo,V	- increase hot strength, annealing and wear resistance (V) due to precipitation of carbides in the secondary hardening maximum - mechanism: MC (semi-coherent) $- >$ M_2C $- >$ M_6C, M_7C_3, $M_{23}C_6$ with increasing annealing temperature - precipitation effects of W and Mo beside secondary carbide formation due to intermetallic compounds (IMC) - W delays the precipitation of IMC to higher temperatures
Ni	- enhances hardenability - decreases A_1 temperature and impedes spheroidise annealing and enables lower austenitising temperatures, i.e. a finer structure after hardening
Co	- delays carbide precipitation which leads to a finer distribution - increases secondary hardness due to formation of IMC, but ductility decreases - enhances the temper resistance up to 600°C - advances the thermal conductivity - below 5 % no influence on hardenability
Si	- leads to higher strength at annealing temperatures of 200 to 600°C in 5% CrMoV steels - enhances high temperature corrosion resistance and hardenability - produces a finer grain structure but raises the affinity to segregation
Mn	- increases hardenability at simultaneous restriction of toughness, but a lower carbon content avoids this effect

The chemical compositions of several hot work tool steels are given in Table 2.2:

Steel grade	**C**	**Si**	**Mn**	**Cr**	**Mo**	**Ni**	**V**	**W**	others
W100	0.29	0.25	0.30	2.7	–	–	0.35	8.5	–
W300	0.38	1.10	0.40	5.0	1.3	–	0.40	–	–
W360	0.50	0.20	0.25	4.5	3.0	–	0.55	–	–
W400	0.36	0.20	0.25	5.0	1.3	–	0.45	–	–
W500	0.55	0.25	0.75	1.1	0.5	1.7	0.10	–	–
W750	0.04	0.25	1.4	15.0	1.3	25.0	0.3	–	Ti=2.7 Al=0.25 B=0.005

Table 2.2: Chemical compositions of selected Böhler hot work tool steels [6, 7].

2.2 Heat Treatment and Mechanical Properties

The initial state is generally soft-annealed with spheroidal carbides in a ferritic matrix. Carbides like $M_{23}C_6$, M_7C_3, M_6C and MC exist and the steel produced by Böhler Edelstahl GmbH is processed by the customer and heat treated afterwards (Fig. 2.2).

For low alloyed steels, hardening temperatures of about 830 to 900°C and 1000 to 1080°C for high alloyed steels are common. Adequate preheating steps reduce thermal stresses in cross sectional variations and between edge and core of the component. Lower hardening temperatures are adjusted at tools with high required toughness, complex geometries and small section thickness, higher hardening temperatures are common for massive components [5].

The quenching medium, e.g. air, oil, warm bath, salt bath or nitrogen for vacuum hardening, is dependend on the steel grade. Too low quenching rates cause pre-eutectoid carbide precipitations or lead to high amounts of bainite whereas too rapid quenching causes distortion and stress induced cracks.

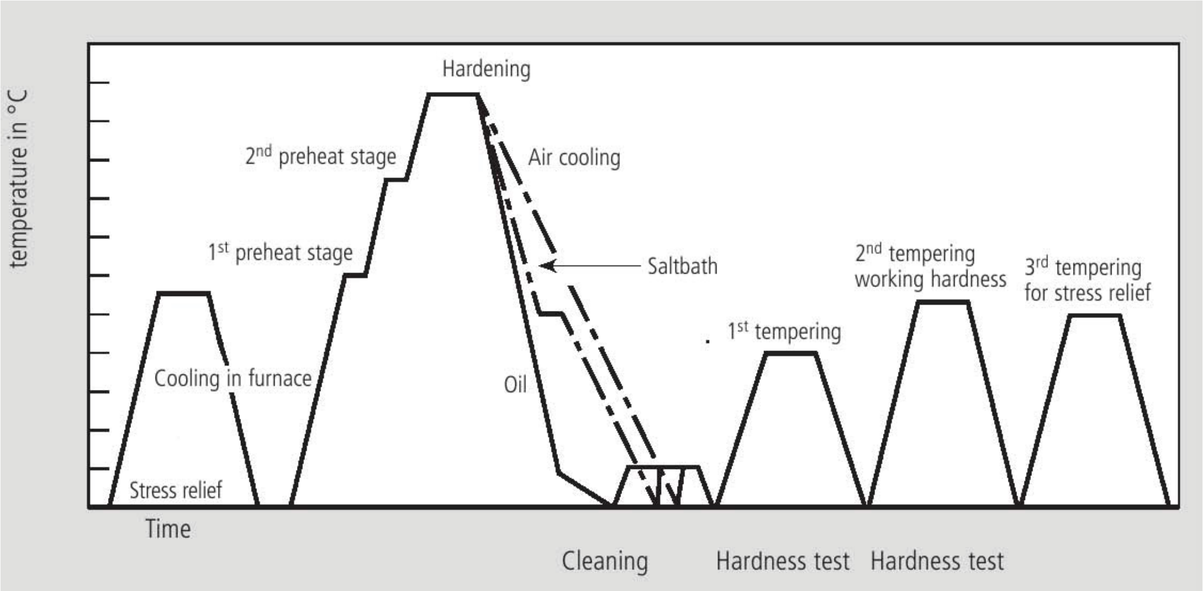

Figure 2.2: Heat treatment for the hot work tool steel Böhler W400, schematically [7].

At temperatures of about 500 to 600°C the steels are tempered overall for one to two hours, gerally in two or three separate steps. The influence of the tempering temperature on hardness is depicted in Fig. 2.3. The higher the tempering temperature is, the more decreases the hardness due to resolution of martensite and the tougher the material becomes.

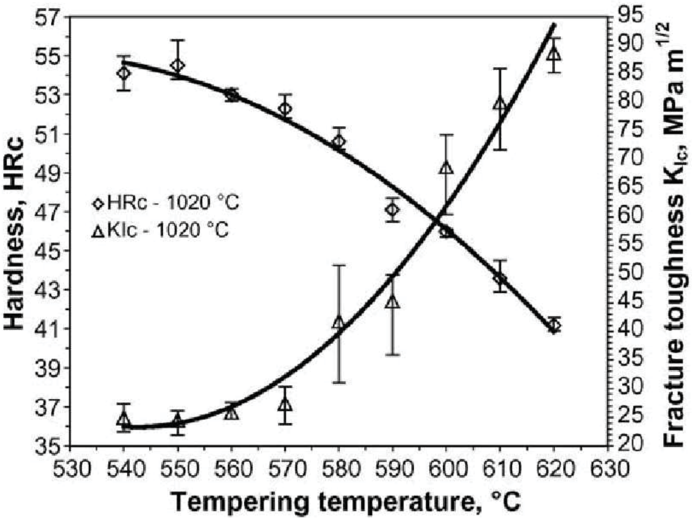

Figure 2.3: Effect of tempering temperature on the hardness and fracture toughness K_{Ic} of the vacuum-heat treated conventional hot work H11 tool steel (W300). [8].

Steels with a low content of secondary carbide formers (e.g. 56 Ni CrMoV 6, in Fig. 2.4) show a continuous decrease in hardness. High alloyed grades show a secondary hardening maximum due to precipitation of secondary carbides, IMCs and residual austenite transformation. The position of the secondary hardness maximum depends on the solution state of the matrix. During annealing also transformations of established carbides occur [5].

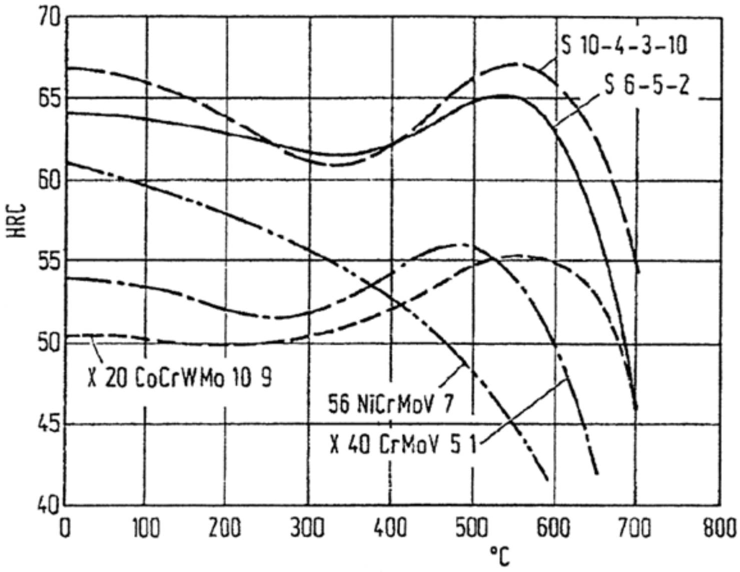

Figure 2.4: Temperature curves of several tool steels: The diagram depicts the Rockwell harness (HRC) vs the annealing temperature (°C) for the hot-work tool steels X 20 CoCrWMo 10-9, 56 NiCrMoV 7 and X 40 CrMoV 5-1 as well as for two high speed steels. [5].

In such types of steel, the most stable carbide is the VC-carbide, which also plays an important role in the heat treatment. VC-carbides are responsible for pinning grain boundaries in order to inhibit the grains from growing, which allows higher austenitising temperatures without a significant grain growth. If the temperature is too high (about 1100°C), i.e. high enough to dissolve the VC-carbide, the material experiences a rapid grain growth (Fig. 2.5). If a relatively high austenitising temperature is applied in the heat treatment, more of the primary carbides will be dissolved and thus increase the secondary hardening effect.

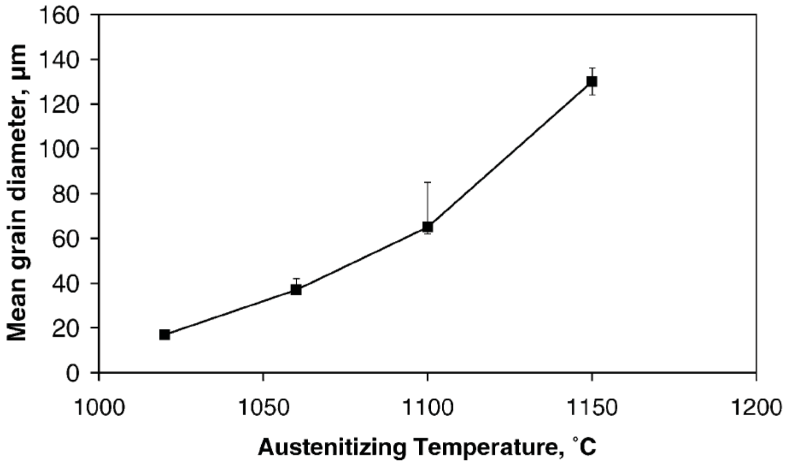

Figure 2.5: Mean austenitic grain diameter after different austenitising temperatures investigatet for the hot work tool steel DIEVAR [9].

It has been shown that V:C ratios close to stoichiometric gives a better secondary hardening effect as well, simply because the amount of VC available for precipitation is greater [3]. Consequently, the temper resistance is increased, which is also dependent on another important feature such as the stability of the carbides. Studies have shown that decreasing of the chromium and increasing the molybdenum content will generate more stable carbides, because the chromium rich carbides M_7C_3 and $M_{23}C_6$ can easily coalesce and coarsen with negative influence on mechanical properties. The microstructure in detail is described in chapter 3.

To minimise wear rupture of dies, high quality hot work tool steels are in use and in addition, several surface treatments, such as nitriding, are employed to increase wear resistance of tools. Nitriding consists of introducing nitrogen into metallic materials to improve their surface hardness, wear and corrosion resistance, as well as fatigue life. During nitriding of steels, two different structures are formed from surface to core, known as the compound layer and diffusion region. The compound layer consists of iron nitrides of the phase (ε-$Fe_{2-3}N$), gamma phase (γ'-Fe_4N) or of a mixed phase (ε+γ') developed at the surface. Wear characteristics of the compound layer depend on many factors such as compound layer composition (epsilon/gamma), compound layer thickness, mode of mechanical loading, etc. [10]. On the other hand, the diffusion region causes an improvement of fatigue strength when compared to an untreated material. In the material, nitrogen atoms also dissolved interstitially in excess in the ferritic lattice, which provide the formation of nitride precipitates [11].

3 Microstructure

In the following chapter, the microstructure of especially bcc-metals is described with respect to several microstructure parameters, which finally have a basic influence on mechanical properties of the material.

Microstructural Parameters

The microstructure can be described by

- the grain size,
- the mobile dislocation density ρ_m,
- the subgrain-radius r_{sub},
- the distribution of subgrain size by the several distribution-parameters,
- the misorientation θ,
- the related dislocation density in subgrains ρ_b,
- as well as by the parameters for all occurring populations of precipitations f_v^p and r_p.

3.1 Precipitations

Precipitation hardening is a basic mechanism in hot work tool steels to achieve reasonable mechanical properties. It is described in the following, how to characterise them and their influence onto material hardening is depicted.

Interface-Character of Precipitations

The nature of interface is important for the appreciation of interactions with dislocations and topology of dislocations, and also for the selection of adequate models.

Characterisation of Precipitations

In general phases can be quantitatively described by:

- The volume fraction f_v^p,
- the average particle radius r_p or particle diameter d_p,
- the number of precipitations per unit of volume N_v^p

$$f_v^p = \frac{4}{3}\pi r_p^3 N_v^p, \tag{3.1}$$

- the number of precipitations per unit of area N_s^p

$$N_s^p = 2N_v^p r_p, \tag{3.2}$$

- the distance between centres λ_p

  $$\lambda_s = (N_s^p)^{-1/2} \tag{3.3}$$

  in any cutting plane. Kocks, Foreman and Mecking (in [12]) mentioned that the smallest distance between particles in a plane cannot describe the mechanical interaction of dislocations with particles. They obtained an effectual distance of particles from their analysis of a random particle distribution

$$\lambda_s = 1.8(N_s^p)^{-1/2} = 1.25 r_p \left(\frac{2\pi}{3f_v^p}\right)^{1/2}. \tag{3.4}$$

- The aspect-ratio a_r

  $$a_r = \frac{r_{p,max}}{r_{p,min}} \tag{3.5}$$

  is in proportion to the maximum to minimum axis-length ratio of a particle in a cutting plane.

The parameters r_p, a_r, λ_s and N_s^p distinguish second phases as means under condition of a statistical distribution.

Commercial alloys are commonly heterogeneous, i.e., comprise second phases in a solid-solution matrix. Dislocation motion in such systems has to take into account solid solution hardening and precipitation hardening. Shearable precipitates essentially affect the yield stress only, while the hardening behaviour of the respective alloy is akin to that of the pure matrix materials or its solid solution. Non-shearable particles affect plastic flow mainly in two ways. First, they increase the yield stress by the Orowan stress

$$\tau_{or} = \frac{Gb\sqrt{f_v^p}}{r_p}, \tag{3.6}$$

and second, they drastically increase the hardening rate due to the plastic zone (geometrically necessary dislocations) in the wake of the particles. The dislocation concept introduced here does not lend itself easily to accommodate these physical processes, but they can be accounted for qualitatively by the basic equations derived so far. A higher yield stress can be represented by a larger glide resistance as expressed by a larger activation energy Q for glide (Eq. 4.28). The increased hardening rate is taken care of by modification of the slip length, i.e., by incorporating the precipitate spacing

$$\lambda_p = \frac{r_p}{f_v^p} \tag{3.7}$$

in the effective slip length as already accounted for in Eq. 4.32. In particular, for elevated-temperature deformation, λ_p may depend on time, since precipitation and Ostwald ripening may occur during deformation. It is followed a concept proposed by Estrin and co-workers [13] to account for this complication. For precipitate coarsening the change of precipitate radius with time is given by

$$r_p = c(t + t_0)^{1/k_1} \tag{3.8}$$

with C_k the kinetic constant, t the time, t_0 the time prior to the test, and the parameter $k_1 = 3$ for ideal Ostwald ripening according to the Lifshitz-Slyozov-Wagner theory (LSW theory). If concurrent precipitation occurs the precipitate volume fraction will change, which can be described by an Avrami-type equation

$$f_v^p = \left\{ 1 - exp\left[-\left(\frac{t + t_0}{\hat{t}} \right)^m \right] \right\} f_v^\infty \tag{3.9}$$

with an Avrami exponent m and the volume fraction f_v^∞ of precipitates in thermodynamic equilibrium. The characteristic time is

$$\hat{t} = \frac{A_0}{D} = \frac{A_0}{D_0} exp\left(\frac{H_m}{k_B T} \right) \tag{3.10}$$

with A_0 a constant, D the respective diffusion coefficient comprising the pre-exponential term D_0 and the activation enthalpy H_m. The diffusion coefficients are taken for the main alloy components. It is noted that this concept unlawfully mixes two kinetics, namely precipitation and ripening kinetics. Since both processes operate on a different time scale, however, the error introduced is small and mitigated by using effective kinetic constants, e.g., an effective k_1 in Eq. 3.8.

3.2 Dislocations

Dislocations are a main microstructure constituent and it is necessary to know how they react and which mechanisms are operating when loads are applied. In bcc-Fe lattice

	Sliding plane at		
Metal	RT	low T	high T or low ε
Fe	{112}	{110}	{123}
	{110}	{112}	$\{hkl\}$
Fe-3Si	{112}	{110}	{123}
	{110}	{112}	$\{hkl\}$

Table 3.1: Sliding planes in bcc-metals at different temperatures [14].

dislocation slide occurs in the direction of the closed packed direction $\langle 111 \rangle$. Closed packed layers in bcc-metals are from the type $\{110\}$. $\{123\}$ planes and non crystallographic planes $\{hkl\}$ have been found in addition to the dominant sliding planes $\{110\}, \{112\}$. With increasing temperature and/or decreasing strain rate, the dominated sliding plane changes (according to Smoluchowsky and Opinsky, in [14]) as follows: $\{110\}, \{112\}, \{123\}$ and $\{hkl\}$ as shown in table 3.2.

The non-crystallographic slide (hkl) at elevated temperatures and/or low strain rates is declared by cross-sliding of screw dislocations. Electron microscope investigations at low temperatures discovered long screw dislocations, which means that edge dislocations are more mobile than screw dislocations, so screw dislocations determine slide characteristics. Screw dislocations also have jogs with edge character. The concentration of jogs in thermodynamic equilibrium c_j^e, for example in the unit of jogs per defined length, can be described by an approach of Arrhenius [15]

$$c_j^e = \frac{1}{b} e^{-\frac{\triangle H_j^f}{k_B T}} \tag{3.11}$$

as a function of the formation energy of a jog

$$\triangle\, H_j^f \cong \frac{G b^3}{K_1} \tag{3.12}$$

with K_1=10..15 [16]. Pure metals with bcc lattice show a high Peierls-stress at ambient temperatures. The plastic deformation is controlled by the movement of screw dislocations, which transcend the Peierls-potential. With increasing temperature, i.e. thermal activation, pairs of kinks are formed, which facilitate the transcendation of the Peierls potential.

Precipitations inhibit dislocation gliding, i.e. the dislocation has to climb or cut the precipitation. Incoherent particles are non-shearable, the only way to pass them is to go around or climb. Climb can occur by local or general climb (Fig. 3.1).

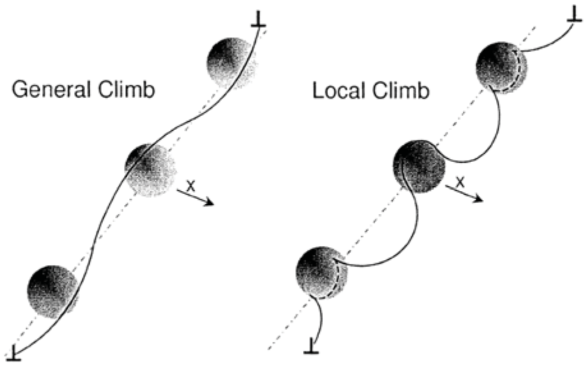

Figure 3.1: Imagination of passing particles by climbing, x denotes the direction of dislocation motion [17].

Coherent particles can be passed by cutting or going around, depending on the particle size. The energy for cutting small particles is much less than for cutting big ones which are passed by going around, which is energetically more favourable.

Splitting up of Dislocations

The high stacking fault energy in Fe and ferritic Fe-alloys is a reason that stacking faults cannot be observed in these materials. However, atomistic calculations found out that screw-dislocations under passive state split up marginally. This is also a characteristic caused by the high Peierls-stress. The conceptions on movement of a splittet, non-planar screw dislocation are related to a crystallographic slide, where the core structure changes before overpowering the Peierls barrier [18].

3.3 Subgrain Structure

Argon and Takeuchi [19] schematically outlined the developement of the substructure for metals with distinctive affinity to formation of subgrains (Fig. 3.2). Due to recovery during creep, the cellular structure is transformed into a substructure.

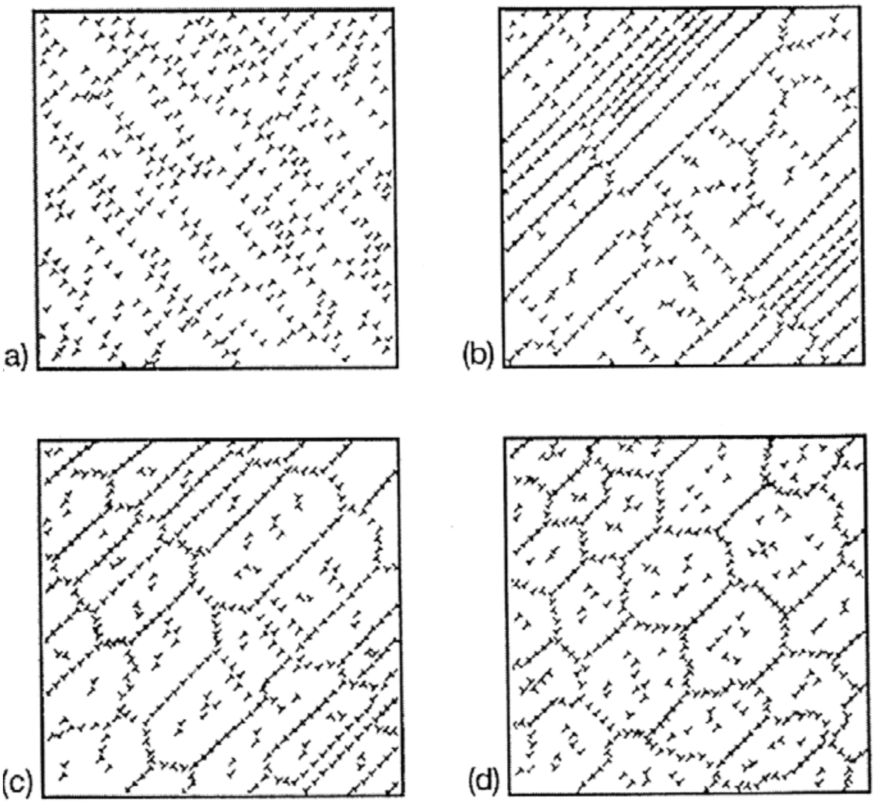

Figure 3.2: Schematical evolution of the substructure during a primary and secondary creep. Loading (a), early range (b) and late range (c) of primary creep and accumulated subgrain structure (d) in the secondary creep range [19].

In contrary to perfect LED-structures (low energy dislocation structures) like subgrain boundaries, the cell walls are an accumulation of dislocations which do not all take a LED-position. Cell boarders or cell walls consist of dislocation dipoles which annihilate during creep.

3.3.1 Dislocation Structure at Subgrain Boundaries

According to Orlova et al. [20], subgrains in $\alpha - Fe$ contain of a tilt as well as of a torsion part. Besides dislocations of type $\frac{a}{2}\langle 111\rangle$, also dislocations with the Burgers- vector $\langle 001\rangle$ can be found. The formation of these dislocations is established by the reaction

$$\tfrac{1}{2}[111] + \tfrac{1}{2}[1\overline{1}\overline{1}] \rightarrow [100].$$

If two interacting dislocations are of screw type, a pure screw dislocation with the Burgers vector [001] is the result.

The plane of the investigated sheet lies parallel to the plane of the network. Dingley et al. [21] found out that the percentage of [100]-dislocations is about 20. Carrington, Hale and McLean (in [14]) investigated the dislocation structure of subgrain boundaries at deformed and recovered $\alpha - Fe$ by thin-sheet experiments. It was possible to explicate and correlate the form of subgrain boundaries and networks by $a\langle 100\rangle$-edge-dislocations. Total concordance with the theory of Frank is given for some observed networks only for the account that $a\langle 110\rangle$-dislocations are formed by cutting $a\langle 100\rangle$-dislocations. In the case of only rotary boundaries, the fractions of dislocations which imply an acute angle, react by the energy law. The sections of dislocations which imply an optuse angle would react to an [110] dislocation. If the interbreeding dislocations do not lie in the rotary plane, both reactions can occur [22].

Dislocation Density in the Subgrain Boundary

The density of interface dislocations is defined as length per unit of area or break-through-points per unit of length. According to Gottstein and Argon [23], the density

$$\rho_b^l = \frac{\theta}{b} = \frac{1}{h_b} \tag{3.13}$$

with $[\rho_b^l] = [m^{-1}]$ is a function of the misfit-angle θ and of the distance between the dislocations in the subgrain boundary h_b. Therefore $\theta \sim sin\theta$ and $\theta \ll 1$ is assumed. If the volume-density ρ_b of the subgrain boundary dislocations is considered, then

$$\rho_b^l = \rho_b D_{sub} \tag{3.14}$$

with D_{sub} as the subgrain diameter, is obtained. Introducing ρ_b^l results for the factor ρ_b by

$$\rho_b = \frac{1}{h_b D_{sub}}. \tag{3.15}$$

The assumption that the subgrain boundary generally only consists of two dislocation families with distances of the same amount, the distance in the subgrain boundary, finally results in

$$h_b = \frac{2}{\rho_b D_{sub}} = \frac{1}{\rho_b r_{sub}}. \tag{3.16}$$

Additionally to intrinsic dislocations, there is also an accumulation of dislocations at the interface. This dislocations, immobilised after a gliding process, are defined as static dislocations which do not adopt a LED-position and are comparable to dislocation dipoles in cell walls. Due to the density of these static dislocations ρ_s, it is possible to describe the change of nature of the substructure-interfaces during creep of cell walls to subgrain boundaries.

Misorientation

The qualitative developing of misorientation with increasing deformation for various materials is known from literature facts. According to investigations of cubic metals, the misorientation among subgrain boundaries increases with advanced strain, whereas in the investigation of pure iron, the distance between the dislocations h_b and the angle between subgrain boundaries from a distinctive strain on, remains constant and embraces significant smaller values 1.5° instead of $> 3°$. Initiating at small values ($\sim 10'..20'$), the devolution of θ as a function of time or strain shows a comparative linear rising in the primary and partly in the secondary creep range until a saturation value is approached. The kinetics of misorientation is similar to, or dependent on the other kinetic distributions of other microstructure parameters like dimensions of subgrains or dislocation density [22].

3.3.2 Subgrain Size Distribution

It is not adequate to describe the substructure via use of means. Non-linear effects investigated by Orlova [20] are a reason for that. In addiction to the subgrain size, mechanisms are operating in various extends, which provide a varying growth performance of subgrains of differing size. The subgrain structure under creep loads can be described by a $log - normal$ distribution of the subgrain size

$$f(x) = \frac{1}{\sqrt{2\pi}\sigma x} exp\left[-\frac{(ln(x) - \mu)^2}{\sigma^2 2}\right] \tag{3.17}$$

as a function of the median μ and the standard deviation σ. In the other hand, i.e. if the distribution parameters σ and μ are allocated, a rough discretisation of the distribution in n subgrain categories can be accomplished. The relative density N_i of the category i

$$N_i = \int_{A_i}^{B_i} f(x)dx \tag{3.18}$$

with the boundaries A_i and B_i

$$\overline{x_i} = \frac{A_i - B_i}{2} \tag{3.19}$$

results in the fraction of volume f_v^i of the category i by

$$f_v^i = \frac{\overline{x}_i^3 N_i}{\sum_{i=1}^{n} \overline{x}_i^3 N_i}. \tag{3.20}$$

4 Structure Evolution during Cyclic Thermo-Mechanical Loads

4.1 Hardening Processes

Hardening must be due mostly to the dislocations produced by the plastic deformation. The point defects - e.g. vacancies and interstitial atoms - which are produced are too mobile and too few in number to play an important role. Dislocations introduced into a crystal can harden it in two ways:

1. They increase the internal stresses and thus can hinder, by elastic interactions, the development of loops from active sources.
2. They increase the density of the forest of screw dislocations which pierce their slip planes. Thus the development of the loops requires that proportionally more jogs are formed.

Frank-Read Mechanism

When the elastic limit, which is the stress above the deformation, does not go back to zero, i.e. the yield stress σ_y, which is usually of the order of $10^{-4}G$, is reached, a few Frank-Read sources will start emitting loops as described in Fig. 4.1 from the beginning on (1) to a complete loop (7).

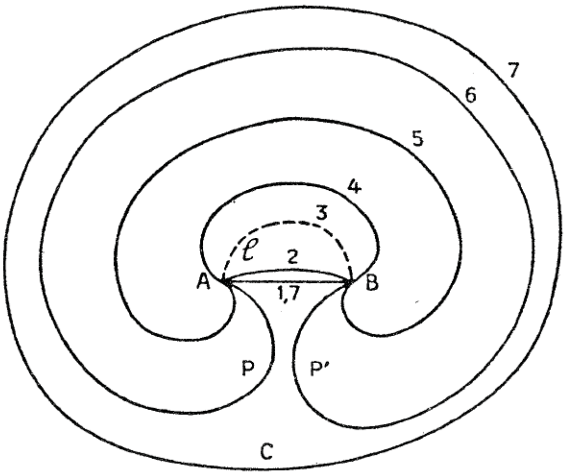

Figure 4.1: Development of a Frank-Read source [24].

In ductile crystals these will be the most favourably placed, i.e. in the slip system with maximum resolved shear stress, of a great length, in regions where the Frank network has an especially large size. Once developed over a region of large enough radius, these loops should be able to cut across the whole crystal and disappear at the surface. This is because, if the radius is large, the back stress of the loops on the emitting source will be small. If a large number of loops is emitted under a small applied stress, the first of these loops will be pushed through the denser parts of the Frank net with the help of the other loops behind it [24].

If the crystal contains, before any deformation, sufficiently long dislocation lines AB, they can be those of a Frank network with the free length l, which is equal to the distance between nodes. The dislocation can leave the slip plane, or it is pinned down by impurity atoms or precipitates 4.2.

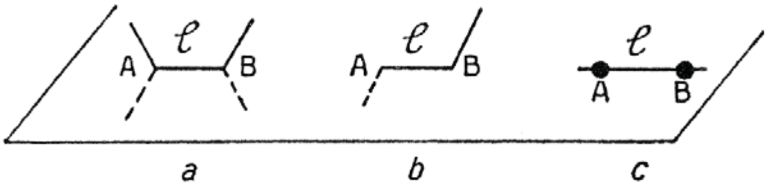

Figure 4.2: Various possible modes of pinning Frank-Read sources [24].

Under the action of a shear stress in its slip plane, such a line AB bends. The curvature, and therefore the shear stress which produces it, pass through a maximum when the loop is a semi-circle of the diameter AB. Under this maximum shear stress τ_{max}, a whole circle of dislocation, of diameter $2r = AB = l$ would be in equilibrium. According to Eq. 4.1

$$\tau_{max} \simeq \frac{2\tau_{loop}}{lb}, \tag{4.1}$$

where τ_{loop} is the line tension of the loop ($\tau \sim Gb^2$). If the applied stress exceeds this value, the line can increase beyond a semi-circle and develop into a complete loop C, at the same time restoring the initial line AB. This mechanism produces a large number of dislocation loops.

If n loops are produced in the same crystallographic plane and if they emerge at the surface, the created step on the surface must be then parallel to the this glide plane. This assumes that the dislocation lines, which end at the pinning points A and B of the source (Fig. 4.2), have Burgers vectors parallel to this glide plane. For example, such will be the case when the pinning is as shown in Fig. 4.2b and c, where the lines which end at the points A and B are assumed of the same nature as that of the line AB. But it may happen that, as in Fig. 4.2a, one of the pairs of lines ending in A or B will have Burgers vectors with a non zero projection on the normal to the glide plane. Such an alteration causes several types of Frank-Read sources 4.3:

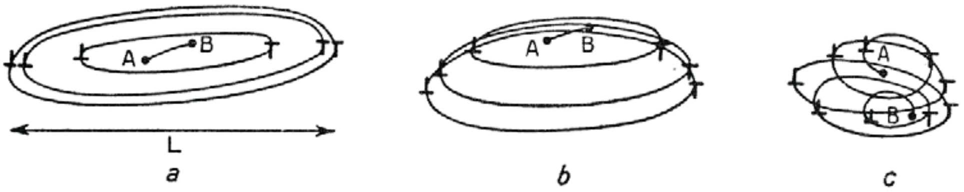

Figure 4.3: The three types of Frank-Read sources: (a) flat; (b) spatial; (c) spiral [24].

If the projections of the arcs ending on A and B are equal, the successive loops emitted by the source find themselves on different glide planes at a certain distance from each other (Fig. 4.3b). This configuration has been called by Seeger [25] a spatial source, in contrast to the flat source (Fig. 4.3a) considered so far.

If the projections are unequal, two spirals develop, around each of the points A and B. This is known as a spiral source (Fig. 4.3c). More exactly, after each turn of a spiral source around A and B, the parts P and P' of the source (in Fig. 4.1) will be on planes separated by one more interatomic distance. Three successive processes are expected, descibed in Fig. 4.4:

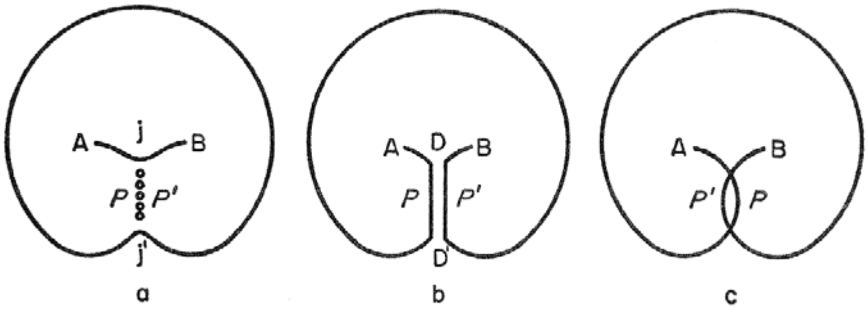

Figure 4.4: Three successive stages for a spiral Frank-Read source [24].

At each of the few first turns, P and P' will recombine by fast climb. A row of point defects will be produced along the length they recombine, and two jogs (j, j') of increasing length are formed at its ends (Fig. 4.4a).

After a few turns, the parts P and P' will be in planes too far away for rapid climb to occur because of their strong elastic interactions, one expects a new dipole DD' of increasing height to be formed at each turn (Fig. 4.4b).

After many turns, the distance between their planes might become so large that the parts P and P' can pass each other without forming a dipole. Two independent spirals develop around A and B (Figs. 4.3c and 4.4c). For not too large applied stresses, the kinetic energy of the dislocation is negligible and the maximum height h (Eq. 4.2) of the dipoles thus formed is such that the applied stress pushes P and P' past each other:

$$h \simeq \frac{Gb}{2\pi\sigma}. \tag{4.2}$$

This is usually so large that a spiral source should stop acting much before the corresponding number of turns, of the order of h/b, has been produced. The dipoles produced harden the lattice locally, so that spiral sources should be anyway much less active than flat or spatial ones. With spatial or spiral sources, slip is no longer concentrated on a well defined plane, but is distributed uniformly in a small zone [26].

4.2 Softening Processes

4.2.1 Recovery

The state of a material under loads is basically instable, because the produced dislocation structure is not in thermodynamic equilibrium. At respective low temperatures, the plastic deformation maintains due to mechanical stability, because the dislocations remain in a mechanical equilibrium of forces after withdrawal of loads. At higher temperatures this mechanical stability can be overpowered by thermal activated processes, when dislocations are able to resolve their inhibition by cross sliding of screw dislocations or climbing of edge dislocations. Thereby dislocations can switch to other sliding planes and adopt energetical advantageous positions, and they are able to annihilate one another or leave the crystal. This procedure is known as recovery and causes a decrease of dislocation density, and produces specific dislocation structures consisted of a network of small-angle grain boundaries, which is defined as polygonisation. The recovery is based onto the interaction of dislocations due to their wide ranged stress field. The interaction force F of an edge dislocation with the Burgers vector b_1 upon a parallel dislocation with the Burgers vector b_2 is

$$F = \tau b_2 = \frac{G b_1 b_2}{2\pi r_v (1-\nu)} cos\Phi cos2\Phi \tag{4.3}$$

whereas r_v and Φ determine the position of the first dislocation in relation to the second, and ν denotes the poisson ratio. If both dislocations have the same sign and maintain on the same sliding plane, i.e. $\Phi = 90°$, the force is positive and they repel. If both dislocations have antipodal signs, the force is negative, they attract, fuse and annihilate one another. This procedure is responsible for a decrease of dislocation density. If the dislocations with antipodal signs do not have the same sliding plane, but one inbetween, a dislocation dipol is formed, which corresponds to a chain of vacancies and has a significant lower engergy than both single dislocations and annihilation can result due to climbing by the distance of one atomic layer. This annihilation also occurs by attraction and manifold climbing over a couple of layer distances. If the sliding planes are far away, so that $\Phi > 45°$, the sign changes according to Eq. 4.3 and anti-parallel dislocations repel, whereas parallel dislocations attract each other. The position of equlibrium of two parallel dislocations is reached when they are lying upon each other, then $\Phi = 90°$ and $F = 0$ in Eq. 4.3. Every deflection out of this position finally ends up in the idle state. If many dislocations arrange one upon the other, a significant minimisation of dislocation energy is caused. Such a periodic arrangement of edge dislocations causes a dislocation interaction, which reduces the range R_a of the stress field to the magnitude of the dislocation distance r_v. If there are ρ_b^l dislocations per cm in this arrangement, the energy per unit of area is

$$\gamma_{sg} = \rho_b^l \left[\frac{Gb^2}{4\pi(1-\nu)} ln \frac{r_D}{2b} + E_C \right] \tag{4.4}$$

where E_C denotes the energy of the dislocation core. The described arrangement approximates a small angle tilt grain boundary (SAGB) and γ_{sg} denotes the specific grain boundary energy. The difference in the orientation Θ of the adjoining grains can be described by

$$\Theta = \frac{b}{r_D} \tag{4.5}$$

and $1/r_D = \Theta/b = \rho_b^l$ is the number of dislocations per cm in the small angle grain boundary. Hence the specific energy of the SAGB results in:

$$\gamma_{sg} = \Theta(K_1 - K_2 ln\Theta) \tag{4.6}$$

where K_1 and K_2 are defined as

$$K_1 = \frac{E_K}{b} - K_2 ln2 \tag{4.7}$$

and

$$K_2 = \frac{Gb}{4\pi(1-\nu)} \tag{4.8}$$

The same consideration can also be taken for screw and hybrid dislocations, which also built similar networks of low energy. A complete regional network can be build up by several small angle grain boundaries consisting of screw, edge and hybrid dislocations, which has a much lower energy than randomly distributed dislocations. Grain boundaries can be formed due to coalescense of several subgrain boundaries. Recovery is affected by climbing and cross sliding, both processes are sensitively depending on the stacking fault energy γ_{SFE}, in a way that climbing and cross sliding are benefited by higher stacking fault energys. Materials with a high stacking fault energy show strong recovery like most bcc metals and fcc aluminium. Ag, Cu and fcc alloys exhibit a low stacking fault energy and show a lower tendency to recovery [27].

4.2.2 Subgrain Formation

Basically the following mechanisms are responsible for subgrain growth [28]:

- Subgrain growth due to reduction of the whole interface energy, at varying specific interface energy by recovery and knitting processes in the subgrain boundary or regions close to the boundary,

- nucleation of subgrains by transition of a critical dislocation density in the inner subgrain,
- recovery of dislocations at the subgrain boundary, and
- knitting processes: knitting out and knitting in of dislocations

For a movement of subgrain boundaries, it is necessary that the dislocations in the subgrain boundary glide and climb. Climbing of dislocations is the slower and determining step of the velocity. In gerneral it is known that the subgrain structure in metals with a high stacking fault energy γ_{SFE} at homologous temperatures of about 0.3-0.4T_m is formed due to energetical factors. The character of this two-dimensional dislocation structure goes from ideal conceptions of a *low energy dislocation structure* (LEDS) to clews of dislocations, which can be associated with cell walls. Following general statements it can be formulated that [29]:

- In metals with a low stacking fault energy γ_{SFE}, which have no tendency to form subgrains, recrystallisation can occur.
- The propability of a cell or network formation decreases with decreasing stacking fault energy, which is a reason of advanced split-up of dislocations, which impedes a cross sliding of screw dislocations. Solid solution generation decreases the stacking fault energy and minimizes the affinity to cell creation.
- Generally the size of the cell expands in relation to the steady state with increasing stacking fault energy.
- The subgrain size in Fe - based alloys is independent of the grain size.

4.2.3 Subgrain Growth

Subgrain growth can be considered, according to a partition in serveral material types, like

- pure material,
- solid solution, and
- precipitation strengthened material.

The velocity of a subgrain boundary υ_{sg} can be described by the attempt of Einstein (in [30])

$$\upsilon_{sg} = M_{sg} p_{sg} \tag{4.9}$$

with M_{sg} standing for the mobility ($[M_{sg}] = [m^3/Ns]$) of the subgrain boundary and p_{sg} depicting the force ($[p_{sg}] = [N/m^2]$) of the subgrain growth. Several models are related to different formulations of the driving force p_{sg} due to energy minimisation by subgrain growth. The specific interface energy γ_{sg}, according to Read and Shockley (in [31]), of a small angle grain boundary is a function of the misfit θ

$$\gamma_{sg} = -E_0 \theta (A + ln(\theta)), \tag{4.10}$$

with

$$E_0 = \frac{Gb}{4\pi(1-\nu)} \tag{4.11}$$

and

$$A = 1 + ln\left(\frac{b}{2\pi r_0}\right) \tag{4.12}$$

as a function of the cut-off radius. For the amount of the misfit θ, caused by the dislocations in the subgrain boundary with the dislocation density ρ_b, see Eqs. 4.11 and 4.12. The approaches by Sandström, Humphreys and Saetre [30, 32] can be adapted in the case of creep by implication of the kinetics of the dislocation density in the subgrain boundaries ρ_b and therefore with a non constant specific interface energy γ_{sg}.

4.2.4 Knitting Processes

TEM-investigations showed that subgrains interact in different ways with sliding dislocations. Depending on the sign and the Burgers vector of the dislocations, it results in an integration and also disassembling of dislocations in the dislocaton network of subgrain- or cell boundaries. These mechanisms are defined according to TEM-images as knitting mechanisms. Depending on the direction of movement of the dislocation *knitting in* or *knitting out* can take place. In the model according to Ghoniem et al. [28] the region of a subgrain consists of dislocations forming the subgrain boundary and static dislocations accumulating into the subgrain. Knitting in of dislocations happens by static dislocations, i.e. mobile dislocations that cross the subgrain boundary and that are immobilised and subsequently integrated into the subgrain boundary by climbing.

The concept of *knitting out* is not exactly confining with the association of the *knitting in* mechanism. In this case dislocations are not restored, which is energetically implausibly, but new dislocations are formed similar to the Frank-Read mechanism. Argon and

Takeuchi [19] assumed dislocations, which are not perfectly stored in the subgrain, as dislocation sources. Such kind of dislocations is comparable to static dislocations and the process is only operating by thermal activation.

Rate Equations

For a description of microstructure mechanisms, the principle of rate equations can be introduced, especially to characterise thermally caused recovery of dislocations as well as knitting mechanisms. A general microstructure parameter S_i out of a certain amount of parameters is considered. The variable $S_i(t)$ is demanded, whereas the temporal variation of S_i due to the mechanism j

$$\dot{S}_i^j = f(\mathbf{S}, \sigma, T, ..) \tag{4.13}$$

is a function of the whole microstructure $\mathbf{S}$, σ, T and other influences. The account of an independent, parallel operating of several mechanisms on the considered parameter S_i leads to an addition of rate equations and the total temporal deviation $\dot{S}_i$ is derived by addition of all $\dot{S}_i^j$

$$\dot{S}_i = \sum_j \dot{S}_i^j. \tag{4.14}$$

The model according to Ghoniem et al. [28] demonstrates an approved formulation for modelling such mechanisms. The basic microstructure parameters to describe the dislocation structure are the mobile dislocation density ρ_m, the subrain radius r_{sub}, the dislocation density in the subgrain boundary ρ_b and the dislocation density ρ_s of the stored dislocations next to the subgrain boundaries.

Based on the equation for static recovery due to lattice diffusion of vacancies,

$$\frac{d\rho}{dt} = -\frac{2\rho}{\tau_c} = -8\rho^{3/2} v_c^l. \tag{4.15}$$

with τ_c as the annihilition time and v_c^l the climb velocity due to diffusion of vacancies, Ghoniem et al. assumed a thermal recovery for mobile and static dislocations

$$v_{c,m} = v_{c,m}^l + v_{c,m}^p \tag{4.16}$$

and

$$v_{c,s} = v_{c,s}^l + v_{c,s}^p, \tag{4.17}$$

with $v_{c,m}/v_{c,m}$ as the climb velocity of mobile/static dislocations, $v_{c,m}^p/v_{c,s}^p$ as the climb velocity of mobile/static dislocations due to pipe diffusion and $v_{c,m}^l/v_{c,s}^l$ denotes the climb velocity of mobile/static dislocations via lattice diffusion. The differential equation for thermal recovery of mobile dislocations results according to 4.15

$$\frac{d\rho_m}{dt} = -8\rho_m^{3/2} v_{c,m}. \tag{4.18}$$

A comparison of measured saturated dislocation densities with calculated values showed an appropriate conformity.

4.3 Concept of Threshold

The strain and shear rate as well as the gliding speed υ_g of dislocations as a function of the effective stress τ_{eff} results from

$$\dot{\gamma} = \rho \upsilon_g(\tau_{eff}, ..)b. \tag{4.19}$$

Generally the effective stress equals the applied stress σ and τ, respectively, is compensated due to

- stress fields and bulging of dislocations,
- bulging of subgrain boundaries,
- the strengthening by a second phase and
- solid solution hardening

and thus is a function of the time dependent microstructure. In the following, the influence of dislocations and configurations of dislocations on the effective stress and their contribution to the threshold stress τ_{th} respectively, is analysed.

The individual contributions of the microstructure elements, like mobile dislocations and subgrain boundaries are added according to the principle of superposition

$$\tau_{th} = \sum_j \tau_i^j, \tag{4.20}$$

and produce the total drag against deformation. τ_i^j denotes sum of the inner stresses. The approach by Taylor and Bacon [33], respectively, declares the constrained stress generated by mobile dislocations as a function of the Taylor factor α_m, the shear modulus G, the Burgers vector b and the mobile dislocation density ρ_m

$$\tau_i^m = \alpha_m G b \sqrt{\rho_m}. \tag{4.21}$$

where τ_i^m denotes the backstress due to mobile dislocations and $\alpha_m = 1$ according to Taylor and $\alpha_m = 0.84$ according to Bacon [33]. Orlova [34] founds an $\alpha_m \approx 0.52..0.78$ α_{FR} due to measured distributions of dislocation segment lengths, strong buckling of dislocations and experimental values for τ_i. The parameter α_{FR} is the Taylor factor at active Frank-Read mechanism. The resulting instable point $2R = \lambda$ and $\lambda = 1/\sqrt{\rho_m}$ from experimental investigations could result for $\alpha_{FR} = 1.2..1.8$ for the analysed dislocation networks, which would require a high strength of the dislocation joints. But according to the investigations of Plüschl (in [34]), the dislocation joints formed during deformation are weak barriers ($\alpha_m = 0.25...0.45$). The concept of a weak barrier is concerned as a marginal buckling between two barriers. The degree of buckling or the angle ϕ provides the amount of the backstress which is not considered by Taylor. Approaches for a general effect on the internal stress τ_i according to Friedel [24].

$$\tau_i = cos\left(\frac{\phi}{2}\right)^{3/2}\frac{Gb}{\lambda}\frac{ln\lambda}{2\pi} \tag{4.22}$$

and Hull and Bacon [33]

$$\tau_i = cos\left(\frac{\phi}{2}\right)\frac{Gb}{\lambda} \tag{4.23}$$

show a strong influence by ϕ. On the basis of these approaches the Taylor factor can be calculated (Fig. 4.5).

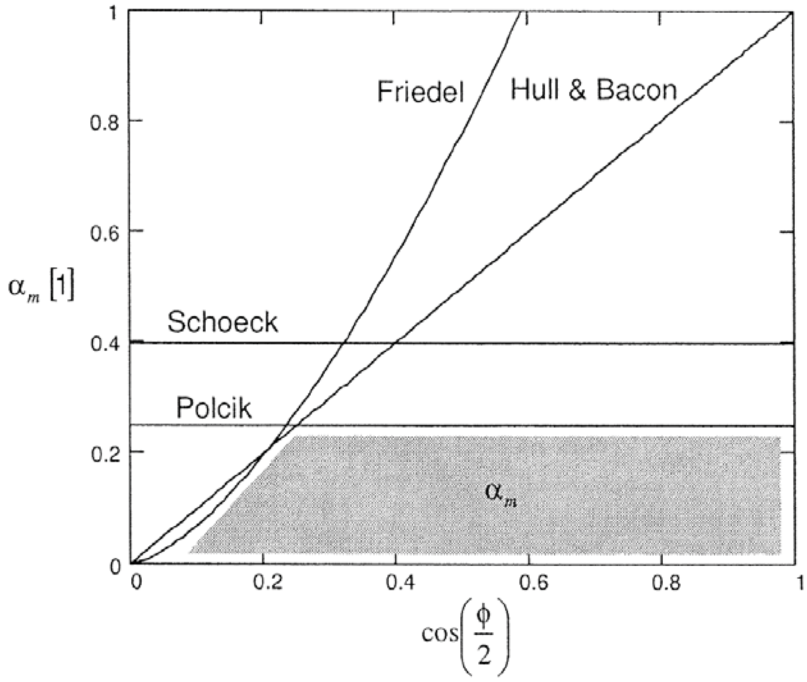

Figure 4.5: Taylor factor α_m against the angle ϕ and out of Literature according to Polcik [35], Hull and Bacon [33], Schoeck (in [34]) and Friedel [24].

Glide Kinetics

The application of hot work tool steels often lies in the range of dislocation creep, that means the plastic deformation occurs due to dislocation glide at adequate stresses. The common relation between the steady state strain rate and stress is characterised by:

- At low stresses, a stress exponent of $n \approx 1$ arises in pure metals,
- with increasing stress, the stress exponent changes and obtains characteristic values of $n \approx 3..5$,
- and with advanced stress, the exponent gets values of about $n \approx 20$ which is defined as power-law-breakdown.

The conduction in the first stress range, i.e. at low stresses, also known as *Harper-Dorn*-creep is associated with a collective migration of subgrains. The behaviour in the high stress ranges with $n \geq 3..5$ is accounted for the gliding of mobile dislocations (Fig. 4.6).

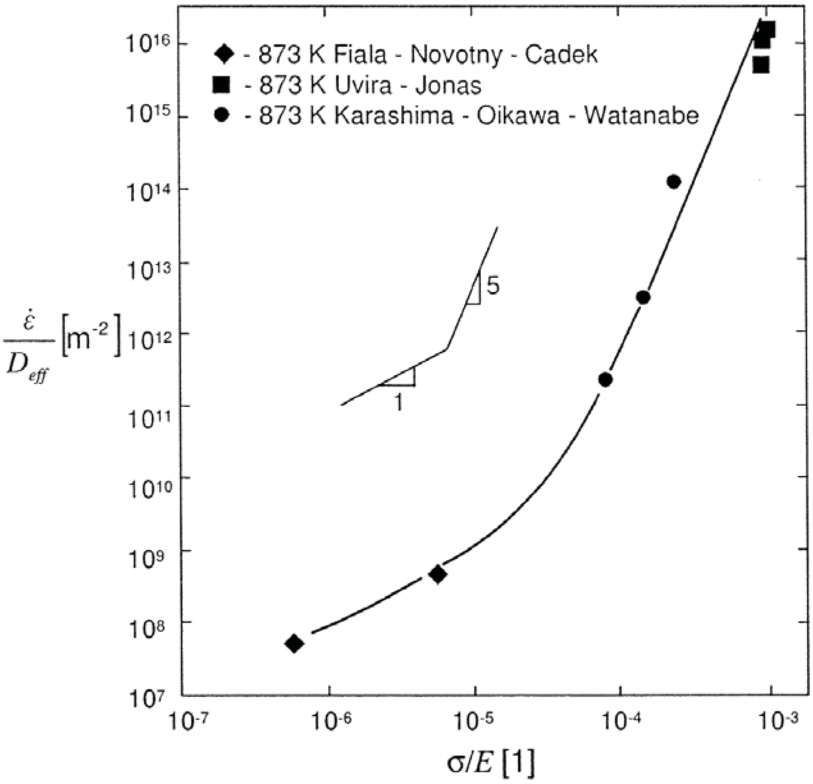

Figure 4.6: Diffusion counterbalanced steady state creep rate $\dot{\varepsilon}/D_{eff}$ against the normalised stress σ/E of $\alpha - Fe$ according to Ruano et al. [36]

The influence of precipitations on dislocations is described in section 3.1.

4.4 Joint Theories

The Three-Internal-Variables Model[37]

An appropriate representation of the hardening behaviour has to be based on microstructural state variables, which are affected by the processing history of the material. There are micromechanical models that contain explicit internal state variables, for example the model according to Chaboche [38], which have been successfully implemented in finite element codes. Although such approaches do define evolutionary equations for the internal state variables, the respective constants are commonly used as fit parameters and do not relate to specific mechanisms of microstructure evolution.

There have been numerous attempts in the past to predict work-hardening behaviour in terms of dislocation concepts, with limited success, however with regard to correctly predicting hardening behaviour in a wide field of temperature, strain rate and material chemistry. A model is presented, based on contemporary understanding of microstructural evolution and the interaction of dislocations with microstructural essentials. Such a model gives a reasonable description of the hardening behaviour and accounts adequately for changes of material chemistry, in particular for age-hardened alloys. The two effects, namely dislocation-dislocation interaction and dislocation-precipitate interaction, are separated for properly testing both parts of the model. This was accomplished by using a single-phase alloy that represents the matrix material of the corresponding precipitation-hardened alloy.

In this model, the consideration is confined to cell/subgrain-forming metals and alloys, which includes most commercial aluminium alloys, copper and nickel alloys as well as steels. With progressing strain, a cellular dislocation arrangement develops, composed of cell walls with high dislocation density (ρ_w), which enclose cell interiors of low dislocation density (ρ_i). Dislocation sources inside the material generate mobile dislocations (ρ_m), which interact with dislocations in the cell interior and dislocations in the cell walls upon their way through the crystal forced by the applied stress to accomodate the imposed strain. This interaction can result in the formation of dislocation dipoles or even annihilation of dislocations. Dipoles will finally be swept into the dislocation walls, where they are subject to thermally activated recovery processes.

Interior dislocation sources will emit dislocation loops. If we consider the loops to be of square shape with length $2L$, we represent the loop expansion by the motion of one of its segments, more specifically an edge dislocation segment. Hence, we have to keep in mind that a slip length L corresponds to a total dislocation loop length of $8L$ and a swept area of $(2L)^2$. While in the real world a loop will percolate through its slip plane and leave debris behind around circumvented impenetrable areas, we follow the classical analogon and assume instead that the considered dislocation segment will cease to move after a slip length L. This slip length is determined by obstacles which the mobile dislocations encounter on their way through the crystal. Such obstacles will be other dislocations, grain boundaries or precipitates, each of which has a specific spacing L_i^{obst}. There is no unique concept to treat the superposition of more than one obstacle type (hardening mechanism) but with increasing obstacle density (smaller obstacle spacing) the slip length must decrease. This can be accounted for by the assumption

$$\frac{1}{L} = \sum_i \frac{w_i}{L_i^{obst}} \tag{4.24}$$

(where w_i is a weight factor), since this will adjust the slip length to be dominated by the shortest spacing among the competing obstacles. Of course, this does not account for different obstacle strength or the local dislocation arrangement due to the dislocation-obstacle interaction (e.g., geometrically necessary dislocations next to non-deformable particles), but it reflects an effective influence of the ensemble of obstacles.

All dislocation-hardening models are single-crystal models in their fundamental set-up. The extension to polycrystal behaviour is accomplished by introduction of the Taylor factor α_m, which relates the macroscopically imposed strain $d\varepsilon$ to the total slip on all active glide systems in the grains $\sum d\gamma$, and thus the macroscopic flow stress σ to the acting shear stress τ in the slip systems,

$$\sigma_f = \alpha_m \tau = \frac{\sum d\gamma}{d\varepsilon}\tau. \tag{4.25}$$

In polycrystals, besides the Taylor factor, the grain size is introduced in the effective slip length equation (Eq. 4.24) to account for the limited crystallite dimensions.

Kinetic equation of state

The basic structure of the three-internal-variables model (3IVM) consists of a kinetic equation of state and a set of equations for the structure evolution as do many other dislocation models of crystal plasticity, but the 3IVM distinguishes three dislocation categories (according to Fig. 4.7): namely, mobile dislocations (ρ_m), immobile dislocations in the cell interiors (ρ_i) and immobile dislocations in the cell walls (ρ_w). For each class of dislocations an evolutionary law of the form

$$\dot{\rho}_x = \dot{\rho}_x^+ - \dot{\rho}_x^- \tag{4.26}$$

is derived below, where the index x assumes either m (mobile), i (cell interior) or w (cell wall). The $\dot{\rho}_x^+$ term represents one or more production terms of dislocations while $\dot{\rho}_x^-$ represents reduction terms. The kinetic equation of state is used to calculate the required external stress σ_{ext} to comply with the imposed strain rate $\dot{\varepsilon}$ for a given structure and temperature. Within the 3IVM, the Orowan equation

$$\dot{\gamma} = \dot{\varepsilon}\alpha_m = \rho_m b v \tag{4.27}$$

is used as kinetic equation of state. In Eq. 4.27, $\dot{\gamma}$ is the shear rate, α_m the Taylor factor of the polycrystalline material for the imposed strain path, and b the magnitude of the Burgers vector.

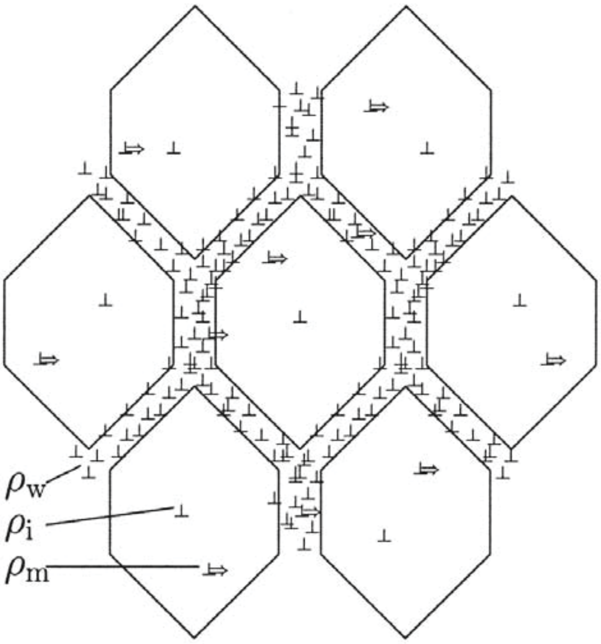

Figure 4.7: Schematic drawing of the arrangement of the three dislocation classes considered in the three-internal-variables model: mobile dislocations (ρ_m), immobile dislocations in the cell interiors (ρ_i) and immobile dislocations in the cell walls (ρ_w) [37].

By use of the Taylor factor to relate the macroscopic strain rate to the dislocation behaviour in the crystals implies, of course, that the dislocation properties are considered as population average values. The average dislocation glide velocity v depends on the effective stress $\tau_{eff} = \tau - \hat{\tau}$, where τ is the acting shear stress and $\hat{\tau}$ is the athermal flow stress.

$$v = \lambda \nu_0 exp\left(-\frac{Q}{k_B T}\right) sinh\left(\frac{\tau_{eff} V}{k_B T}\right), \tag{4.28}$$

where λ is the jump width - i.e., the mean spacing of obstacles (the immobile forest dislocations in this case), ν_0 is the attack frequency, Q is the effective activation energy for dislocation glide, and V is the activation volume. In commercial alloys the solute atoms present in the matrix result in higher values for Q than those used for pure metals. Substituting Eq. 4.28 into Eq. 4.27, Eq. 4.27 can be solved for τ_{eff}.

As the forest dislocation spacing is different in the cell interior and the cell walls, one obtains two different values for the effective stress, $\tau_{eff,i}$ in the cell interiors and $\tau_{eff,w}$ in the cell walls. In both cases the passing stress of dislocations has to be added to derive the necessary resolved shear stress in the cell interior τ_i and in the cell walls τ_w

$$\tau_x = \tau_{eff,x} + \alpha G b \sqrt{\rho_x}, \tag{4.29}$$

with the index x ($x = i, w$), α being a constant and G denotes the shear modulus, both of which are mildly temperature-dependent. The required external stress can then be calculated as

$$\sigma_{ext} = \alpha_m (f_i \tau_i + f_w \tau_w), \tag{4.30}$$

where α_m is again the Taylor factor for polycrystalline material, which can be calculated for arbitrary strain paths as a function of the total strain and f_i, f_w are the volume fractions of cell interior and cell wall, respectively.

Structure evolution equations

While the kinetic equation of state determines the flow stress for a given structure, a set of structure evolution laws is needed to calculate stress-strain curves. In the following an evolution law is derived for each of the dislocation densities considered in the model based on the underlying elementary dislocation processes. The mobile dislocations carry the plastic strain. They are assumed to penetrate both dislocation walls and cell interiors. Each mobile dislocation is supposed to travel a mean free path L_{eff} before it is immobilised or annihilated by one of the processes outlined below. A relationship between the imposed strain and the mobile dislocation density is obtained if the Orowan equation is considered on a larger time scale. In a time increment Δt, a dislocation density $\dot{\rho}_m^+ \Delta t$ is produced and immobilised after travelling the distance L_{eff}. This is associated with a strain increment, $\Delta\varepsilon$, so

$$\frac{\Delta\varepsilon}{\Delta t} \simeq \dot{\varepsilon} = \dot{\rho}_m^+ b L_{eff} \frac{1}{\alpha_m}. \tag{4.31}$$

L_{eff} is determined by the effective grain size $K_{G,eff}$, which is understood to be some constant fraction of the true grain size, and three obstacle spacings:

- the forest dislocation spacing in the cell walls L_w,
- the forest dislocation spacing in the cell interior L_i,
- and the spacing of the precipitates L_p.

The calculation of L_p and why it is introduced at this point is discussed separately below. As outlined in the previous section, it is difficult to define an effective obstacle spacing if more than a single obstacle type interacts with the moving dislocations with different strength. From the reasons given before, we arrive at

$$\frac{1}{L_{eff}} = \frac{\beta_i}{L_i} + \frac{\beta_w}{L_w} + \frac{1}{K_{G,eff}} + \frac{1}{L_p(t)}, \tag{4.32}$$

where β_i and β_w are constants, which relate the spacing of the respective dislocations (i, w) to the slip length, if only this type of dislocation would determine the slip distance L_{eff}. We assume the mobile dislocation density to be reduced by three processes, namely, by the formation of dislocation dipoles and dislocation locks as well as by annihilation.

For each process a probability for the decrease of dislocation density can be derived, as is shown below in detail for the annihilation process.

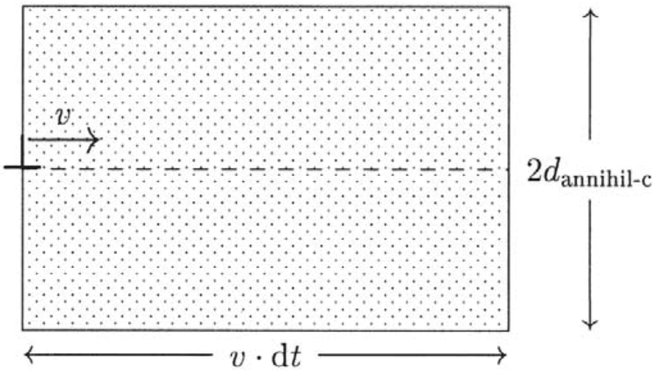

Figure 4.8: Geometrical set-up for calculating the annihilation probability [37].

Assuming that spontaneous annihilation takes place when two dislocations with antiparallel Burgers vectors come closer to each other than a critical distance $d_{annihil-c}$, the probability for the event can be calculated according to Fig. 4.8. During a time increment dt a mobile dislocation travels a distance $\nu\ dt$. Thus, spontaneous annihilation will take place if there is a suitable dislocation within the area $2d_{annihil-c}v\ dt$ (shaded area in Fig. 4.8). The number dp of mobile dislocations to serve as reaction partner within this area reads

$$dp = 2d_{annihil-c} v dt \rho_m. \tag{4.33}$$

However, for an annihilation event to take place, it is required to find an antiparallel dislocation; i.e., a dislocation on the same glide system. If the number of active glide systems is denoted n_{GS}, and one assumes an equal density of dislocations on all active glide systems, this gives rise to a normalisation term $1/n_{GS}$ for the probability calculation. Taking into account the number of active glide systems renders the rate equations texture-sensitive. Under the assumption of an equal density of positive and negative dislocations, an additional term $1/2$ must be considered as the two reacting dislocations have to be of opposite sign. The reaction rate $\dot{p}$ of an individual moving dislocation now reads

$$\dot{p} = 2d_{annihil-c} \nu \rho_m \frac{1}{2n_{GS}}. \tag{4.34}$$

The Orowan Eq. 4.27 can be used to substitute $\nu\rho_m$ to yield

$$\dot{p} = 2d_{annihil-c} \frac{\dot{\varepsilon}\alpha_m}{b} \frac{1}{2n_{GS}}. \tag{4.35}$$

For calculating the reduction rate $\dot{\rho}_m^-$ of the mobile dislocation density due to annihilation, one has to take into account that, with each annihilation event, two dislocations are eliminated and that the density of mobile dislocations is ρ_m

$$\dot{\rho}_m^-(annihil) = 2\dot{p}\rho_m = 2d_{annihil-c}\frac{\dot{\varepsilon}\alpha_m}{b}\frac{1}{n}\rho_m. \tag{4.36}$$

The formation of dislocation locks can be derived analogously. For this, the critical distance for the spontaneous formation of locks becomes d_{lock} instead of $d_{annihil-c}$. Moreover, since reaction partners can be dislocations on all other active glide systems, this leads to a factor $(n-1)/n$ instead of $1/n$. The reduction rate of the dislocation density $\dot{\rho}_m^-$ due to the formation of locks then reads

$$\dot{\rho}_m^-(lock) = 4d_{lock}\frac{\dot{\varepsilon}\alpha_m}{b}\frac{n-1}{n}\rho_m. \tag{4.37}$$

The third process taken into account is the formation of dipoles. Again, the derivation is very similar to that for annihilation. For a dipole to form the distance between the two dislocations has to exceed the critical distance for annihilation $d_{annihil-c}$ but has to be small enough to have the involved dislocations trap each other. For this to happen, the acting resolved shear stress due to the external stress has to be balanced by the stress field of the individual dislocations. This implies that the critical spacing for the formation of dipoles (d_{dipol}) scales inversely with the externally applied stress. The respective area that has to be considered amounts to $2(d_{dipol} - d_{annihil-c})v\ dt$ (shaded area in Fig. 4.9).

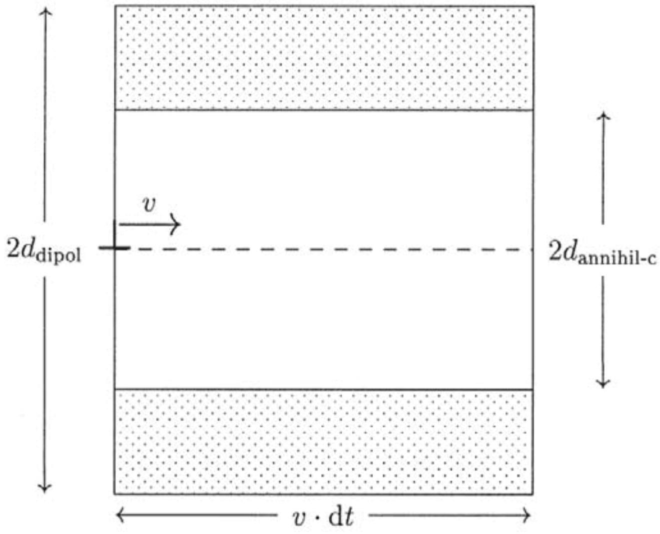

Figure 4.9: Geometrical set-up for calculating the probability for the formation of dipoles [37].

The reduction rate $\dot{\rho}_m^-$ due to the formation of dipoles then reads

$$\dot{\rho}_m^-(dipol) = 2(d_{dipol} - d_{annihil-c})\frac{\dot{\varepsilon}\alpha_m}{b}\frac{1}{n}\rho_m. \tag{4.38}$$

The second category of dislocations considered are the immobile dislocations in the cell interiors ρ_i. The rate of increase of the dislocation density inside the cells $\dot{\rho}_i^+$ is equal to the decrease of mobile dislocations due to the formation of locks, which was derived before (Eq. 4.37)

$$\dot{\rho}_i^+ = \rho_m^-(lock) = 4d_{lock}\frac{\dot{\varepsilon}\alpha_m}{b}\frac{n-1}{n}\rho_m. \tag{4.39}$$

Since locks cannot glide, the only process to decrease the immobile dislocation density is annihilation by dislocation climb. The velocity of climb v_{climb} is diffusion-controlled

$$v_{climb} = \frac{D}{k_B T}\tau A, \tag{4.40}$$

where D is the self-diffusion coefficient, and A the activation area. The rate equation for this process is then given by

$$\dot{\rho}_i^- = 2v_{climb}d_{annihil-g}\frac{1}{n}\rho_i^2. \tag{4.41}$$

The third class of dislocations are the immobile dislocations in the cell walls ρ_w. These dislocations undergo the same processes as those in the cell interiors, but there is one additional process, which contributes to the increase of this particular dislocation density. According to a former proposed model, it can be assumed that all dislocation dipoles finally end up and accumulate in the cell walls. As dipoles are created in the whole volume, but stored in the walls only, the rate of increase amounts to

$$\dot{\rho}_w^+ = \frac{1}{f_w}\dot{\rho}_m^-(dipol) = \frac{1}{f_w}2(d_{dipol} - d_{annihil-c})\frac{\dot{\varepsilon}\alpha_m}{b}\frac{1}{n}\rho_m. \tag{4.42}$$

5 Initiation and Progress of Damage

5.1 Load Mechanisms

Hot work tool steels are thermally and mechanically loaded during complex load cases. Depending on the load type, the tool will exhibit a certain lifetime. High cyclic thermal loads cause time dependent creep, cyclic mechanical loads cause time independent fatigue mechanisms. One cycle can last splits of a second to minutes and lifetime is commonly defined as number of cycles to failure. The interaction of these load cases can cause creep-fatigue, which cause an earlier component failure than only creep or fatigue.

Hot work tool steels are applicable for a temperature field over 200°C to 500°C. If the material is exposed to temperatures higher than 0.3 T_m, which means temperatures above 350°C to 400°C, the tool steel will creep (Fig. 5.1).

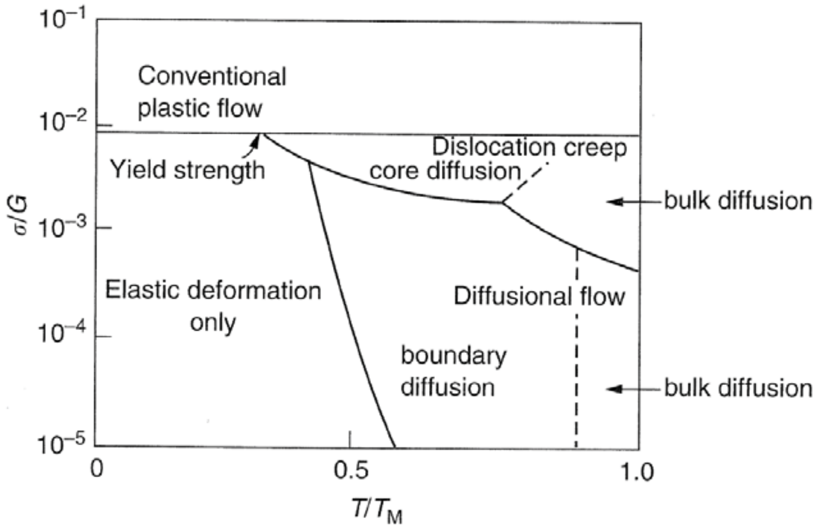

Figure 5.1: Deformation mechanisms at different stresses and temperatures [39].

The creep mechanism is naturally determined by the temperature, stresses and strain-rates, respectively. At high stresses and strain rates we can expect dislocation creep and core diffusion, at lower stresses and high homologous temperatures, diffusion creep (Coble creep via grain boundaries, and at even higher temperatures Nabarro-Herring creep via the matrix) occurs (Fig. 5.2). According to calculations of Sommitsch et. al. [40, 41], dislocation creep can be considered as the dominant creep mechanism in hot work tool steels during use.

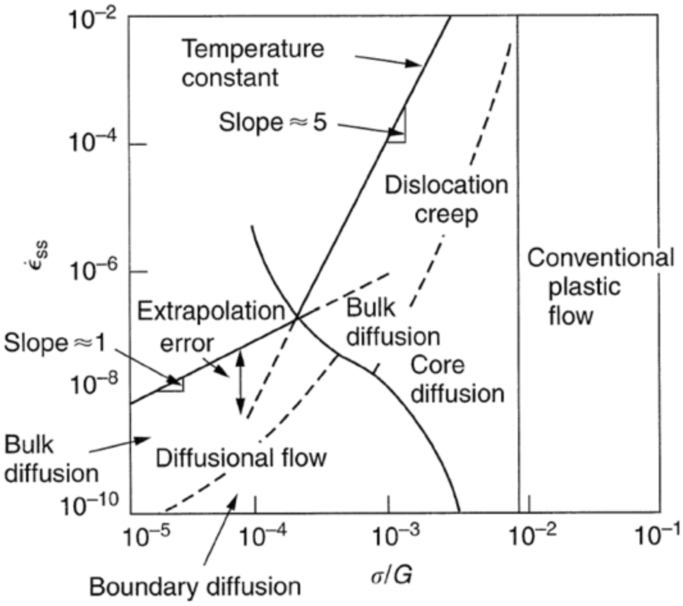

Figure 5.2: Deformation mechanisms at different strain-rates and stresses [39].

Hot work tool steels, for example for extrusion processes are supposed to carry cyclic mechanical loads, which peaks are above the elastic limit. As a consequence of these cyclic loads, generating plastic deformations, the component is not able to sustain more than 10^3 to 10^5 cycles, which is defined as low cycle fatigue.

5.1.1 Creep

At homologous temperatures of about 0.3-0.4 T_m for metals and 0.4-0.5 T_m for ceramics, the material deforms continuously under mechanical load or constant stress. Immediately after loading a certain amount of strain ε_0 is received, then the range of primary creep (creep I) or transition range occurs, in which the creep-rate decreases continuously. The subsequent steady state creep range is characterised by a constant creep rate (creep II), i.e. the strain increases proportional to the time. Finally the creep rate increases until a creep fracture occurs (creep III) [27].

The steady state creep rate depends on deformation mechanisms, i.e. the applied stress, the temperature and also on the material parameters, especially on the diffusion coefficient and the stacking-fault energy. Phenomenologically the steady state creep rate $\dot{\varepsilon}_{ss}$ depending on temperature and stress can be described by

$$\dot{\varepsilon}_{ss} = A\sigma^n, \tag{5.1}$$

with A as a constant and n denotes the stress exponent, or more explicit

$$\dot{\varepsilon}_{ss} = A\left(\frac{\sigma}{G}\right)^n exp\left(-\frac{Q}{kT}\right), \tag{5.2}$$

The behaviour of solid materials under creep load is examined by uniaxial creep tests under constant stress or load. The general creep equation describing the strain over a time period is as follows:

$$\frac{d\varepsilon}{dt} = \frac{C\sigma^{m_1}}{d^{b_1}} exp\left(-\frac{Q}{kT}\right) \tag{5.3}$$

where C is a constant depending on the material and the particular creep mechanism, m_1 and b_1 are exponents only depending on the creep mechanism, Q is the activation energy of the creep mechanism, σ is the applied stress, d_G the grain size of the material, k the Boltzmann's constant and T is the temperature. At relatively high stresses in comparison to the shear modulus, creep is controlled by the movement of dislocations. When a stress is applied to a material, dislocations move in their slip plane and this causes plastic deformation. For dislocation creep it is essential that $Q = Q_{SD}$, the activation energy for self diffusion, $m_1 = 4-6$, and b_1 is 0. Therefore dislocation creep has a strong dependence on the applied stress and no grain size dependence. Materials contain a variety of defects, for example solute atoms, that act as obstacles to dislocation motion. Creep arises from this because of the phenomenon of dislocation climb. At homologous temperatures above 0.3 T_m, vacancies in the crystal can diffuse easier to the location of a dislocation and cause the dislocation to move to an adjacent slip plane. By climbing to adjacent slip planes, dislocations can overcome obstacles to further gliding, allowing further deformation to occur. Because it takes time for vacancies to diffuse to the location of a dislocation, this results in time dependent strain or creep. The rate of dislocation glide υ_D, also known as drift velocity is

$$\upsilon_D = \frac{D_0}{kT}\tau b, \tag{5.4}$$

where D_0 denotes the diffusion coefficient, τ the acting shear stress and b the Burgers vector. The shear rate is according to Orowan [42]

$$\dot{\gamma} = \rho b \upsilon_D, \tag{5.5}$$

since ρ is associated to τ by a root-law,

$$\dot{\gamma} = \frac{\tau^2}{\alpha^2 G^2 b^2}\frac{Db^2}{kT}\tau = AG\left(\frac{\tau}{G}\right)^n \frac{D_0}{kT} exp\left(-\frac{Q_{SD}}{kT}\right). \tag{5.6}$$

A high value of n requires adequate assumptions about details of dislocation glide which imply the amount of dislocation splitting. At high homologous temperatures and relatively low stresses creep mechanisms are investigated, which are not attributed to dislocation slide, but diffusion flow. In this case the material in a grain, which is under compressive stress, is transported to regions under tensile stresses and that is the reason why a material elongates parallel to the tensile load direction. This diffusion creep can occur via the matrix (Nabarro-Herring-Creep) or at lower temperatures via grain boundaries (Coble-Creep).

Some alloys exhibit a very large stress exponent ($n > 10$), and this has typically been explained by introducing a threshold stress, σ_{th}, below which creep can't be measured. The modified power law equation then results in

$$\frac{d\varepsilon}{dt} = \dot{\varepsilon} = A(\sigma - \sigma_{th})^n exp\left(-\frac{Q}{RT}\right) \tag{5.7}$$

with $3 < n < 10$ [27].

5.1.2 Creep-Fatigue Interaction

Creep-fatigue occurs due to overlapping of high thermal loads causing creep and cyclic mechanical loads which cause fatigue. Creep can produce large strain deformation, stress relaxation, and crack initiation and growth (Fig. 5.3). For materials under fatigue and creep loading, the interaction of creep and fatigue has been observed to have different effects on the creep-fatigue life of different materials. Creep-fatigue tests were performed and found out that the creep-fatigue lifetime was significantly affected by initial creep damage on metallic alloys [22].

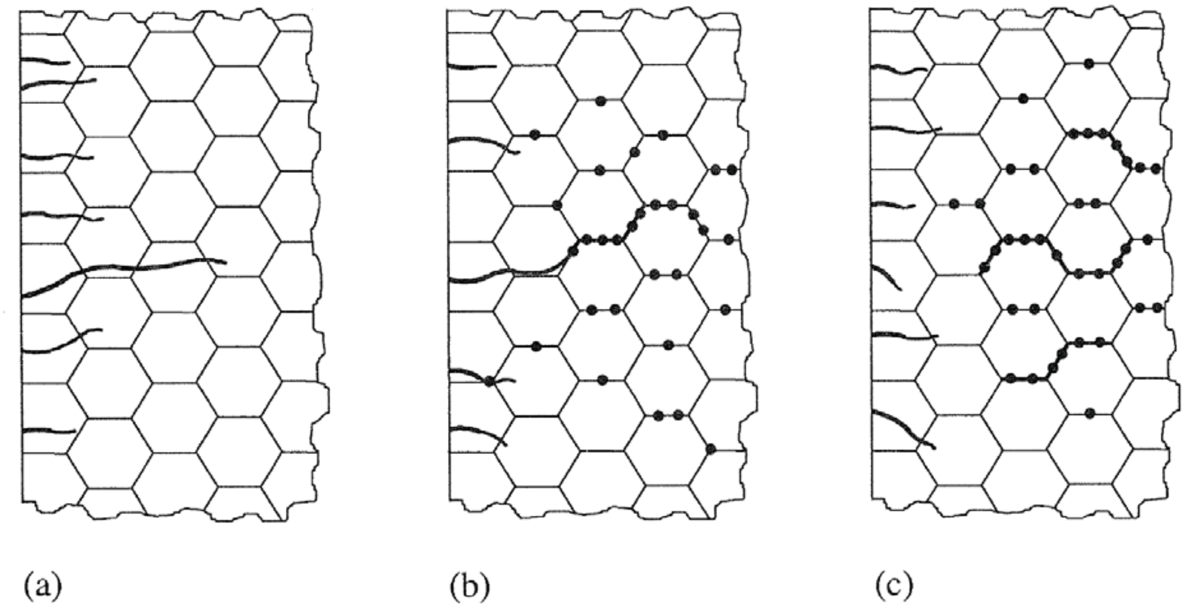

Figure 5.3: Influence of several damage mechanisms on crack progression at high-temperature alternating-deformation, whereas fatigue damage (a), creep-fatigue-alternation (b) or creep damage (c) dominates [43].

High temperature components in energy- and propulsion technology are commonly exposed to these combined thermo-mechanical load cases. Especially during run up or shut down of gas turbines the temperature changes so quickly, that time incremental temperature gradients inside one component develop. As a reason of different hot regions which expand unequally, local thermal strains and stresses result from these thermal gradients. They overlap with present mechanical loads and determine the lifetime of such components. An important aspect is the chronological compliance of temperature and strain, if they are in phase or if they exhibit a phase shift. For example, an air cooled turbine blade has a phase shift of about 180° between thermal and mechanical load at the exterior side, when there is an in-phase load at the interior side. Without cooling, the load case changes and this causes a phase shift of about $+90°$ at the exterior and $-90°$ at the interior side. Under these complex high-temperature loads, mechanisms are active which cause additional damage, compared to room temperature conditions. In this case of high temperatures and mechanical loads, time dependent deformation mechanisms occur. Despite of a low nominal stress in the supporting sections of the component, which can cause time dependent global creep in only small amounts, notches or imperfections in the material cause local superelevations of stress, which lead to intensified creep damage. The material is also influenced by environmental conditions like oxidation and corrosion. In addition to time dependent damage contributions, time independent fatigue damage mechanisms in the high cycle fatigue (HCF)-range as a reason of high frequent vibrations, as well as fatigue loads in the low cycle fatigue (LCF)-range as a reason of run up or shut down and other low cyclic mechanical loads and thermal stresses due to fluctuation of temperature, occur [44].

Hot work tool steels are commonly used for forging processes, extrusion of light alloys and processing of several materials. They get in contact with the preheated raw material, for example the billet, subsequently the forging or extrusion process is proceeded and finally after ejection of the forged component, or finished extrusion, the next cycle starts immediately, or after a process-related required operation. A preheating of dies is demanded, not to cool down the billet too much during it is in contact with the dies. This preheating is also contributing to low cycle fatigue. During the loading process, the surface of the die is heated up rapidly with a certain amount of temperature, which cause high temperature gradients and as it is constrained by the colder matrix, compressive stresses occur at the surface and tensile stresses below in bulk. The manufacturing process itself causes additional high mechanical stresses and strains in the component, overlapping with thermal loads. At the end of the manufacturing cycle, the thermal and mechanical loads, respectively, decrease and tensile stresses occur at the surface, which is the critical region for failure initiation [44].

5.1.2.1 Thermal and Thermo-mechanical Fatigue Experiments

Thermal Fatigue Experiments

In laboratory experiments it is tried to investigate the effects of the coexistant time independent and dependent loads during practical application of these high temperature materials with the aim of thermal and thermo-mechanical fatigue experiments. The thermal fatigue experiments are arranged at specimens similar to components to achieve preferably realistic conditions. Strains and stresses are generated by temperature gradients similar to the real component. Another possibility is that specimens are clamped while cyclic heated and cooled, so compressive stresses occur during heating and tensile stresses develop during thermal compression when cooling. Plastic strains arise because of the permanently clamping of the specimen. Thermal fatigue experiments can simulate operating conditions near to reality, but have in common that the occurring stresses cannot be measured, only evaluated by FEM-simulations. Furthermore, the specified parameters like total strain or plastic strain are hardly to control [44].

Thermo-mechanical Fatigue Experiments

Due to a three dimensional inhomogeneous tempereature distribution and resulting thermal strains, a thermomechanical loaded specimen is strain controlled regulated in the experiment. Hot regions are generally under compressive stresses, colder ones thereby under tensile stresses. These stresses can relax during the manufacturing process due to a high viscosity in hot regions and are reduced by inelastic deformations, which cause a stress rearrangement. Several attempts were performed for the hot-work tool steel W400, see [45].

In contrast to the afore described thermal fatigue experiments, only one volume fraction of a real component with specific temperature and load distribution is considered. In common such experiments are conducted on specimens with cylindrical or rectangular cross sections in a servo-hydraulic test device, operating in a closed regulator circuit. The specimens are exposed to a pre-defined mechanical load distribution (of stress, total strain or plastic strain) and this distribution can be calibrated independently of periodic thermal fluctuations, wherby user-defined interactions are possible. The total strain adjusted by the thermal module or the plastic strain is used as control signal. This procedure allows it to keep the value of the plastic strain as well as the plastic strain amplitude constant during the experiment by applying a triangular reference value distribution. A constant level of the plastic strain amplitude is advantageous for the interpretation of the measured cycles to fracture, because the plastic strain amplitude determines the lifetime in the LCF-range decisively. The usage of the plastic strain as control variable is also advantageous, because isothermal and mechanical behaviour of alternating deformed specimens with the same plastic strain rate can be compared. In principal, user defined load distributions and phase shifts between mechanical and thermal cycles are possible. However in practical experiments, triangular in-phase (IP) and out-of-phase (OP) specified values for strain and temperature are chosen, which simulate the worst load cases in real components and are defined as basic types of thermo-mechanical fatigue experiments.

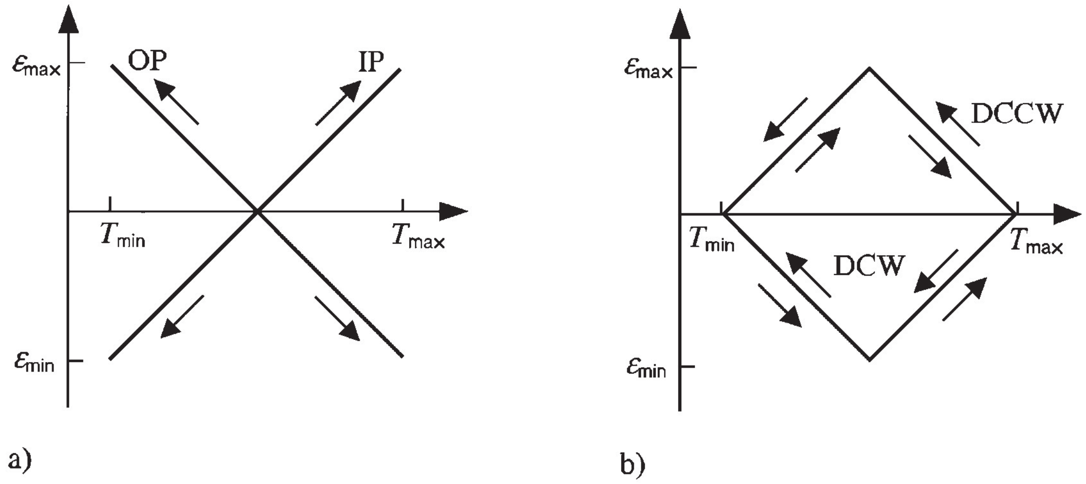

Figure 5.4: Schematical phase-distribution between temperature and strain at TME-load for an IP and OP experimental guidance (a) and a DCW and DCCW load (b) [46].

In the case of an IP-experimental guidance, the maximum tensile strain coincides with the maximum cyclic temperature, which means a phase shift of 0° between mechanical- and thermal load. Whereas under OP experimental guidance, the maximum tensile strain occurs at the minimum cyclic temperature, which conforms to a phase shift of 180° (Fig. 5.4). Beside these, TME experiments with a phase shift of ±90° between load and temperature distribution are realised, which are known as $diamond - clockwise$ (DCW) and $diamond - counterclockwise$ (DCCW) [44]. In the strain vs. temperature diagram, the load distribution curves form a tetragon, which passes clockwise or counter-clockwise (Fig. 5.4). According to a fracture mechanical consideration by [47], creep-fatigue exists, if the crack propagation rate is higher than the linear summation of the time dependent fatigue and time dependent creep conditioned crack propagation rate. The distinctive interaction of several damage mechanisms in TME-experiments is defined by a total damage, which is not determined by the aim of a simple linear summation of single active damage mechanisms. Difficulties due to the characterisation of material behaviour at thermomechanical fatigue load are, that in the TME-experiment damage mechanisms can occur, which are not observable in isothermal experiments. It can happen that the isothermal data, which are based on lifetime rules, produce non-conservative results. To describe the characteristical effects of damage mechanisms and interactions during TME-load on lifetime, Nitta and Kuwabara [48] introduced a classification of material behaviour which consists of four types (Figs. 5.5 and 5.6). This classification is based on evaluations of large experimental data on several high-temperature materials under TME-conditions [44].

Type I arises, if an IP-load shows lower fracture load cycles in comparison to an OP-load. Such a type I performance is investigated for the austenitic steel AISI 304 SS when the maximum cyclic temperature is in the region of more than 600°C where creep in style of nucleation of pores under tensile stresses plays a significant role. In this case, an OP-experimental guidance causes less damage, because the specimen is under compressive stresses at high temperatures and no pores can come into existance. In the out-of-phase experiment, transcrystalline fractures occur, whereas intercrystalline damage reduces the lifetime under IP-load. If there are strong environmental effects like oxidation or diffusion of gas like oxygen or hydrogen, the material behaves according to type O. An OP-experimental guidance leads to higher damage than in-phase loading, which attributes to significant differences in the number of cycles until crack initiation occurs (Fig. 5.5). Ferritic steels, for example 2,25 Cr-1Mo and 1Ni-1Mo-1V or the nickel-base-alloy IN 738LC show such a behaviour. The high tensile stresses affecting during the cold stage of an OP-cycle promotes crack formation in the brittle oxyde layer, which leads to an accelerated initiation of a fatigue crack in the matrix material during out-of-phase conditions. The characteristic for the material behaviour of type O is also a transcrystalline fracture mode at both types of TME-loads.

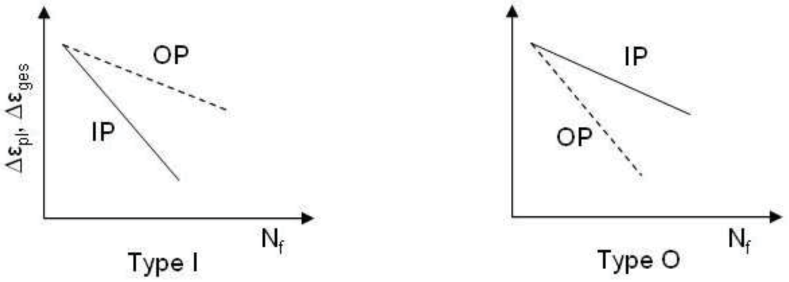

Figure 5.5: IP-load causes the shortest lifetime of a component according to *Type I*, the main damage mechanism is creep. OP-loads cause the shortest lifetimes according to *Type O*, the main damage is caused by environmental conditions [48].

Similar investigations concerning the fracture character are observed for material behaviours according to type E, which is identified that nor creep damage neither environmental conditions have a strong influence on lifetime. Independent of the load type (IP or OP), nearly the same number of cycles to fracture are incorporated, which is determined by the amount of the plastic strain amplitude and therewith by the dimension of fatigue damage (Fig. 5.6). Nitta and Kuwabara [48] detected such a material behaviour for the austenitic steel AISI 304 SS, when the maximum temperature is not too high ($\leq 550°C$), as well as for the iron-base alloy A 286 and the cobalt-base alloy FSX 414.

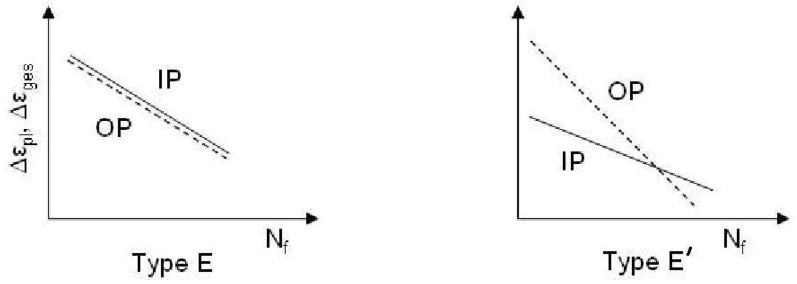

Figure 5.6: IP- and OP load show nearly the same lifetime according to *Type E*, neither environmental conditions nor creep damage dominates. At high strain amplitudes an IP-load case causes the shorter lifetime according to *Type E′*, creep only dominates at high load amplitudes [48].

These investigations definitely demonstrated, that for many materials used in components under high-temperature application, often a difficult overlapping of several damage mechanisms under TME-conditions not only causes a lifetime dependence on the maximum temperature and stress- and strain amplitude, but also additionally the lifetime dependence is controlled by the phase relation between the cyclic differing parameters temperature, stress and strain respectively [44].

5.2 Damage Mechanisms

5.2.1 Pores

5.2.1.1 Nucleation of Pores

Damage initiated by pores can be considered in form of intra- and transgranular pores, which differ in their nucleation behaviour.

Intragranular Nucleation

An intragranular pore nucleus is geometrically defined by its radius r and its wetting angle of contact ψ. Also particles can be propable locations for nucleation. The wetting angle of contact ψ for intragranular nucleation at grain boundaries results from the equilibrium of the interface energy matrix/pore γ_s (surface energy of the matrix material) and the grain boundary γ_{gb} [22].

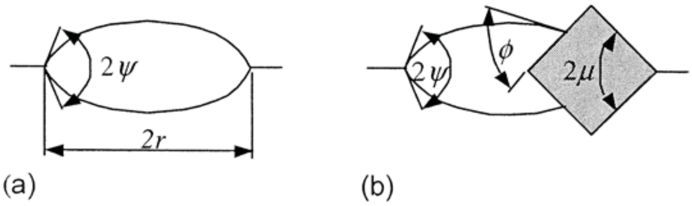

Figure 5.7: (a) Intragranular pore nucleus at a grain boundary and (b) at a cubic particle [49].

The angle ϕ for nucleation on a particle is defined by the interface energy matrix/particle γ_{ip}, matrix/pore γ_s and particle/pore γ_{sp}

$$cos\phi = \frac{\gamma_{ip} - \gamma_{sp}}{\gamma_s}. \tag{5.8}$$

For a lentoid pore, the volume V_p, the surface S_p, the substitute grain boundary surface B_p and the perimeter P_p

$$V_p = \rho^3 f_V(\psi), \tag{5.9}$$

$$S_p = \rho^2 f_S(\psi), \tag{5.10}$$

$$B_p = \rho^2 f_B(\psi), \tag{5.11}$$

$$P_p = \rho f_P(\psi) \tag{5.12}$$

can be described as a function of the radius of curvature ρ and the form functions $f_i = f(\psi)$

$$\begin{aligned} f_{V_p}(\psi) &= \frac{2\pi}{3}(2 - cos\psi + cos^3\psi), && (5.13)\\ f_{S_p}(\psi) &= 4\pi(1 - cos\psi), && (5.14)\\ f_{B_p}(\psi) &= \pi sin\psi, && (5.15)\\ f_{P_p}(\psi) &= 2\pi sin\psi. && (5.16) \end{aligned}$$

For a description of the seeds of pores at particles, the angles ϕ and μ are necessary to be defined

$$fv(\psi') = \frac{4\pi}{3}(2 - 3cos\psi' + cos^3\psi'), \tag{5.17}$$

$$\psi' = \frac{(\psi + \phi - \mu)}{2}. \tag{5.18}$$

Based on the classical nucleation theories for condensation, and for phase transformation in solid state [50], for a pore nucleus in a stress field with the stress σ, the critical radius of curvature ρ_c amounts to

$$\rho_c = \frac{2\gamma_s}{\sigma}. \tag{5.19}$$

The stress related to the critical state of a nucleus is declared as sintering stress $\sigma = \sigma_0$. The variation of the free energy through formation of a pore nucleus is

$$\Delta G_n = -\sigma \rho^3 f_v(\psi') + 3\gamma_s \rho^2 f_v(\psi'), \tag{5.20}$$

with σ as the normal stress at the grain boundary. For the case $\psi' < 0$, a negative radius of curvature ρ_c arises. As a consequence, the activation barrier ΔG_c disappears and spontaneous seeds are formed. The critical radius r_c can be obtained from the grain boundary surface and the circular area A_c with $4\pi r_c^2$

$$B_p = A_c, \tag{5.21}$$

$$\rho_n^2 f_b(\psi) = 4\pi r_c^2 \tag{5.22}$$

and

$$r_c = \frac{\gamma_s}{\sigma} \left(\frac{f_b(\psi)}{\pi} \right)^{1/2}. \tag{5.23}$$

During a descent of the effective stress at a pore with a critical radius of curvature ρ_c below a critical value, analog to $\sigma = 2\gamma_s/\rho_c$, the pore becomes instable and shrinks, that means the pore closes by sintering. The associated stress $\sigma = \sigma_0$ to the condition $\rho = \rho_c$ is declared as sinter-stress.

Basically two related conceptions, in-depth described by Riedel [49], exist. They refer to the presumption of a size distribution of pore nuclei and clusters consisted of diffusible vacancies with a number of n, respectively. Raj and Ashby [51]formulated the steady state nucleation rate J_{ss}, established from the theory of homogeneous nucleation of precipitates [52]

$$J_{ss} = \beta N \tag{5.24}$$

as a function of stress and free energy of a pore nucleus ΔG_n. The absorption rate of vacanies β is

$$\beta = \beta(n) = f_p \left(\frac{n}{f_v}\right)^{1/3} \frac{\delta_{gb} D_{gb}}{\Omega} exp\left(\frac{\sigma\Omega}{k_B T}\right) \tag{5.25}$$

with $n = 80k_BT/(\sigma\Omega)$. D_{gb} is the self-diffusion coefficient along the grain boundary and δ_{gb} the thickness of the grain boundary. In this approach, the experimental noticed influence of the strain rate $\dot{\varepsilon}$ is not considered. This is also obtained for the formulation of J_{ss} based on the attempts of Fooker-Planck and Zeldovich (in [49]), with

$$J_{ss} = \beta N Z \tag{5.26}$$

with Z as the $Zeldovich$-coefficient

$$Z = \frac{\sigma\Omega}{4\gamma_s} f_v \left(\psi'\right)^{-1/2}. \tag{5.27}$$

According to a theory related to the homogeneous nucleation of precipitates, the $Zeldovich$-coefficient concerns the following [52]: In contrast to Becker and Döring, it was considered that also overcritical pore nuclei with $r > r_c$ and $\Delta G_n > \Delta G_{n,c}$ respectively, can be dissolved. That menas that the steady state seed distribution around pore nuclei with $n > n_c$ and $r > r_c$ respectively, expands to an indiscriminately determined marginal radius r^* and n^*. This was considered by the modified $Zeldovich$-coefficient Z

$$Z = \left(\frac{-1}{2\pi k_B T} \frac{\partial^2 \Delta G_n}{\partial n^2}\right)^{1/2}. \tag{5.28}$$

The graphical interpretation of the distribution ΔG_n vs. r_n also demonstrates that the magnitude of the nucleation energy barrier in the interval k_BT below the maximum $\Delta G_{n,c}$ can be described by $1/Z$.

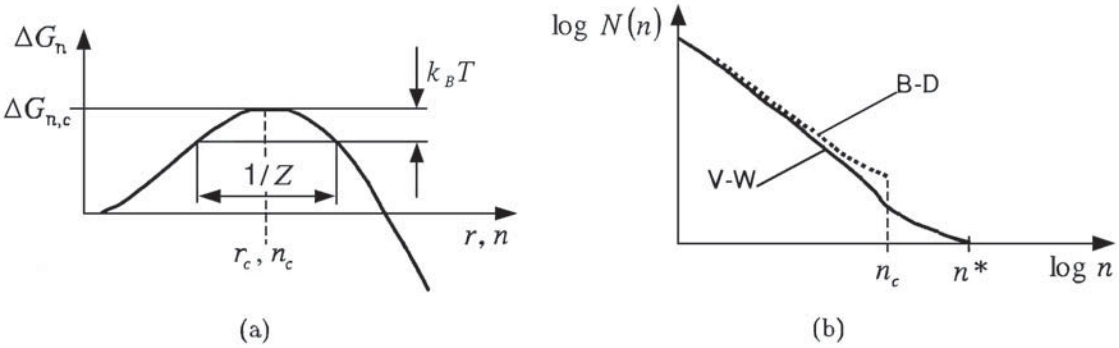

Figure 5.8: (a) Schematical distribution of the free formation energy against the cluster or nucleus radius r_n and n as the number of vacancies in one nucleus. r_c and n_c denote the critical values; (b) quasi-stationary cluster size distribution according to Volmer/Weber (V-W) and Becker/Döring (B-D) [49].

Transgranular Nucleation

Under influence of high stresses or high strains, transgranular pores accumulate. The formation of transgranular pores at stresses above the yield strength and creep is always observed only in combination to nucleation on particles. According to Martin [12], the theories of nucleation at deformation above the yield strength σ_y can be splitted up into three parts:

- Energy criteria,
- local strain criteria and
- local stress- and decohesion criteria.

In case of creep, different approaches were discussed by Goods and Brown [53]:

1. an energetical based criterion for the critical nucleation strain ε_n

$$\varepsilon_n \geq \frac{3\gamma_{sp}}{\mu_p b}. \tag{5.29}$$

   Here the possibility of relaxation around the particle is considered. Therefore it was assumed that the plastic relaxation around the particle decays parabolically. The factor μ_p denotes the shear modulus of the particle and γ_{sp} the specific surface energy.

2. Nucleation during excess of decohesion stress causes a critical nucleation strain ε_n. In comparison to the models at deformation above the yield strength σ_y, decohesion stresses, for example for a maraging steel with TiC at $\sigma_c \backsimeq 1900[MPa]$ were observed. At creep loading, the occurence of such high stresses is doubtful, because stresses are reduced due to relaxation around the particle.

5.2.1.2 Growth of Pores

Besides the alteration in the damage mechanisms, characteristic growth mechanisms are working, depending on the load cases and material conditions, which are systematically shown in several *Void Growth Mechanism Maps*. In use of the growth-models for intragranular pores, Riedel [49] calculated the growth rates of different mechanisms and generated a void growth map.

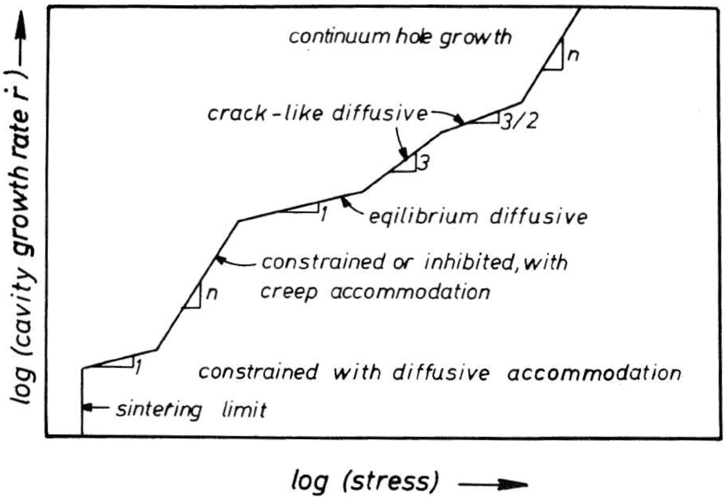

Figure 5.9: Calculated cavity growth rates, schematically [49].

Fig. 5.9 gives a simplified picture of the cavity growth rates calculated from various models and it schematically shows the ranges in which different mechanisms predominate. Of course, real materials do not necessarily exhibit all of the mechansms indicated depending on material parameters and on the cavity size and spacing. If, for example the surface diffusion coefficient is large, crack-like cavity growth may have no range of validity between equilibrium diffusive growth and plastic hole growth. Fig. 5.10 summarises the times to cavity coalescense calculated for instantaneous cavity nucleation at the beginning of a test. In many cases, the time to cavity coalescence is approximately equal to the time to rupture, but in the case of constrained growth, this relation is questionable.

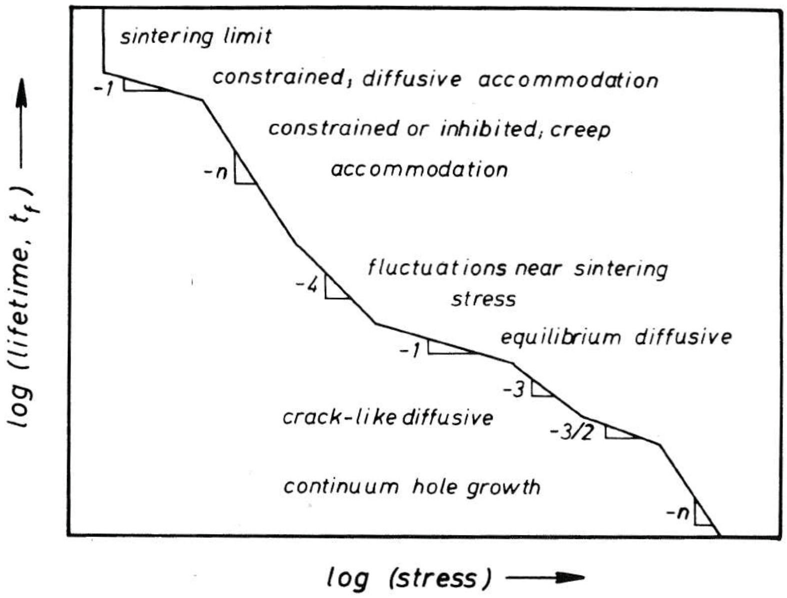

Figure 5.10: Calculated lifetimes for instantaneous nucleation, schematically [49].

- **Intragranular Pore Growth**

An intragranular pore with its characteristic geometric dimensions is shown in Fig. 5.11:

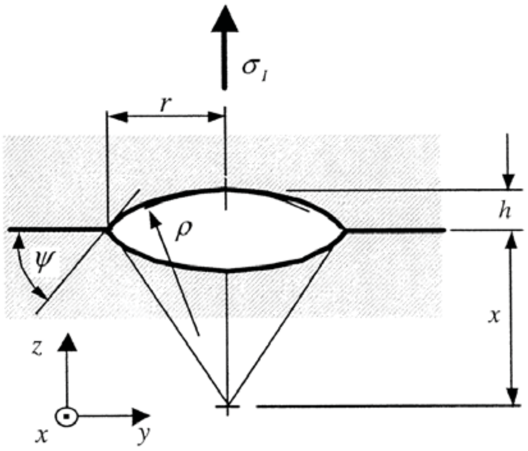

Figure 5.11: Intragranular pore with its characteristic geometric dimensions. σ_I denotes the direction of the first principle stress [22].

According to Cocks/Ashby [54] and Riedel [49], the pore growth can be controlled by

- Diffusion along grain boundaries and void surfaces,
- power law creep
- and by a combined interaction of single mechanisms.

Growth by Grain Boundary Diffusion

Based on the theory for diffusion-creep, i.e. the consideration of the normal stress distribution σ_n at a grain boundary with the displacement rate $\dot{u}_n$

$$\nabla^2 \sigma_n = \frac{k_B T}{\Omega \delta_{gb} D_{gb}} \dot{u}_n, \tag{5.30}$$

Riedel derived a relation for the grain boundary diffusion controlled growth dr/dt

$$\frac{dr}{dt} = \frac{2\Omega \delta_{gb} D_{gb} [\sigma_b - \sigma_0 (1-\omega)]}{k_B T h(\psi) q(\omega) r^2}, \tag{5.31}$$

with

$$\omega = \left(\frac{2r}{\lambda}\right)^2, \tag{5.32}$$

$$q(\omega) = -2ln(\omega) - (3-\omega)(1-\omega) \tag{5.33}$$

and

$$h(\psi) = \frac{3}{4\pi}\frac{f_v(\psi)}{sin(\psi)^3} \tag{5.34}$$

of an axisymmetric pore with the radius r. σ_b is the local stress at the grain boundary and is named facet stress. λ denotes the distance between pores, ω the damaged area, Ω the atomic volume and σ_0 the sinter stress.

Combined Diffusion

Grain boundary and void surface diffusion are operating independently from each other. Hence an additive rate attempt can be applied. Riedel [49] studied this case analytically. Consecutively the equations for growth of pores are mentioned:

$$\frac{dr}{dt} = \frac{27\Omega\delta_s D_{sf}\gamma_s}{8k_B T\lambda^3\Delta}\frac{\left\{(1+Q\Sigma\Delta)^{1/2}-1\right\}^3}{Q^3(1-\omega)^3}, \tag{5.35}$$

$$\Sigma = \frac{2\sigma\lambda}{3\gamma_s sin(\psi/2)}, \tag{5.36}$$

$$Q = \frac{3}{4}\frac{\sqrt{\omega}q(\omega)}{(1-\omega)^3} \tag{5.37}$$

and

$$\Delta = \frac{\delta_s Dsf}{\delta_{gb} D_{gb}}, \tag{5.38}$$

where δ_s and δ_{gb} denote the thickness of interfaces and grain-boundaries, D_{sf} and D_{gb} the self-diffusion-coefficient. At a high level of surface-diffusion the pore forms spherically, while at high stresses no diffusive balance takes place and the pore shapes like a crack.

Growth by Power Law Creep

A defect similar to a crack under deformation in a volume was analysed by He and Hutchinson [55]. This state approach was adapted by Riedel [49] for the case of power law creep. The temporal derivation of the volume V of the pore is

$$\dot{V} = \dot{\varepsilon}_e d_g^3 \left(1+\frac{3}{n}\right)^{-1/2} \frac{\sigma_1^\infty - \sigma_b}{\sigma_e^\infty}. \tag{5.39}$$

In contrast to the attempt by He and Hutchinson [55], the crack-length a was replaced by the grain-size d_g, and the stress σ_1^∞ was replaced by the difference between the first principal normal stress and the facet stress σ_1^∞-σ_b. The equivalent stress is denoted by σ_e^∞.

Constrained Growth

The association for this theory is as follows: under influence of local stresses σ_b, pores are growing in relation to Eq. 5.31 by grain boundary diffusion. A multiplication of this equation with the number of pores at the facet of a grain boundary results in the rate of volume $\dot{V}$. On the other hand the strain-rate $\dot{\varepsilon}_e^\infty$ in the matrix causes a volume growth rate of the crack, considered as grain boundary facet. Due to reasons of compatibility, the volume-rates have to be equal. The local stress σ_b results by equating

$$\sigma_b = (1-\omega)\sigma_0 + \frac{\sigma_1^\infty - (1-\omega)\sigma_0}{1 + 2\Omega\delta D_{gb} q' \sigma_e^\infty / [k_B T q(\omega) d_g \lambda^2 \dot{\varepsilon}_0]}, \tag{5.40}$$

where

$$q' = \pi^2 \left(1 + \frac{3}{n}\right)^{1/2}. \tag{5.41}$$

The growth equation for the radius of the pore can be obtained by introducing σ_b into Eq. 5.31

$$\frac{dr}{dt} = \frac{\sigma_1^\infty - (1-\omega)\sigma_0}{h(\psi) r^2 [q(\omega) k_B T/(2\Omega\delta D_{gb}) + q'\sigma_e^\infty/(d_g \lambda^2 \dot{\varepsilon}_e^\infty)]} \tag{5.42}$$

If the strain-rate $\dot{\varepsilon}_e^\infty$ is very high, the volume generated by the diffusion process can easily be accommodated, that means the growth equation is restricted to the diffusive influence. This case is described as *unconstrained* growth. In contrast to *constrained* growth, i.e. at lower strain rates $\dot{\varepsilon}_e^\infty$ and $\sigma_b \rightarrow \sigma_0$, the growth rate is controlled by $\dot{\varepsilon}_e^\infty$. Riedel [49] assumed that the (all of the same size) pores are evenly distributed and described by a distance λ. The comparison of corresponing calculated results with data of experiments on ferritic steels shows that the damage behaviour by an assumption of continuous intragranular nucleation can be described very well by this model of growth. In contrast to this, the model by Cocks and Ashby [54] is based on modified conceptions by the point of view that pores do not form on all facetts, which lie perpendicular to the first principal normal stress. By means of the compatibility condition, the strain rates at the damaged facetts, and facetts exempt from pores, have to be the same. Therefore a new variable L was introduced, which characterises the distance of the pore clusters between the damaged facetts.

- **Transgranular Pore Growth**

Analogous to nucleation of transgranular pores, the growth by grain boundary or surface diffusion is assumend to be not influenced by vacancies, because the transgranular pores don't have a connection to the grain boundaries. Cocks and Ashby [54] adapted a model for intragranular pore growth at power-law-creep for transgranular pore growth (Fig. 5.12).

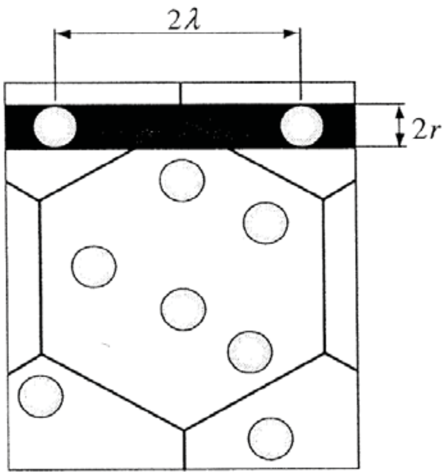

Figure 5.12: Homogeneous distribution of transgranular pores [54].

The representative volume in this approach is supposed to be a disk with a thickness of $d = 2r$. With the evolution equation of the damaged area

$$\frac{1}{\dot{\varepsilon}_0}\frac{df_h}{dt} = \beta\left[\frac{1}{(1-f_h)^n} - (1-f_h)\right]\left(\frac{\sigma_e}{\sigma_0}\right)^n, \tag{5.43}$$

it is possible to derive a relation for the temporal alteration of the pore radius by

$$\begin{aligned}\frac{df_h}{dt} &= \frac{d}{dt}\left[\left(\frac{r}{2\lambda}\right)^n\right] \\ &= \frac{4r}{\lambda^2}\frac{dr}{dt} - \frac{8r^2}{\lambda^3}\underbrace{\frac{d\lambda}{dt}}_{=0}.\end{aligned} \tag{5.44}$$

Therefore a relation between dr/dt and df_h/dt is given by

$$\begin{aligned}\frac{dr}{dt} &= \frac{df_h}{dt}\frac{\lambda^2}{4r} \\ &= \frac{\beta\lambda^2}{4r}\left[\frac{1}{(1-f_h)^n} - (1-f_h)\right]\dot{\varepsilon}_e\end{aligned} \tag{5.45}$$

with $\beta \sim 0.6$ at uniaxial tensile load.

Damage caused by Pores

To make a precise prediction for the point in time when failure occurs, an indicator is required. This indicator has to be described by the parameters like pore radius, pore density and distance of pores for both, intra- and transgranular pores. The coagulation of pores to cracks (see Fig. 5.13) is not considered in that way, but as an increase of the stress due to reduction of area, which leads to the changeover to fracture mechanical theory [22].

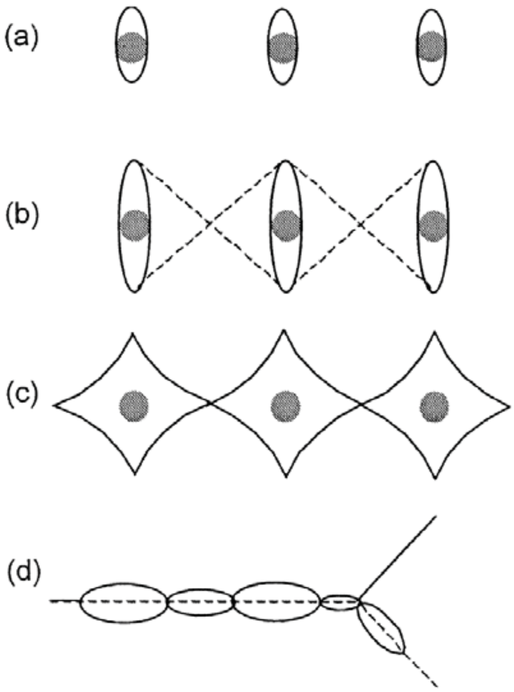

Figure 5.13: Coagulation of trans- and intragranular pores. (a), (b) and (c) illustrate the growth and coalescence of transgranular pores, while in (d) the critical state of coagulation of intragranular pores at a grain boundary is depicted [12].

5.2.2 Cracks

5.2.2.1 Initiation of Cracks by Coagulation of Pores

In the domain of tertiary creep (creep III), intragranular and transgranular pores coagulate to micro cracks and these micro cracks form macro cracks. At damage by transgranular failure $\sigma > \sigma_y$, the model according to Brown and Embury (in [12]) provides a suggestion for the amount of strain, which is necessary to cause coagulation of pores. According to this model, the transgranular pore seeds have reached the magnitude of the particle soon after decohesion, on which the nucleation takes place. The strain, until coalescence arises, amounts to

$$\varphi_g = \frac{1}{C} ln(1+\varepsilon_g) \tag{5.46}$$

with $C = 1..2$ and

$$\varepsilon_g = \frac{\lambda - 2r}{2r}. \tag{5.47}$$

By insertion for $\lambda = \lambda_p$, φ_g follows to

$$\varphi_g = \frac{1}{C} ln\left(\sqrt{\frac{\pi}{6 f_v^p}} - \sqrt{\frac{2}{3}}\right). \tag{5.48}$$

The distinctive elongation of pores in the direction of the first principal normal stress, ivestigated by Brown and Embury, occurs at only a small value of triaxial stresses. With increasing triaxiality, the transgranular pores form spherically.

The point is now, to find suitable failure criteria and an indicator to predict the moment of failure. Therefore this critical state or indicator has to be described by available parameters like pore radius, pore density and distance between intra- and transgranular pores. The coagulation of pores into cracks was not considered, but the increase of stress due to the diminution of cross section. At the time of coagulation of pores, it is necessary to consider fracture mechanical theories [22].

If given parameters are applied, three different failure criteria can be implemented:

- To reach a critical stress,
- the excess of a critical damage-parameter D_{crit},
- and the coagulation of pores, if $2r \geq \lambda$.

5.2.2.2 Fatigue Crack Initiation

Polycrystalline metals have a variety of intrinsic stress concentration features, such as grain boundaries, triple junctions and inclusions, which can rapidly initiate a crack under an applied cyclic load. Therefore, even with a highly polished surface, cracks can still initiate in these regions so long as the resolved shear stresses in the vicinity of these inherent microstructural defects are sufficiently high and aligned favourably along preferential slip systems of the material crystal structure (e.g. $\langle 111\rangle\{110\}$ systems in face-centered cubic (fcc), $\langle 110\rangle\{111\}$ in base centered cubic (bcc) metals). If considered at the sub-micron level, lattice defects such as dislocations and the evolving dislocation structures ultimately control the initiation process. There are additional considerations when analysing fatigue behaviour, such as the material and shape of an engineering component, as well as, the sequence, mode and magnitude of cyclic loading [56].

For early crack initiation studies, four point bending is a suitably convenient test setup as is keeps the specimen geometry simple. The advantage lies in confining the study to the surface microstructure, where a uniform tensile stress is applied to the surface under a bending load. The application of a relatively low load under high frequency also implies that the local plasticity induced will be small in the early stages of testing. Hence, surface grain interaction with suburface grains should have less influence so long as it can be ensured that the average grain size of the specimen surface microstructure is larger than the local regions of plastic deformation. If this is the case, only the surface microstructure needs to be described, which considerably simplifies procedures involving microstructure characterisation. Such two-dimensional analyses are now routinely conducted using EBSD [56].

Experimental Study

For the four point bend setup, the bending moment is uniform along the inner fibre of the beam, according to beam theory. On the top surface, where the investigations of this study were made, the tensile stress is highest and also uniform across the with. This raises the likelihood of fatigue cracks initiating on the surface and narrows the region to be studied, which lies near the specimen mid-point on the top surface (Fig. 5.14). The rectangular aluminium test piece had a purity of 99.99% [56].

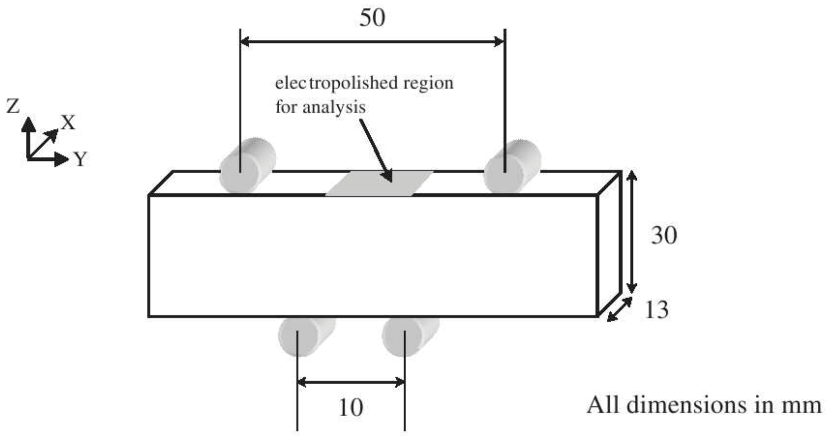

Figure 5.14: Schematic diagram of the four-point bend test and specimen geometry for high-cycle fatigue testing [56].

The initial microstructure of a representative section of the polished region is shown in Fig. 5.15 and it is observed that the grains are equaxed and relatively large.

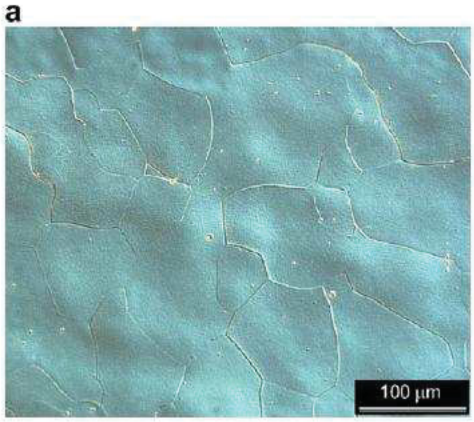

Figure 5.15: Initial microstructure of a selected region of the electropolished specimen surface [56].

After 5×10^5 cycles fatigue cracking became prominet, at which time the test was stopped. Fig. 5.16 shows the region under low (a) and high (b) magnifications, where the formation of slip lines and bands, as well as early crack initiation and growth, are clearly seen. Such cracks are typical of Stage I fatigue cracking, initiating at grain boundaries, triple junctions and slip bands.

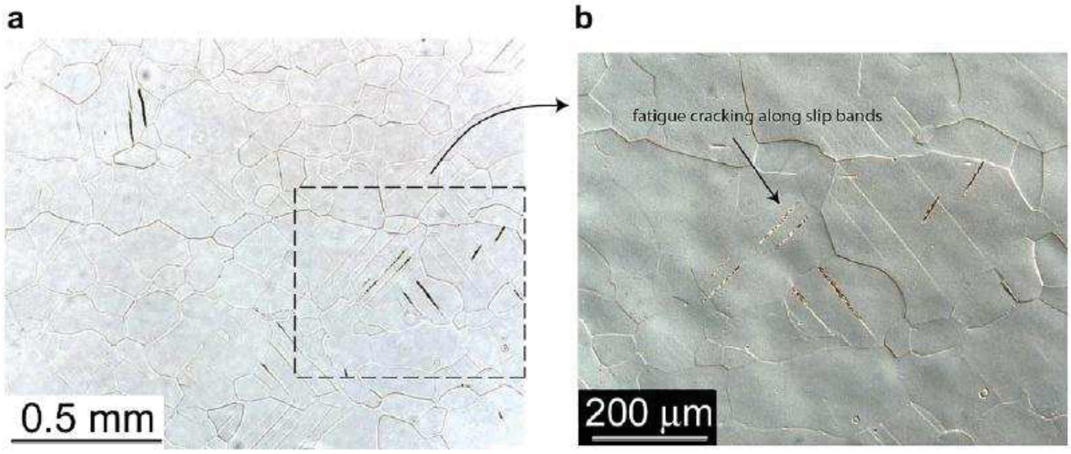

Figure 5.16: (a) Low and (b) high magnifications of the microstructure of a region after 5×10^5 fatigue cycles, emphasising the formation of slip bands, crack initiation and early crack growth [56].

Crack growth was frequently observed to occur along slip bands, thus highlighting their crystallographic nature. Crack growth was also confined to within grain boundaries and observed to be arrested once an opposite grain boundary was reached. It was also observed that the fatigue cracks were predominantly found in grains above the average grain size [56].

6 Damage Models

A variety of damage models exists, for example plastic energy criteria (Freudenthal resp. Clift [57, 58], Cockroft and Latham [59], Argon and Im [60, 61]), as well as integral over effective strain criteria (Ayada [62], Oh and Kobayashi [63], Osakada [64, 65]), empirical criteria (Kuhn [66], Sowerby [67, 68]), void based criteria (McClintock [69], Rice and Tracey [70], Oyane [71, 72], Gosh [73]) Yield criteria based on void volume fraction (Gurson [74], Gurson-Tvergaard-Needleman [75–77], Shima-Oyane [78], Green [79]) and continuum damage mechanics criteria (Lemaitre [80, 81], Chaouadi [82], Tai and Yang [83]). To describe creep and creep-fatigue damage, some exemplarily selected void based criteria and continuum mechanical methods are presented in this chapter.

6.1 Void based Criteria

6.1.1 Model according to McClintock

The McClintock criterion [69] is an integral approach to describe failure by cylindrical void initiation and growth followed by coalescense. The fracture should occur when one of the damage variables C_i, like the void radius, void volume fraction or stress related parameter, reaches a critical value. The criterion is as follows

$$C_i = \int_0^{\bar{\varepsilon}_f} \left[\frac{\sqrt{3}}{2(1-n)} sinh \left(\frac{\sqrt{3}(1-n)}{2} - \frac{\sigma_i + \sigma_j}{\bar{\sigma}} \right) + \frac{3}{4} \frac{\sigma_i - \sigma_j}{\bar{\sigma}} \right] d\bar{\varepsilon} \tag{6.1}$$

with i = 1,2,3; and j = 2,3,1. Important in this criterion is that there is a very strong inverse dependence of fracture strain on hydrostatic tension in plastic material. A very strong effect of triaxiality in reducing the fracture strain was observed, especially in non hardening material. The damage rate depends on the average of the two transverse stresses in non hardening materials, whereas it depends only on the stress normal to the fracture plane in viscous materials.

6.1.2 Model according to Rice and Tracey

The approach according to Rice and Tracey [70] considers the ductile growth of voids in continuum plasticity and also discussed related results, e.g. a long cylindrical void considered by McClintock [69]. In this formulation, fracture occurs when the radius r of the spherical cavities reaches a critical value r_c:

$$ln \left(\frac{r}{r_c} \right) = c_1 \bar{\varepsilon} exp \left(\frac{c_2 \sigma_H}{\bar{\sigma}} \right) \tag{6.2}$$

with c_1 and c_2 as material parameters, $\bar{\sigma}$ denotes the Von Mises equivalent stress and σ_H the hydrostatic (mean) stress.

A modified Rice and Tracey criterion [84] was introduced for application in finite element programs for fracture analysis with the critical value C

$$C = \int_0^{\bar{\varepsilon}_f} exp\left(\frac{c_m \sigma_H}{\bar{\sigma}}\right) d\bar{\varepsilon} \tag{6.3}$$

with c_m as material parameter.

6.1.3 Yield Criteria based on Void Volume Fraction

Gurson and Gurson-Tvergaard-Needleman Model

The following criteria define new flow rules for voided materials, which depend on the current void volume fraction C_ν,

$$\begin{aligned} C_\nu &= \frac{V - V_M}{V} = 1 - \frac{V_M}{V} \qquad (6.4) \\ \Rightarrow V &= \frac{V_M}{1 - C_\nu} \end{aligned}$$

and

$$\frac{dV}{dC_\nu} = \frac{V_M}{(1 - C_\nu)^2} \tag{6.5}$$

with V denoting the volume and V_M as the incompressible volume of the matrix material. With the Eqs. 6.4 and 6.5 the change of the volumetric strain $d\varepsilon_\nu$ can be obtained

$$d\varepsilon_\nu = \frac{dV}{V} = \frac{dC_\nu}{(1 - C_\nu)} \tag{6.6}$$

and the volumetric strain can also be calculated

$$d\varepsilon_\nu = d\lambda \left(\frac{9}{2} C_\nu \sigma_H\right). \tag{6.7}$$

Subsequently, an expression for the non-negative proportionality factor $d\lambda$ is gained by substituting Eq. 6.6 into Eq. 6.7:

$$d\lambda = \frac{2 dC_\nu}{9 \sigma_H C_\nu (1 - C_\nu)} \tag{6.8}$$

The change of the strain components $d\varepsilon_i$ can be calculated with the proportionality factor $d\lambda$, the normal anisotropy strain ration $\bar{r}$, the principal stress components σ_i, the hydrostatic stress σ_H, and the current void volume action C_ν,

$$d\varepsilon_1 = d\lambda\left\{\frac{1}{1+\bar{r}}[2(1+\bar{r})\sigma_1 - 2\bar{r}\sigma_2 - 2\sigma_3] + \frac{3}{2}C_\nu\sigma_H\right\}, \tag{6.9}$$

$$d\varepsilon_2 = d\lambda\left\{\frac{1}{1+\bar{r}}[2(1+\bar{r})\sigma_2 - 2\bar{r}\sigma_1 - 2\sigma_3] + \frac{3}{2}C_\nu\sigma_H\right\}, \tag{6.10}$$

$$d\varepsilon_3 = d\lambda\left\{\frac{1}{1+\bar{r}}[-2\sigma_1 - 2\sigma_2 + 4\sigma_3] + \frac{3}{2}C_\nu\sigma_H\right\}. \tag{6.11}$$

$d\lambda$ can also be expressed in the following form:

$$d\lambda = \frac{1}{2(1-C_\nu}\frac{d\bar{\varepsilon}_M}{\bar{\sigma}_M}, \tag{6.12}$$

and by substituting Eq. 6.8 into Eq. 6.12, an expression for the dependence of the effective matrix strain $\bar{\varepsilon}_M$ on the current void volume fraction is gained as

$$\frac{d\bar{\varepsilon}_M}{dC_\nu} = \frac{4\bar{\sigma}_M}{9\sigma_H C_\nu}. \tag{6.13}$$

Different yield criteria exist, which provide the expressions for the effective stress on the matrix material $\bar{\sigma}_M$. With $d\lambda$ from Eq. 6.8, the principal strain components ε_i can be calculated, and thereby also the volumetric strain ε_ν. From this procedure, a dependence of the strain on the void volume fraction is achieved and the fracture should occur when a critical C_ν value and therefore the corresponding critical strain is reached.

Gurson [74] proposed a yield function which is based on an upper bound solution for spherically symmetric deformation of rigid perfectly plastic materials around a single spherical void

$$\bar{\sigma}^2 = \bar{\sigma}_M^2(1+C_\nu^2) - 2C_\nu\bar{\sigma}_M^2 cosh\frac{3\sigma_H}{2\bar{\sigma}_M}. \tag{6.14}$$

Tvergaard and Needleman [75–77] analysed the beginning and growth of plastic flow localisation for solids with initial imperfections numerically and modified Gursons model which arises now to

$$\bar{\sigma}^2 = \bar{\sigma}_M^2(1+q_1^2C_\nu^2) - 2C_\nu q_1\bar{\sigma}_M^2 cosh\frac{3q_2\sigma_H}{2\bar{\sigma}_M}, \tag{6.15}$$

where q_1 and q_2 are fit parameters, introduced to drive the predictions of the model into closer agreement with numerical analyses for deformations of materials with periodically distributed circular cylindrical voids or sherical voids.

The modification of Gurson's model by Tvergaard accounts in a global way for the non-uniform stress field around each void and also for the interaction between neighbouring voids [85]. Tvergaard also considered imperfections in the form of locally higher concentrations of void nucleating particles. The material failure is not directly attributed to the coalescence of voids, like it is assumed in Gurson's model [74], but to the apparent loss of active material volume.

6.2 Continuum Damage Mechanics Criteria

6.2.1 Effective Stress Concept according to LeMaitre

The effective stress concept according to LeMaitre [80] describes the process of material damage and resulting increase of stress due to diminution of the load carrying cross section. If the representative volume element (the representative volume element method is described more detailed in 8.3) of Fig. 6.1 is loaded by a force $\vec{F} = \vec{n}F$, the usual uniaxial stress is:

$$\sigma = \frac{F}{S}. \tag{6.16}$$

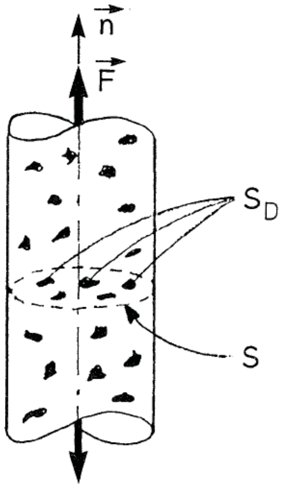

Figure 6.1: One-dimensional damaged element [80].

If all the defects are open in such a way that no microforces are acting on the surfaces of microcracks or microcavities represented by S_D, it is convenient to introduce an effective stress $\hat{\sigma}$ related to the surface that effectively resists the load, namely (S - S_D):

$$\hat{\sigma} = \frac{F}{S - S_D}, \tag{6.17}$$

and introducing the damage variable $\omega = S_D/\omega$,

$$\hat{\sigma} = \frac{F}{S\left(1 - \frac{S_D}{S}\right)}, \tag{6.18}$$

or

$$\hat{\sigma} = \frac{\sigma}{1 - \omega}. \tag{6.19}$$

This definition is valid for the effective stress on the material in tension. In compression, if some defects close, the damage remaining unchanged, the surface that effectively resists the load is larger than S - S_D. If all the defects close, the effective stress in compression $\hat{\sigma}$ is equal to the usual stress σ. The definition of the "effective" area of microcracks δS_D, "effective" has to be understood as "strength", taking into account the microstress concentrations and mutual interactions of defects loaded in tension or shear. Only micromechanics may give a precise meaning of this concept which will be taken into account globally at the mesoscale through identification of the damage variable by means of its coupling with elasticity or plasticity.

A way to avoid a micromechanical analysis for each type of defect and type of damage is to postulate a principle at the mesoscale, which leads to the strain equivalence principle. In thermodynamics, the method of local state assumes that the thermomechanical state at a point is completely defined by the time values of a set of continuous state variables depending upon the point considered. This postulate applied at the microscale imposes that the constitutive equations for the strain of a microvolume element are not modified by a neighbouring microvolume element containing a microcrack. Extrapolating to the mesoscale, this means that the strain constitutive equations written for the surface δS - δS_D are not modified by the damage or that the true stress loading on the material is the effective stress $\hat{\sigma}$ and no longer σ. The following principle results [80]:
"Any strain constitutive equation for a damaged material may be derived in the same way as for a virgin material except that the usual stress is replaced by the effective stress"

This means, that the undamaged material with $D = 0$ and $\varepsilon = f(\sigma, ...)$ is from the same derivation as the damaged material with $0 < \omega < 1$ and $\varepsilon = f(\sigma/(1-\omega), ...)$. This statement is a principle because it has been demonstrated only in some particular cases of damage through homogenisation techniques and can be applied either to elasticity or plasticity.

6.2.2 Model by Yeh and Krempl

An incremental multiaxial life prediction law (IMLP) is proposed in this model which consists of the three-dimensional thermoviscoplasticity theory based on overstress (TVBO) combined with a multiaxial damage accumulation law (MDA) to compute the life-time or cycles-to-crack initiation [86].

Thermoviscoplasticity Theory Based on Overstress (TVBO)

This theory developed by Lee and Krempl is for infinitesimal strain and orthotropy. It is of unified type and does not use a yield criterion and loading/unloading conditions. The elastic strain is formulated to be independent of thermomechanical path and the inelastic strain rate is a function of overstress, the difference between the stress σ, and the equilibrium stress g. The long-term asymptotic values of stress, equilibrium stress, and kinematic stress rates, which can be obtained for a constant mechanical strain rate and ultimately constant temperature, are assumed to be independent of thermal history as are the ultimate levels of the rate-dependent overstress and of the rate-independent contribution to the stress. Therefore, the material functions and constants can in principle be obtained from isothermal tests within the temperature range of interest.

All material constants can be functions of temperature. This dependence is not explicitly displayed. The temperature dependence can be the usual Arrhenius relation or can deviate from that model [86].

Flow laws

In the context of an infinitesimal theory, the total strain rate, $d\varepsilon/dt$, is considered to be the sum of elastic, $d\varepsilon_{el}/dt$, inelastic, $d\varepsilon_{in}/dt$, and the thermal strain rates, $d\varepsilon_{th}/dt$,

$$\dot{\varepsilon} = \dot{\varepsilon}_{el} + \dot{\varepsilon}_{in} + \dot{\varepsilon}_{th} \tag{6.20}$$

For each strain rate, a constitutive equation is postulated. The elastic strain is assumed to be independent of thermal history, therefore

$$\dot{\varepsilon}_{el} = \frac{d}{dt}(\mathbf{C}^{-1}\sigma) = \mathbf{C}^{-1}\dot{\sigma} + \dot{\mathbf{C}}^{-1}\sigma \tag{6.21}$$

where $\mathbf{C}^{-1}$ is the compliance matrix. The additional term $\dot{\mathbf{C}}^{-1}\sigma$ contributes to the total strain rate for temperature-dependent elastic material properties. It insures that the elastic behaviour is path-independent.

The inelastic strain rate is only a function of the overstress $\mathbf{x}$. It denotes the difference between the stress σ and the equilibrium stress $\mathbf{g}$, a vector state variable of the theory. Accordingly,

$$\dot{\varepsilon}_{in} = \mathbf{K}^{-1}\mathbf{x} \tag{6.22}$$

The viscosity matrix $\mathbf{K}^{-1}$ controls the rate dependence through the positive, decreasing viscosity function $k[\Gamma]$. The thermal strain rate is given by

$$\dot{\varepsilon}_{th} = \alpha[T]\dot{T} \tag{6.23}$$

with $\alpha[T]$ as the temperature-dependent coefficient of the thermal expansion vector. $\dot{T}$ is the temperature difference from some datum temperature.

The Incremental, Multiaxial Damage Accumulation Law

The multiaxial damage accumulation law (MDA) is proposed based on the modification of the incremental life prediction law for uniaxial creep-fatigue interaction. The model includes the effect of hydrostatic stress on creep and fatigue damage. The importance of hydrostatic stress on the low-cycle fatigue life has been acknowledged [87]. Ductile materials can become brittle under hydrostatic tension, while brittle materials may become ductile under hydrostatic pressure. To model the hydrostatic effects, a triaxiality factor T_F $(=\sigma_{kk}/\sigma_{eff,M})$ is used in the model, where σ_{kk} is the first stress invariant and $\sigma_{eff,M}$ is the Von Mises effective stress. The MDA is intended for the prediction of crack initiation, which is assumed to occur along the plane of maximum inelastic shear strain rate [88]. The creep damage is assumed to be of cavity type, which initiates on grain boundaries normal to the maximum principal tensile stress direction [89]. The proposed incremental multiaxial damage accumulation law consists of a fatigue and a creep damage rate equation $\dot{\omega}_f$ and $\dot{\omega}_c$, respectively. Damage is only a counter and its evolution does not influence the constitutive equations. Fatigue and creep damage are set to be zero initially for a virgin or fully annealed material, and crack initiation occurs if the sum of fatigue and creep damage reaches 1. The incremental law is then given as

$$\dot{\omega}_f = \frac{L_f^{\pm}}{T_f}|\frac{\dot{\varepsilon}_{in}^s}{\dot{\varepsilon_f}}|^{n_f}|\frac{\sigma_{eff,M}}{\sigma_f}|^{m_f} MF_f \tag{6.24}$$

and

$$\dot{\omega}_c = \frac{L_c^{\pm}}{T_c}|\frac{\dot{\varepsilon}_{in}^s}{\dot{\varepsilon}_c}|^{n_c}|\frac{\sigma_{eff,M}}{\sigma_c}|^{m_c} MF_c, \tag{6.25}$$

where

$$MF_f = 1 + a_k(1 - T_f)^{m_f} \tag{6.26}$$

and

$$MF_c = 1 + b_k(1 - T_c)^{m_c}. \tag{6.27}$$

Failure is said to occur when

$$\omega_f + \omega_c = 1. \tag{6.28}$$

$L_f^{\pm}$ is the fatigue loading function which models the effects of multiaxial loading and temperature T. It is assumed to be controlled by the ratio of $\dot{\varepsilon}_{in}^n$ and $\dot{\varepsilon}_{in}^s$, where $\dot{\varepsilon}_{in}^s$ is the value of the normalised maximum inelastic shear strain rate, and $\dot{\varepsilon}_{in}^n$ is the value of the normalised inelastic strain rate perpendicular to the plane on which $\dot{\varepsilon}_{in}^s$ acts [88, 89]. Normalised means, that the multiaxial strain rates are reduced in comparison to the uniaxial value for uniaxial loading. Accordingly,

$$\dot{\varepsilon}_{in}^s = \frac{2}{3}|\dot{\varepsilon}_{in}^1 - \dot{\varepsilon}_{in}^3| \tag{6.29}$$

and

$$\dot{\varepsilon}_{in}^n = 2(\dot{\varepsilon}_{in}^1 + \dot{\varepsilon}_{in}^3), \tag{6.30}$$

where $\dot{\varepsilon}_{in}^1$, $\dot{\varepsilon}_{in}^2$ and $\dot{\varepsilon}_{in}^3$ are the principal inelastic strain rates with $\dot{\varepsilon}_{in}^1 \geq \dot{\varepsilon}_{in}^2 \geq \dot{\varepsilon}_{in}^3$. For an axial and torsional considered load case, $\dot{\varepsilon}_{in}^n$=$\dot{\varepsilon}_{in}$ and $\dot{\varepsilon}_{in}^s$=$[(\dot{\varepsilon}_{in})^2 + 4/9(\dot{\gamma}_{in})^2]_{1/2}$, where $\dot{\varepsilon}_{in}$ and $\dot{\gamma}_{in}$ are the inelastic axial strain rate and inelastic shear strain rate, respectively. $L_c^{\pm}$ is the creep loading function which represents the effects of the multiaxial loading and temperature. It is a function of the ratio of maximum principal stress σ_I and the Von Mises effective stress $\sigma_{eff,M}$ [89]. $L_f^{\pm}$ and $L_c^{\pm}$ are defined as

$$L_f^{\pm} \equiv L_f^{\pm}[\omega, T] = \begin{cases} L_f^{+}[T] & \omega \geq 0 \\ L_f^{-}[T] & \omega < 0 \end{cases} \tag{6.31}$$

and

$$L_c^{\pm} \equiv L_c^{\pm}[\beta, T] = \begin{cases} L_c^{+}[T] & \beta \geq 0 \\ L_c^{-}[T] & \beta < 0, \end{cases} \tag{6.32}$$

where

$$\omega = \frac{\dot{\varepsilon}_{in}^{n}}{\dot{\varepsilon}_{in}^{s}}, \qquad \beta = \frac{\sigma_I}{\sigma_{eff,M}} \tag{6.33}$$

$L_f^{\pm} > 0$ is postulated and the fatigue damage always accumulates, but a negative creep damage rate is allowed through $L_c^{\pm}$, though it is, however, always positive. For instance, L_c^{+}=1 and L_c^{-}=−1 are assumed for the uniaxial case in tension and compression, respectively [90]. MF_f and MF_c are two multiaxiality factors, which are used to model the hydrostatic effects on fatigue and creep damage, respectively. The constants T_f, T_c, $\dot{\varepsilon}_f$, and $\dot{\varepsilon}_c$ in Eqs. 6.24 to 6.27, are introduced for dimensional considerations. They are set equal to 1 in the appropriate units. The other constants, n_f, m_f, σ_f, n_c, m_c, a_k and b_k must be determined from appropriate axial, torsional, and biaxial tests with and without hold time. Methods with a close similarity are described in section 7.1.

7 Lifetime Prediction

7.1 Ideas of Modelling the Lifetime at Cyclic High Temperature Loading

To acquire the complex interaction of pure fatigue, creep and environmental conditions at practical relevant dimensioning of high temperature components, several methods and approaches exist. According to Danzer [91], lifetime prediction methods can be classified into four main groups:

- empiric models
- damage mechanism methods
- physical models
- fracture mechanical methods

7.1.1 Empiric Models

Fundamentally empiric methods to predict lifetime are based on the principle of implementating a damage parameter like strain, strain rate, stress, temperature and so on, which is defined by correlation to experimental results. It is assumed that among a damage parameter, which is variedly defined according to the method, and the time or number of cycles to fracture respectively, there is a definite correlation which can be used for lifetime prediction. At isothermal high temperature experiments, following models are appropriate to describe the lifetime of a component:

Models concerning the the linear and non-linear partial damage accumulation, modifications of the Coffin-Manson-rule [92, 93], the category of "Strain Range Partitioning" (SRP)-methods [94], the "Strain Rate Modified Accumulation of Time Dependent Damage" (SRM-model), or the "Frequency Modified Damage Function" (FMDF-method) [95].

The SRM- and FMDF-method are constructed onto results of basic experiments of creep-fatigue-behaviour and enable the prediction of lifetime due to complex load cases. The SRM-model is a modification of the "Accumulation of Creep Damage" (AC-model) under continously varying stress $\sigma(t)$ and temperature $T(t)$. The number of cycles to fracture ($N_{f,AC}$) according to the AC-model at periodic load is defined by

$$N_{f,AC} = \frac{1}{D_{cr}(\tau)} = \left[\int\limits_0^\tau \frac{1}{t_{cr}(\sigma(t), T(t))} dt \right]^{-1} \tag{7.1}$$

at which τ denotes the duration of one cycle, D_{cr} the creep damage parameter and $t_{cr}(\sigma, T)$ the time to creep induced fracture at the stress σ and temperature T. Towards integration of Eq. 7.1, the simple expression for the number of load cycles at isothermal symmetric loads results in

$$N_{f,AC} = \alpha^* \beta^* \gamma^* \frac{t_{cr(\sigma_t, T)}}{\tau_t} \tag{7.2}$$

in this formulation σ_t is the highest investigable tensile stress in the load cycle and τ_t the time increment of the cycle, in which tensile stresses are effecting. The factor α^* describes the stress dependence of the creep-law, β^* the damaging effect of compression phases and the parameter γ^* specifies the influence of the load character. In the AC-model the average damage produced during one load cycle, is replaced by the same amount of creep damage, which is only possible if the damage mechanisms are quasi identic in the fatigue- and creep experiments. Therefore Danzer [91] introduced a parameter r to predict the material condition due to unsteady loads, which concerns the relation of the mean values of the averaged inelastic deformation rate $\dot{\varepsilon}_{in}$ during the tensile part of one cycle and the steady state creep rate $\dot{\varepsilon}_s$, in each case with the same external stress:

$$r(t) = \frac{\int_0^t \dot{\varepsilon}_{in}(\sigma(t'), T(t'), t') dt'}{\int_0^t \dot{\varepsilon}_s(\sigma(t'), T(t')) dt'} \tag{7.3}$$

The use of the AC method is suggested if the the parameter satisfies the criteria of $r_t < 10$, but this linear accumulation of creep damage includes no fitting parameters, determined by fatigue experiments. To consider the deviations in the material condition at alternating load from those to steady state creep, i.e. at high r_t values, the SRM-method was propagated

$$N_{f,SRM} = \left[\int_0^\tau \frac{1}{t_{cr}(\sigma(t), T(t))} \left(\frac{\dot{\varepsilon}_{in}}{r_0 \dot{\varepsilon}_s} \right)^{\nu_*} dt \right]^{-1} \tag{7.4}$$

with ν_* as a fitting parameter and r_0 equals to r in the creep experiment. Analogical to the approximation in Eq. 7.1, the approximation of Eq. 7.4 results in

$$N_{f,SRM} = \alpha^* \beta^* \gamma^* \frac{t_{cr(\sigma_t, T)}}{\tau_t} \left(\frac{r_t}{r_0} \right)^{-\nu_*} = N_{f,AC} \left(\frac{r_t}{r_0} \right)^{-\nu_*}. \tag{7.5}$$

In general the SRM as well as the AC model are based on creep-data and should be restricted to near creep like material conditions. For a definition of the relation to creep, the r_t parameter is used. From experiences of less ductile, high strength materials (superalloys), the application of the SRM-model for lifetime prediction at isothermal high-temperature fatigue loading has produced satisfying results due to the condition $r_t < 10^6$.

In difference to the SRM model, the FMDF model is based on fatigue data. This method belongs to “semi-empiric” lifetime prediction methods, which acquire creep-fatigue interactions by energetic attempts. The principle of the FMDF method is the association of a direct relation between the hysteresis energy ΔW_T, defined by the area of the hysteresis curve during the tensile period, and the material damage or lifetime. The hysteresis energy can be approximated by a damage function $(\sigma_{max}.\Delta\varepsilon_{pl})$, which is a product of the plastic strain amplitude $\Delta\varepsilon_{pl}$ and the maximum tensile stress σ_{max}. The lifetime can be defined by an exponential relation with the damage function

$$N_f = L(\sigma_{max}.\Delta\varepsilon_{pl})^{-\eta}, \tag{7.6}$$

where L and η depict material parameters. This equation is not very different from the Coffin-Manson-rule, only the extension in the base by the maximum occurring tensile stress σ_{max} in the load cycle is different.

At higher temperatures, time-dependent damage mechanisms occur in addition to the time-independent fatigue damage. Due to this reason, the equation was modified by a frequency term f^{k-1}

$$N_{f,FMDF} = L(\sigma_{max}.\Delta\varepsilon_{pl})^{-\eta} f^{k-1}, \tag{7.7}$$

where f denotes the experimental frequency and k a material parameter. For the reason that positive mean stresses (σ_m) cause creep damage at high temperatures, they can have a strong influence onto the fatigue lifetime. In the FMDF method, the mean stresses are at least partly considered by the maximum stresses $(\sigma_{max} = \sigma_m + \Delta\sigma/2)$. It is also possible to consider the influence of the cyclic profile onto the creep-fatigue lifetime with the help of a frequency separation method, which was propagated for experiments with dwell times. Here an additional creep damage is expected during dwell time combined with tensile load and a heal up of pore damage at the dwell time under the compressive phase of the load cycle. To consider the damaging influence onto high temperature fatigue lifetime by the cyclic profiles in the dwell time expriments, a so called "equivalent" frequency f^* is introduced which replaces the given experimental frequency f to acquire the quantitative damaging and healing effects of dwell times. These equivalent frequency is $f_* = 1/(\tau_{dc} + \tau_{H,t} - \tau_{H,c})$ for $\tau_{H,t} > \tau_{H,c}$ and $f^* = f = 1/\tau_{dc}$ for $\tau_{H,t} \leq \tau_{H,c}$, where τ_{dc} is the duration of a cycle without dwell time and $\tau_{H,t}$ as well as $\tau_{H,c}$ denote the dwell time under tensile as well as compressive load. Empiric models for lifetime prediction of thermo-mechanical fatigue loading were used in many studies, and it was shown that also under TME conditions, lifetime prediction models based on empiric methods can successfully be applied. But the matter is that as a result of their lacking physical interpretability, there is no reliability with the transmittance onto other load cases, because several other load cases are not cosidered due to the evaluation of the model parameters. Particular attention should be given to the verification of their scope of application.

7.1.2 Damage Mechanics

The works developed to characterise tertiary creep [96, 97] were decisive for the constitution of damage mechanics, whereby the formation of pores and cracks was described by continuum mechanical methods [98]. Since that time these ideas were transfused onto several load cases like plastic deformation, high cycle fatigue or low cycle fatigue.

Many new methods are based on the implementation of a damage function ω_D, which indicates the proportion of cracks and pores, situated on the area perpendicular to the external stress direction (see 6.2.1), and thus determining the degree of material damage. In a general view, the damage function characterises the diminution of strength in the sense of an introduced concept of the effective stress $\hat{\sigma}$. So it is assumed that starting from the applied stress σ, the incremental damage enhances the effective mean stress onto the remaining cross section according to $\hat{\sigma}/(1-\omega_D)$ and goes into the constitutive equations of the material:

$$\dot{\varepsilon} = \frac{d\varepsilon}{dt} = f(\sigma, T, \omega_D, ...) \tag{7.8}$$

The dots in this equation stand for further inner variables (such as the internal stress), where applicable. For a reasonable description of the damage behaviour, it is also necessary to exactly know the material damage ω_D at every point in time. Therefore, a kinetic equation considering ω_D is established:

$$\dot{\omega_D} = \frac{d\omega_D}{dt} = g(\sigma, T, \omega_D, ...). \tag{7.9}$$

The determination of Eq. 7.9, which depends on the damage mechanism, is a serious problem of damage mechanics. In principle the equations for the developement of damage are to specify, by conformation of appropriate chosen functions, upon experimetal data. If the kinetic equation of damage is based on a mathematical structure, which can be assimilated by separation of variables, then the description in comparison to the linear damage accumulation is equivalent.

During high-temperature fatigue conditions, damage mechanical methods can describe the non-linear effects of damage accumulation, if the material damage is independent from the nature of development, by one single parameter ω_D. In this case it is possible to separate the damage increment $d\omega_D$

$$d\omega_D = \left(\frac{\partial \omega_D}{\partial N}\right) dN + \left(\frac{\partial \omega_D}{\partial t}\right) dt = f_f(\Delta\sigma, \sigma_m, \omega_D, ...)dN + f_{cr}(\sigma, \omega_D, ...)dt \tag{7.10}$$

into one term $(\partial\omega_D/\partial N)dN$, which depicts the increase of fatigue damage, and into one term $(\partial\omega_D/\partial t)dt$, which describes the increase of creep and time-dependent damage. The kinetic equations for the functions f_f and f_{cr} are evaluated by adaptation of respectively pure fatigue or creep experiments. An overview of application possibilities of continuum mechanical methods for a description of the interaction between creep and fatigue processes can be found in the work of Murakami [99]. An interesting example for the application of this procedure is the “Damage Rate Model” (DRM model) according to Majumdar and Maiya [100]. This model is based on the assumption that high-temperature fatigue is mainly a process of crack propagation and pore growth. Furthermore the crack length a and the pore radius r are considered as characteristic parameters of accumulated damage, and the lifetime is determined by growth and coagulation of initial micro cracks and pores to a macro crack. If the macro crack achieves a critical amount a_f and r_f, the fracture suddenly occurs. In the DRM model independent growth of micro cracks and pores is assumed. The kinetic equations of damage are as follows [100]:

$$\frac{da}{dt} = \begin{cases} T'.a.|\varepsilon_{pl}|^p.|\dot{\varepsilon}_{pl}|^{k_f} & \text{for tensile loads} \\ C'.a.|\varepsilon_{pl}|^p.|\dot{\varepsilon}_{pl}|^{k_f} & \text{for compressive loads} \end{cases} \tag{7.11}$$

and

$$\frac{dr}{dt} = \begin{cases} G.r.|\varepsilon_{pl}|^{p}.|\dot{\varepsilon}_{pl}|^{k_r} & \text{for tensile loads} \\ -G.r.|\varepsilon_{pl}|^{p}.|\dot{\varepsilon}_{pl}|^{k_r} & \text{for compressive loads} \end{cases} \tag{7.12}$$

where T', C', G, p, k_f and k_r are all material parameters. The kinetic equations of damage progression 7.11 and 7.12 represent the micro crack and pore growth rate as a function of plastic deformation and the plastic deformation rate. Equation 7.11 shows that different micro crack growth rates due to tensile or compressive load are required. In the kinetic Eq. 7.12, the healing of pores at compressive loads is established, whereby the pore size should not fall below the initial value.

As a fracture criteria due to creep-fatigue conditions the following equation is denoted [100]:

$$\frac{ln(a/a_0)}{ln(a_f/a_0)} + \frac{ln(r/r_0)}{ln(r_f/r_0)} = 1 \tag{7.13}$$

in which a_0 and r_0 are the initial crack length and pore size, a_f and r_f the critical crack length and pore size. The integration of equations 7.11 and 7.12 takes into account the fracture criteria of Eq. 7.13, and delivers the lifetime estimation according to the DRM model. The number of cycles to fracture $N_{f,DRM}$ results from an isothermal symmetric cyclic load with plastic strain amplitude $\Delta\varepsilon_{pl}/2$ and constant strain rate $\dot{\varepsilon}_{pl}$ according to [100]:

$$N_{f,DRM} = \frac{p+1}{A} . \frac{\dot{\varepsilon}_{pl}^{1-k_f}}{\Delta\varepsilon_{pl}^{1+p}} \tag{7.14}$$

with $A = (T' + C')/[ln(a_f/a_0)]$. As mentioned before, the DRM method requires an independet growth of micro cracks and pores. Isothermal fatigue experiments on several materials resulted in the conclusion that this requirement is not always fulfilled, because creep pores have a very strong influence onto the fatigue crack growth [101, 102]. A modification of the DRM method ("Modified Damage Rate Model" or MDRM model) [103, 104] tries to consider the complex interaction of creep and fatigue processes partly by non-linear damage mechanics, as the fatigue crack growth is not specified independently to the creep pore growth. The kinetic equation for the crack growth rate is converted and defined [103]:

$$\frac{1}{a}\frac{da}{dt} = \begin{cases} T'(1 + \delta lnr/r_0)|\varepsilon_{pl}|^{p}.|\dot{\varepsilon}_{pl}|^{k_f} \\ C'(1 + \delta lnr/r_0)|\varepsilon_{pl}|^{p}.|\dot{\varepsilon}_{pl}|^{k_f} \end{cases} \tag{7.15}$$

where δ is a material parameter. The expression in brackets describes the acceleration of crack growth caused by creep damage. The growth of creep pores in the MDRM method is modelled analogically to the DRM method, if Eq. 7.12 is compared.

The description of the damage process in form of differential equations is advantageous in comparison to common empiric procedures because the damage mechanic is then not limited to one defined load case, but flexible and applicable onto complex load distributions. The coupling of equations for damage and strain rate enables the characterisation of effects, which occur due to variable sequences of the load application, which can have a strong influence onto the kinetics of the damage evolution, without additional modifications of the model. But it is necessary to choose an appropriate equation for the damage rate. The instruction of the analytical design of this equation and the fitting of the included equation parameters onto the experimental data can be a great effort. As Chaboche documented in [105], where examples for damage evolution are given, the first damage is not experimentally detectable until 90% of lifetime or more passed over, which is a reason that the determination of kinetic damage equations is not that easy. But the accuracy of the lifetime prediction depends on the exact knowledge of this equation. That is why damage mechanics have similar problems to solve, concerning the determination of the analytical form of the kinetic equation and the fitting of model parameters, as the empiric methods concerning the determination of damage parameters. A solution of these problems could accommodate a precise physical appreciation of the damage mechanism.

7.1.3 Physical Approach

The precisest results for complex load cases should be obtained by physical models, which means models describing the damage evolution on the basis of movement of atoms, vacancies and dislocations, because these models describe the damage evolution by taking into account physically based functions. Physical methods to describe high-temperature deformation were developed to model the pore growth during creep [54]. Although they have no free fitting parameters, they describe the growth rate of pores in their applicable range quite well. The occurring parameters in these models can be determined metallographically (over distance between pores or grain size) or they are common physical parameters like diffusion coefficient and atomic volume. Physical models for this kind of damage are mentioned in section 5.2. For technical alloys, the damage mechanisms during application conditions are not often known exactly. In general it is not known before, at which load which damage mechanism occurs and which physical model is appropriate to calculate the lifetime. But in some single cases it could be shown that some empiric and damage mechanic models conform to physical models. Thus the meaning of physical models for lifetime prediction at this time is to show the physical background for the empiric and damage mechanic models. This can be useful to determine the load ranges, which can be described by empiric models, and to define the limits of these methods [44].

7.1.4 Fracture Mechanical Methods

In operating components, cracks accumulate like in experimetal specimens, wherby the crack initiation can be attributed to fatigue, corrosion or the coagulation of creep pores. With the assistance of fracture mechanics, such a relevant loading parameter can be determined for the material behaviour, which is characteristical for the stress field in the area of the crack tip. When the knowledge about the stress field around the crack tip is coupled with model assumptions of the damage evolution, the crack growth rate can be calculated [44].

Fracture mechanical methods describe the crack growth from the initial size until a critical, material depending parameter. These methods are commonly applicated, if there are viable cracks or defects which act as crack seeds in the virginal material, or if cracks develop within a short time or few cycles. At high-temperature fatigue, it is tried to make a difference between a cyclic dependent and a time dependent rate of crack growth. Depending on the loading conditions (temperature, frequency, etc.), the cyclic dependent or time dependent rate dominates [47].

In most cases, the methods based onto the linear summation of cyclic and time dependent crack growth rates could be applied successfully for a lifetime prediction of high-temperature fatigue conditions [106, 107]. It should also be mentioned that the application of the linear summation leads to a significant undervaluation of the experimental lifetime, which is attributed to a strong creep-fatigue interaction [47].

Riedel [49] determined the relevant loading parameters for several material categories and mentioned the particular stress field in the crack tip zone. Depending on the material behaviour the stress around the crack tip can be characterized by different loading parameters. At unsteady loading (fatigue), the cracks propagate due to periodic expanding and compression of the crack tip which was described by Laird and Smith in 1962 [108]. Such developed cracks are known as fatigue cracks, the crack propagation per load cycle is, according to the model of Laird and Smith, in the dimension of the crack openening at the tip. By this procedure, the formation of microscopic investigable striations at the fracture surface can be explained [44].

8 Special Simulation Methods

8.1 Finite Element Methods

8.1.1 The Elastic-Viscoplastic Chaboche Model

Introduction

Cyclic viscoplastic constitutive equations are increasingly used for the inelastic analysis of structures under severe thermomechanical conditions. In the following the classical models are modified in order to follow the general principles of thermodynamics with internal variables. By using the restrictive framework of standard generalised materials, state variables associated to various kinds of kinematic and isotropic hardening are selected. The evolution equations for these internal variables are then formulated in a slightly less restrictive form. For each hardening process, the separation of the total plastic work into energy, dissipated as heat and energy stored in the material, is discussed.

Plastic and viscoplastic constitutive equations have been greatly developed over the last decades, especially for application under cyclic loadings and high temperatures. Though some of them do not consider directly the notion of back stresses, the cyclic constitutive equations are generally based on linear and nonliear kinematic hardening. Among these, a model developed at Onera is based on a work in which the so called nonlinear kinematic hardening rule (NLK) was introduced. It uses the superposition of several isotropic and kinematic hardening variables, each of the corresponding evolution equations being in a hardening/dynamic-recovery/thermal-recovery format [38].

On the other hand, thermodynamics with internal variables offers a good framework to introduce constitutive equations. It offers both a guideline and some constraints for the choice of thermodynamically consistent evolution equations. A special form uses the notion of standard generalised materials, where the complete thermoelastic-inelastic behaviour is defined from the knowledge of two potentials: the thermodynamic potential to describe the present state, and the dissipative potential for the irreversible evolutions.The constitutive equations developed in this model are thermodynamically consistent. It can be shown, either in the framework of standard generalised materials, or without explicitly using a dissipative potential.

Introducing mechanical constitutive models into a thermodynamic framework allows the partition of the plastic work into the energy stored by the material and the one dissipated as heat. It well known from previous works, that the stored energy is only a small part of the total plastic work (between 5% and 50%) depending on the material and on the strain level.

The intention is now to introduce the constitutive equations into the thermodynamic framework, to discuss the various possibilities for the equations governing the different hardening variables, and to show the corresponding partitioning of the total plastic work between stored energy and energy disspated as heat.

The Constitutive Equations

In a Cartesian reference configuration, the strain $\boldsymbol{\varepsilon}_{ij}$ is taken to be composed of elastic $\boldsymbol{\varepsilon}^e_{ij}$ (reversible, includes thermal strain) and inelastic or plastic $\boldsymbol{\varepsilon}^p_{ij}$ (irreversible) parts such that

$$\boldsymbol{\varepsilon}_{ij} = \boldsymbol{\varepsilon}^e_{ij} + \boldsymbol{\varepsilon}^p_{ij}, \tag{8.1}$$

and there is no inelastic strain in the stress-free virgin state. If the reversible elastic part and thermal strain is considered separately, the equation looks like as follows:

$$\boldsymbol{\varepsilon} = \boldsymbol{\varepsilon}_e(\sigma) + \boldsymbol{\varepsilon}_{th}(T) + \boldsymbol{\varepsilon}_{in}, \qquad \boldsymbol{\varepsilon}_{th}(T) = \varepsilon_{th}(T)\mathbf{1} \tag{8.2}$$

where $\mathbf{1}$ denotes the unit tensor. The viscoplastic potential and the hardening variables are developed in the framework of unified viscoplasticity, considering only one inelastic strain. The existence of a viscoplastic potential in the stress space is assumed. Its position, shape, and size is depend on the various hardening variables. It is limited to the case where the potential is a given function of the viscous stress or overstress [38].

The Hookean law is now given by

$$\boldsymbol{\sigma} = 2G\boldsymbol{\varepsilon}^{'}_e + \frac{E}{3(1-2\nu)} tr\boldsymbol{\varepsilon}_e\mathbf{1} \tag{8.3}$$

with G denotes the shear modulus, E the Young's modulus, ν the Poisson's ratio and the deviator of the elastic strain tensor $\boldsymbol{\varepsilon}^{'}_e$.

For the lifetime prediction of highly stressed extrusion tools during service, taking into account the inelastic strain rate during a cycle, it is necessary to be able to assess the inelastic stress-strain response of the material. The influence of the thermo-mechanical history on the current stress-strain behaviour can be described with internal (non-measurable) variables, beside the measurable (external) variables of deformation, time, temperature and stress. The evolution equations for the internal variables are given by flow and hardening rules. In viscoplastic, i.e. unified inelastic, models, creep and plasticity are covered within a single inelastic strain variable in order to describe creep-plasticity interaction. The flow rule, i.e. the evolution equation for the inelastic strain is according to Chaboche [38]

$$\dot{\boldsymbol{\varepsilon}}_{in} = \frac{3}{2}\left\langle \frac{J_2(\mathbf{S}-\mathbf{X}) - (k+R_h)}{K} \right\rangle^n \frac{\mathbf{S}-\mathbf{X}}{J_2(\mathbf{S}-\mathbf{X})} \quad , \quad \langle y \rangle := \begin{cases} y & \text{, if y >0} \\ 0 & \text{, otherwise} \end{cases} \tag{8.4}$$

with the applied stress deviator $\mathbf{S}$ and specifying k as the initial elastic limit, R_h as the increase of the elastic limit due to hardening, X as the internal back stress tensor, describing kinematic hardening and K as a material parameter. Olschewski et al. [109] have proposed a certain type of a thermo-mechanical evolution equation for the isotropic hardening variable $R = Q(T)r$ in order to describe non-isothermal material behaviour, T denotes the temperature:

$$\dot{R}_h = Q\dot{r} + \frac{R_h}{Q}\frac{dQ}{dT}\dot{T} \tag{8.5}$$

with Q as the saturation parameter of R at isothermal loading and r as the related isotropic hardening variable with the evolution equation

$$\dot{r} = b\left(1 - \frac{R_h}{Q}\right)\dot{p} - \frac{f}{Q}\left(\frac{R_h}{Q}\right)^{S} \quad , \quad r(t=0) = 0 \quad , \quad \dot{p} := \sqrt{\frac{2}{3}}\|\dot{\varepsilon}_{in}\| \tag{8.6}$$

where b, f, s are material parameters adapting the isotropic hardening and static recovery, respectively, and $\dot{p}$ is the inelastic Mises equivalent strain-rate.

The rate equations for the kinematic hardening variables obey a unique format, where the back stress $\mathbf{X}_{bs}$ is decomposed into independent variables $\mathbf{X}_i$, each of them being of the same rule. As shown in previous studies, two or three of such variables are suffiecient to describe, very correctly, the real materials [40, 41]. For a consideration of two independent variables, the applied formulas are as follows

$$\mathbf{X}_{bs} = \mathbf{X}_1 + \mathbf{X}_2 \quad , \quad \mathbf{X}_i = \frac{2}{3}a_i(T)\boldsymbol{\alpha}_i \quad , \quad i = 1,2 \tag{8.7}$$

where a_i(T) are saturation parameters of the internal back-stresses $\mathbf{X}_i$, and $\boldsymbol{\alpha}_i$ are related kinematic hardening variables:

$$\dot{\boldsymbol{\alpha}}_i = c_i\dot{\boldsymbol{\varepsilon}}_{in} - \frac{3}{2}c_i\frac{\mathbf{X}_i}{a_i}\dot{p} - \frac{3}{2}\frac{d_i}{a_i}\left(\frac{J_2(\mathbf{X}_i)}{a_i}\right)^{m_i}\frac{\mathbf{X}_i}{J_2(\mathbf{X}_i)} \quad , \quad \boldsymbol{\alpha}_i(t=0) = 0 \tag{8.8}$$

with c_i, d_i, and m_i as material parameters defining the kinematic hardening and the static recovering, respectively.

The related hardening variables r and $\boldsymbol{\alpha}_i$ are describing the degree of hardening, that corresponds in the material structure to the accumulation of immobile dislocations and that causes certain internal stresses $k + R_h$ and $\mathbf{X}_i$, respectively, at a certain temperature. For example, the isotropic variable r tends, at negligible static recovery, according to Eq. 8.6 for any temperature to its saturation value 1. Something similar is the case for the kinematic variables α_i according to Eq. 8.8 at proportional loading. Thus, the internal stresses $k + R_h$ and $\mathbf{X}_i$ vary at temperature changes according to Eqs. 8.5 and 8.7 at most to their saturation levels (Q and 2/3 a_i) at the current temperature [40].

8.2 Crystal Plasticity FEM

An adequate knowledge of the mechanical properties of metals is technically very important and therfore appropriate evaluation methods play a basic role in physical metallurgy. The main focus is to describe plastic material behaviour with the aim of crystallite deformation. On the experimental side, tensile and compressive tests as well as creep experiments and hardness tests are appropriate to get values, describing the mechanical behaviour of the material [110]. A polycrystal is understood as just an assembly of coupled single crystals with different crystallographic orientations, and the formulations of crystal plasticity are applied to describe the behaviour of such single grains. The evolution of a material model is based on two different strategies, which is based on phenomenological aspects on the one hand and on the other hand based on physical approaches with both, advantages and disadvantages.

8.2.1 Evolution of Dislocations

The interaction of multiplying dislocations influences the hardening rate of crystals. According to the fact, that dislocations are generated at the beginning of plastic deformation and annihilated with progressive deformation, Kocks [111] proposed an approach for the quantitative evolution of the whole dislocation density ρ in macroscopic models to describe the isotropic hardening:

$$\dot{\rho} = \frac{1}{bL}\dot{\varepsilon} - k_0\rho\dot{\varepsilon}, \tag{8.9}$$

where k_0 is supposed to be a constant according to Kocks [111], which depends on the strain rate $\dot{\varepsilon}$ according to Estrin [112]. The mean free dislocation path length L is inverse proportional to the square root of the whole dislocation density [113]:

$$L \sim \frac{1}{\sqrt{\rho}}. \tag{8.10}$$

In the microscopic scale, Essmann and Mughrabi [114] make a difference in the evolution of dislocation densities on edge and screw dislocations with different free path lengths and critical annihilation distances. Accordingly two evolution equations are derived, which both have a similar construction to Eq. 8.9. Furthermore, the formation of dislocations on single glide systems with different gliding is investigated, whereby a quantitative evolution of dislocations results in

$$\dot{\rho}^{\alpha} = \frac{1}{bL_{\alpha}}\dot{\gamma}^{\alpha} - 2\frac{y_c}{b}\rho^{\alpha}\dot{\gamma}^{\alpha}, \tag{8.11}$$

where ρ^{α} denotes the dislocation density on the glide sytem α, $\dot{\rho}^{\alpha}$ the dislocation density evolution on α, b is the value of the Burgers vector and y_c the critical annihilation distance where dislocation annihilation occurs.

The dislocation formation and annihilation depend on glide characteristics. Teodosiu [115] formulated the evolution of dislocation densities independently from the glide directions and described the isotropic hardening of crystals based on Eq. 8.11:

$$\dot{\rho}^{\alpha} = \frac{1}{bL_{\alpha}}|\dot{\gamma}^{\alpha}| - 2\frac{y_c}{b}\rho^{\alpha}|\dot{\gamma}^{\alpha}|, \tag{8.12}$$

The free dislocation distance L_{α} of a system is inverse proportional to the square root of ρ, as mentioned before, but the free distance L_{α} covered by new formed dislocations on a system until immobilising, is according to Essmann and Mughrabi [114] an algebraic function, which is constant at single glide conditions and monotonously decreasing at beginning multi glide, but this dependence on gliding is more of phenomenological nature. Teodosiu [115] considers a short range interaction of dislocations and proposes the following relation of the mean free distances on a system, which depend on the distance between barriers during gliding:

$$L_\alpha = K \left(\sum_{b \neq a} \rho_b \right)^{-1/2} , \tag{8.13}$$

where K depicts a model parameter. In this approach, the mean free distance is determined by the dislocation densities of the other gliding systems. In principal, dislocations on the same gliding plane do not inhibit each other, so the immobilising of dislocations happens due to wood dislocations. As a consequence, the summation is just over the particular wood systems, which can be expressed by the index b_s:

$$L_\alpha = K \left(\sum_{b_s} \rho_{b_s} \right)^{-1/2} . \tag{8.14}$$

This equation can be described with the aim of a vertical matrix $\vec{Z}_\alpha$ and by the matrix $\mathbf{Z}$ consisting the components 0 and 1

$$\begin{aligned} \mathbf{Z} \quad &= \quad \begin{pmatrix} 0 & 0 & 0 & 1 & 1 & 1 & 1 & 1 & 1 & 1 & 1 & 1 \\ 0 & 0 & 0 & 1 & 1 & 1 & 1 & 1 & 1 & 1 & 1 & 1 \\ 0 & 0 & 0 & 1 & 1 & 1 & 1 & 1 & 1 & 1 & 1 & 1 \\ 1 & 1 & 1 & 0 & 0 & 0 & 1 & 1 & 1 & 1 & 1 & 1 \\ 1 & 1 & 1 & 0 & 0 & 0 & 1 & 1 & 1 & 1 & 1 & 1 \\ 1 & 1 & 1 & 0 & 0 & 0 & 1 & 1 & 1 & 1 & 1 & 1 \\ 1 & 1 & 1 & 1 & 1 & 1 & 0 & 0 & 0 & 1 & 1 & 1 \\ 1 & 1 & 1 & 1 & 1 & 1 & 0 & 0 & 0 & 1 & 1 & 1 \\ 1 & 1 & 1 & 1 & 1 & 1 & 0 & 0 & 0 & 1 & 1 & 1 \\ 1 & 1 & 1 & 1 & 1 & 1 & 1 & 1 & 1 & 0 & 0 & 0 \\ 1 & 1 & 1 & 1 & 1 & 1 & 1 & 1 & 1 & 0 & 0 & 0 \\ 1 & 1 & 1 & 1 & 1 & 1 & 1 & 1 & 1 & 0 & 0 & 0 \end{pmatrix} \\ &=: \quad \left(\vec{Z}_1, \vec{Z}_1, \vec{Z}_1, \vec{Z}_2, \vec{Z}_3, \vec{Z}_4, \vec{Z}_5, \vec{Z}_6, \vec{Z}_7, \vec{Z}_8, \vec{Z}_9, \vec{Z}_{10}, \vec{Z}_{11}, \vec{Z}_{12} \right) . \end{aligned} \tag{8.15}$$

Eq. 8.14 can be represented clearer now [116]:

$$L_\alpha = K \left(\vec{Z}_\alpha^T \vec{\rho} \right)^{-1/2} . \tag{8.16}$$

The vector $\vec{\rho}$ includes 12 componets of dislocation densities at 12 glide systems, and $\vec{Z}_{\alpha}^{T}$ is the transposed matrix vector of $\vec{Z}_{\alpha}$. Such a description can be very useful for a numerical transformation.

8.2.2 Constitutive Law based on Dislocation Density for BCC Materials

The calculated Peierls stress for FCC crystals is much smaller than the measured critical resolved stress as there exist close packed lattice planes and close packed lattice directions. Therefore, it can be assumed, that the resistance for moving dislocations is determined by the passing stress and the cutting stress due the other dislocations in the crystal only. BCC single crystals, in contrast, have only densely-packed lattice directions but no densely-packed lattice planes. 24-48 slip systems are reported to be activated to accommodate the external plastic deformation in bcc materials. For this structure, the Peierls stress is so large that one can assume that in order to move the mobile dislocations, the external load has to overcome the resistance both, of the parallel dislocations and the Peierls energy barrier, i.e. forest cuttings can be ignored. In the following, the introduced model is adopted to the BCC crystal structure.

The deformation gradient $\mathbf{F}$ is multiplicative decomposited to separate the elastic and plastic portions of the deformation for a kinematic description of plastic deformation of crystalline materials. The elastic part $\mathbf{F}^{e}$ comprises the stretch and rotation of the lattice, and the plastic part $\mathbf{F}^{p}$ corresponds to the unrecoverable deformation caused by dislocation slip. For the reason that the plastic deformation gradient does not change the lattice orientation, it is possible to use a constant stiffness tensor $\mathbf{C}$ for the stress calculation. The elastic law is defined in the unloaded configuration. BCC crystals have densely-packed lattice directions $\langle 111 \rangle$ but no densely-packed lattice planes. The most densely-packed planes are the $\{110\}$, $\{112\}$ and $\{123\}$ lattice planes. There are at most 48 slip systems if the so-called pencil glide is not considered. As shown in Fig. 8.1, the mobile dislocation experiences the slip resistance from forest and parallel dislocations, and also from the Peierls energy barrier. The parallel dislocation density is defined ρ_{P}^{α} and the forest dislocation density ρ_{F}^{α} [117].

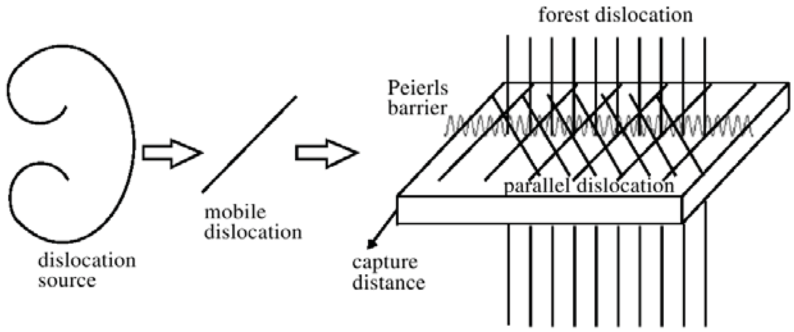

Figure 8.1: Schematic drawing of the slip mechanism for the BCC crystal structure: a mobile dislocation is generated by a Frank-Read source. The external stress must help it to overcome resistances of forest and parallel dislocations, as well as the Peierls energy barrier [117].

While in the FCC case the Peierls potential is so small that it can be neglected, it is much higher for the BCC crystal structure. In fact it is so high, that in BCC structures the forest cutting process can be neglected when formulating the dislocation velocity equation. The plastic velocity gradient $\mathbf{L}^p$ can be calculated by using a standard crystal plasticity finite element (CP-FEM) framework (see e.g. [118])

$$\mathbf{L}^p = \sum_{\alpha=1}^{48} \dot{\gamma}^\alpha \tilde{d}^\alpha \otimes \tilde{n}^\alpha \tag{8.17}$$

where $\dot{\gamma}^\alpha$ is the slip rate on the slip system α, $\tilde{d}^\alpha$ expresses the slip direction, and $\tilde{n}^\alpha$ the slip plane normal with respect to the undistorted configuration. In contrast to [118], a dislocation density based constitutive law is used, so that the slip rates can be calculated by use of the Orowan equation

$$\dot{\gamma}^\alpha = \rho_M^\alpha b v^\alpha \tag{8.18}$$

where v^α is the average velocity of the mobile dislocations ρ_M^α and b the magnitude of the respective Burgers vector. From previous investigations it is known that by applying the principle of maximum plastic dissipation, for the external resolved shear stress during the plastic deformation

$$\frac{\partial \dot{\gamma}^\alpha}{\partial \rho_M^\alpha} = 0 \tag{8.19}$$

a scaling relation can be derived for the mobile dislocation density ρ_M^α in the gliding system α, which amounts to

$$\rho_M^\alpha \approx \frac{2k_B T}{c_1 c_3 G b^4} \sqrt{\rho_P^\alpha} \tag{8.20}$$

where c_1, c_3 are constants, G denotes the shear modulus, b the magnitude of the Burgers vector, T the absolute temperature and k_B the Boltzmann constant. If Eq. 8.20 is compared with FCC materials, the difference can easyly be recognised. Following an approach used in [117], two different flow rules for bulk and for grain boundary elements are distinguished.

- The flow rule for the bulk element

Integrating Eq. 8.20 into Eq. 8.18, the flow rule is derived based on the dislocation slip mechanism. A reference shear rate is included, which is formulated as a function of the dislocation density and temperature. The new flow rule amounts to

$$\dot{\gamma}^{\alpha} = \dot{\gamma}_0^{\alpha} \quad exp\left[-\frac{Q_{Pei}}{k_B T}\left(1-\frac{\tau^{\alpha}-\tau^{\alpha}_{pass}}{\tau^{\alpha}_{Pei}}\right)\right] sign(\tau^{\alpha}), \qquad if \qquad |\tau^{\alpha}| > \tau^{\alpha}_{pass} \tag{8.21}$$

and $\dot{\gamma}^{\alpha} = 0$, if $|\tau^{\alpha}| \leqslant \tau^{\alpha}_{pass}$. $\dot{\gamma}_0^{\alpha}$ is the upper limit of the shear rate, for the case that the Boltzmann factor is equal to 1 in Eq. 8.21

$$\dot{\gamma}_0^{\alpha} = \frac{k_B T \nu_0}{c_1 c_3 G b^2}\sqrt{\rho_P^{\alpha}} \tag{8.22}$$

where ν_0 is the attack frequency and τ^{α}_{pass} the passing stress, caused by parallel dislocations

$$\tau^{\alpha}_{pass} = c_1 G b \sqrt{\rho_P^{\alpha}} \tag{8.23}$$

In the Peierls stress, τ^{α}_{Pei},

$$\tau^{\alpha}_{Pei} = \frac{Q_{Pei}}{c_3 b^3} \tag{8.24}$$

Q_{Pei} denotes the effective energy for the Peierls mechanism [117].

- The flow rule for the grain boundary element

Generally, in crystal plasticity FEM implementations the grain boundaries coincide with element boundaries, but now a special grain boundary element, where one half of the Gauss points belong to one crystal, while the others belong to the abutting crystal [117]. For the constitutive law of material points belonging to this element class, a modified flow rule, where an effective activation energy for the slip process is introduced, which is based on a conservation law for the Burgers vector during the slip penetration through a grain boundary. Based on Eq. 8.21 for the BCC crystal structure, τ^{α}_{Pei} and Q_{Pei} are modified as follows:

$$Q^{'}_{Pei} = Q_{Pei} + c_9 E^{\alpha}_{GB} \tag{8.25}$$

and

$$\tau_{Pei}^{\alpha'} = \frac{Q'_{Pei}}{c_3 b^3}, \tag{8.26}$$

where c_9 is a fit parameter, and E_{GB}^{α} is the activation energy for the penetration of a grain boundary by a mobile dislocation with the length b [117].

There are four processes contributing to the evolution of the statistically stored dislocation:

1. The lock formation mechanism between mobile dislocations and forest dislocations and
2. the dipole mechanism between mobile dislocations with anti-parallel Burgers vector determine the multiplication terms, while
3. the athermal annihilation of two parallel dislocations with anti-parallel Burgers vector within a critical distance and
4. the thermal annihilation determine the annihilation terms.

The complete rate equation system for the immobile SSD combines these four processes. For the details of these rate equations, it is referred to Ma and Roters [119]. The only modification in the present model is, that the thermal annihilation by cross slip of screw dislocations is assumed instead of climb of edge dislocations, so that the bulk diffusion activation energy Q_{bulk} has been replaced by Q_{cross}. When orientation gradients are present in a volume portion, GNDs must be introduced to preserve the continuity of the lattice. In the upon described method the same equations are used for the evolution of this kind of dislocation as given in [119].

8.3 Representative Volume Element Method

A homogenisation procedure to derive the kinematics of a macro continuum with a point wise attached micro structure is shown in Fig. 8.2. The micro polycrystal structure region of the representative volume element (RVE) is made up of an aggregate of well defined crystal grains and it is very small compared with the dimension of the overall macro continuum region $\Omega_C^{\lambda_{sc}}$, defined by a scale factor $\lambda_{sc} \ll 1$, which represents the reciprocal order of the repetition. If the macro continuum body is subjected to a load and contact forces at the boundaries, the resulting deformation and stress vary from point to point and produce the heterogeneity in the micro polycrystal structure of the RVE [120].

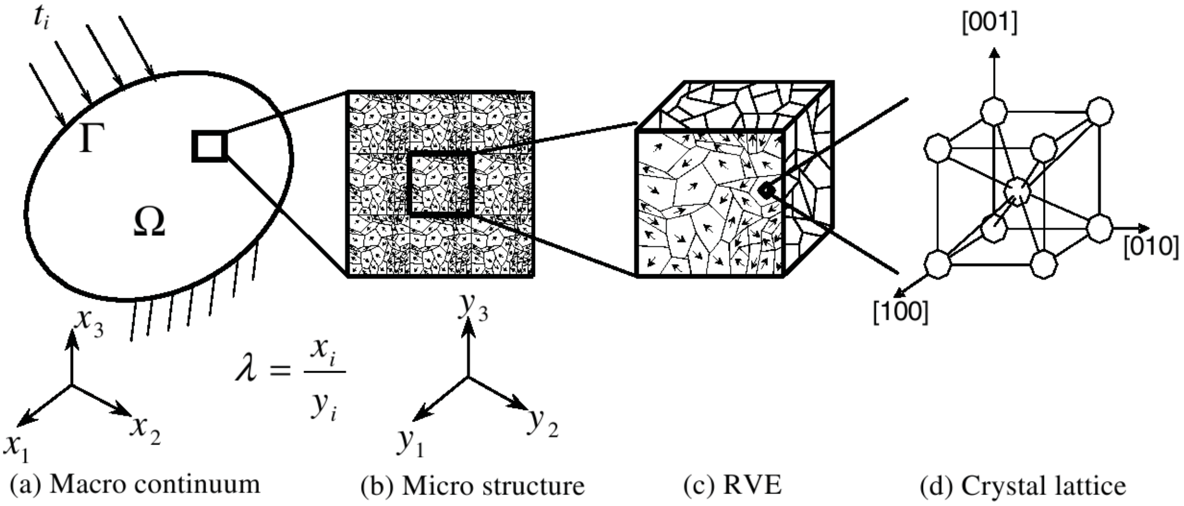

Figure 8.2: Macro continuum and micro polycrystal structures, and coordinates x_i and y_i [120].

In order to describe the effects of heterogeneity in the microstructure, λ_{sc} can be attached as the superscript to all the variables in the formulation if it is essential. Both, a microscopic (y_i) and macroscopic (x_i) coordinate system is introduced so that physical quantities are represented by two different length scales: $\mathbf{x}$ in the macroscopic region $\Omega_C^{\lambda_{sc}}$ and $\mathbf{y}$ (=$\mathbf{x}/\lambda_{sc}$) in the microscopic region. The homogenisation method is employed with the ambition to reflect the heterogeneous microscopic behaviour on the macroscopic deformation [120]. This approach can be be considered for the main mechanisms of ductile damage, such as nucleation, growth and coalescence of microcavities by large plastic deformations. Therefore a relation between the isotropic damage variable ω_D at the mesoscale and the density of microvoids is derived as follows: A RVE at the mesoscale, considered as a cube with the side length l containing n cavity cells of the dimension d^3 (Fig. 8.3).

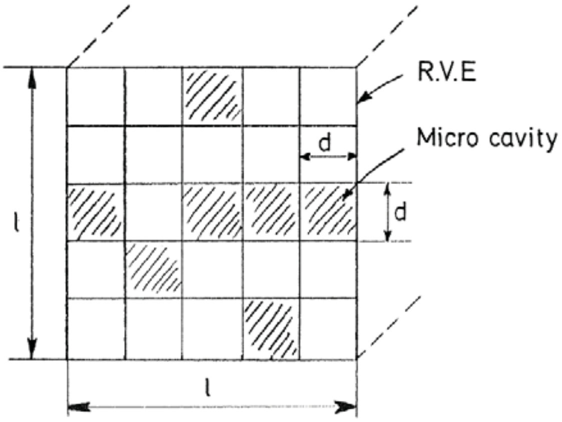

Figure 8.3: Micro-meso element for ductile damage [80].

According to this very simple geometry, the balance of energy calculated from the growth of cavities and from the damage concept can be established. After a certain calculation path, ω_D is obtained as

$$\omega_D = n\frac{d^2}{l^2} \tag{8.27}$$

which is logically if Fig. 8.3 is regarded. Based on Eq. 8.27 the kinetic law of damage evolution can be derived

$$\dot{\omega}_D = \frac{d^2}{l^2}\dot{n} + 2n\frac{d\dot{d}}{l^2}, \tag{8.28}$$

where the first term accounts for the increase in the number of cavities ($\dot{n}$ signifies the number of cavities per unit time), and the second term accounts for the cavity growth.

It is also possible to use this method considering other problems, for example to describe the properties of multi phase materials or compounds. In hot-work tool steels, a relation of two phases, namely the carbides and the softer matrix can be considered.

8.4 Microplane Model

For a wide class of materials, the assumption of isotropic material response yields sufficiently accurate results. Nevertheless, for heterogeneous materials, e.g. concrete or other composites, the assumption of isotrpy is no longer valid, since microcracks and microvoids will develop anisotropically under increased loadding. Moreover, metallic materials may show a an anisotropic response due to their crystalline microstructure.

The modeling of inelasstic isotropic material behaviour is nowadays well-understood, especially because only a few material parameters are needed to simulate either damage or plasticity (Lemaitre and Chaboche [98]). The costitutive modeling of anisotropy, however, is far more difficult and the understanding and identification of material parameters is a sophisticated task (Carol et al. [121]). A general concept to model anisotropic material behaviour has been proposed by Taylor [122], who suggested to consider the uniaxial material response on several characteristc material planes. A clear advantage of this concept is that the material properties can be directly related to the behaviour under uniaxial loading. At first, Taylors ideas were only related to crystal plasticity, where plastic sliding was assumed to take place on several slip planes, defined by the geometry of the crystalline lattice. It was only during the last decade that the general idea of Taylor was applied to continuum damage mechanics by Bažant and Prat [123] and Carol et al. [124, 125]. The generic name “microplane theory” was agreed in order to demonstrate that the concept of defining constitutive laws on characteristic material planes was not restricted to plasticity but could be applied to any kind of material behaviour. The main idea behind microplane models consists in developing the constitutive laws for the two- or three-dimensional continuum starting from the behaviour of a plane of generic orientation, which is then integrated over all possible directions in space. The main difference between the microplane model and the previous similar models is the kinematic constraint assumed, and the principle virtual work (PVW) applied to obtain the corresponding integral micro-macro relation for stresses [121, 126].

Microplane Model under Application

The microplane model is numerically extremly demanding - computation of the stress tensor in a single integration point involves the strain projection to microplanes, an evaluation of local microplane constitutive laws (which may lead to iteration) on each microplane and the homogenisation procedure for computing the overall stress tensor. Moreover, the tangent stiffness matrix can be hardly obtained. For some microplane formulations, there is no direct formula and the only possibility is to construct stiffness from its definition. But this is a very expensive procedure. Due to the lack of tangent stiffness one can use the initial elastic matrix for the whole analysis, but this will lead to a very poor convergence. Therefore, the use of implicit methods, which require the stiffness matrix, is cumbersome, due to an extremely slow iteration process.

An efficient computational scheme employs an explicit algorithm. If the damping is expressed in a special form (for example one may use Rayleigh damping), one does not need the stiffness matrix. Typically, the non-equibrilated internal forces are applied as loading in the next time step. The use of the diagonal mass matrix leads to a very efficient computational scheme, which can be parallelised in a straightforward way. The node-cut and the element-cut techniques can be used to formulate efficient parallel algorithms.

The classical approach to the constitutive modeling is based on a direct relationship between strain and stress tensors ε_{ij} and σ_{ij} and their invariants. In contrary to it, constitutive relations of the microplane model are formulated in terms of strain- and stress components on planes of arbitrary spatial orientations, so called microplanes. This approach excels in conceptual simplicity and allows straightforward modeling of anisotropy and other processes conected with planes with different orientations. The penalty to be paid is a great increase of computational effort. Althoug the microplane theory was originally proposed for plastic behaviour of metals, it can be generally used for any type of material including concrete. The relationship between micro- and macro level is obtained by projecting the strain tensor to the particular microplanes (so-called kinematic constraint) or by projecting stress tensor (static constraint). Then constitutive relations between microstrains and corresponding microstresses are evaluated [126].

The missing link (between microstresses and macrostress for kinematic constraint, and between micro- and macro strain for static constraint, respectively) is obtained by application of the principle virtual work. Such kind of a material model is capable to describe a triaxial nonlinear material behaviour including tensional and compressive softening, damage of the material, different types of loading, unloading or cyclic loading.

The key point of the microplane model is to characterise the material behaviour on a set of microplanes in each material point. The orientation of each microplane can be described by its unit normal n_i. An infinite number of these microplanes can be imaginated, i.e. an infinite set of normals in each material point. The present model [126] is based on so-called kinematic constraint, in which the strain vector on the microplane ε_i^μ is given as a projection of the macroscopic strain tensor ε_{ij}. A microplane strain vector can be obtained by this projection as

$$\varepsilon_i^\mu = \varepsilon_{ij} n_j, \tag{8.29}$$

which can be decomposed into the corresponding normal and shear parts. The normal strain on the microplane can be obtained as follows:

$$\varepsilon_N = n_i \varepsilon_i^{\mu} = n_i \varepsilon_{ij} n_j = N_{ij} \varepsilon_{ij}, \tag{8.30}$$

where N_{ij} is a symmetric tensor defined as $N_{ij} = n_i n_j$. The normal strain ε_N can be further decomposed into volumetric ε_V and deviatoric ε_D parts. Assuming small strains, volumetric and deviatoric parts are defined as

$$\varepsilon_V = \frac{\varepsilon_{kk}}{3}, \tag{8.31}$$

$$\varepsilon_D = \varepsilon_N - \varepsilon_V. \tag{8.32}$$

Components of the shear strain vector are then composed as

$$\varepsilon_{Ti} = \varepsilon_i^{\mu} - \varepsilon_{Ni} = n_k \varepsilon_{ik} - n_i n_j n_k \varepsilon_{jk} = (\delta_{ij} - n_i n_j) n_k \varepsilon_{jk}. \tag{8.33}$$

It is very convenient to express ε_{Ti} in the local microplane coordinate system. Therefore we define two vectors on the microplane. These two vectors are characterised by their unit vectors m and l, respectively. It must be ensured that $l = m \times n$. Magnitudes of shear strains on microplane are then given by

$$\varepsilon_M = m_i(\varepsilon_{ij} n_j) = M_{ij} \varepsilon_{ij}, \tag{8.34}$$

$$\varepsilon_L = l_i(\varepsilon_{ij} n_j) = L_{ij} \varepsilon_{ij}, \tag{8.35}$$

where the two symmetric tensors M_{ij} and L_{ij} are defined as

$$M_{ij} = \frac{m_i n_j + m_j n_i}{2}, \tag{8.36}$$

$$L_{ij} = \frac{l_i n_j + l_j n_i}{2}. \tag{8.37}$$

The definition of the microplane and corresponding microstrain components can be seen in 8.4.

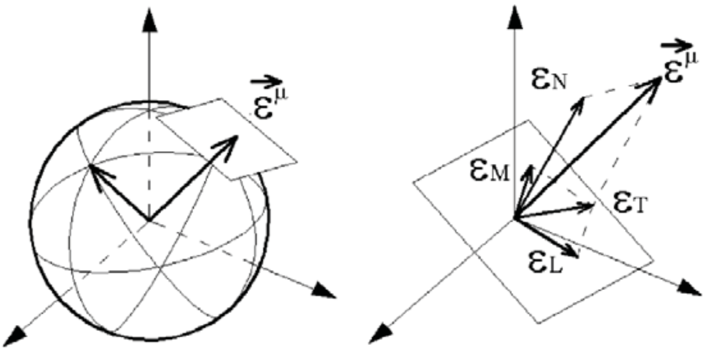

Figure 8.4: Definition of microplanes and microstrain components [126].

Since kinematic constraint (projection of ε_{ij}) was adopted, microplane stress components cannot be, in genral, equal to the projection of the macrostress tensor σ_{ij}. Static equivalence between microstress and macrostress is ensured by means of the principal of virtual work. For a better understanding, the exemplification of microstrain and - stress components are demonstrated beneath (Fig. 8.5):

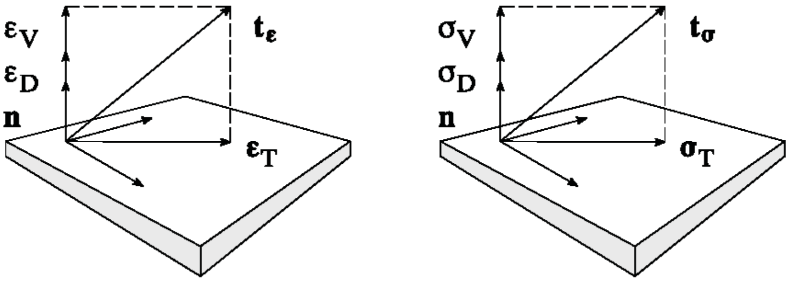

Figure 8.5: Strain and stress components on one microplane [126].

The virtual work of the macroscopic stress tensor working on virtual macrostrains within the unit sphere Ω of volume $(4/3\pi)$

$$W^{macro} = \int_{\Omega} \sigma_{ij}\delta\varepsilon_{ij}d\Omega = \frac{4\pi}{3}\sigma_{ij}\delta\varepsilon_{ij} \tag{8.38}$$

must be equal to the work of all microstress components working on virtual microstrains (normal and shear) integrated over the surface of the unit sphere, i.e. over all microplanes. Taking into account the symmetry of projection tensors it is possible to calculate only with the unit hemisphere Γ:

$$W^{micro} = \int_{\Gamma} (\sigma_N\delta\varepsilon_N + \sigma_M\delta\varepsilon_M + \sigma_L\delta\varepsilon_L)d\Gamma. \tag{8.39}$$

The equality of Eqs. 8.38 and 8.39 and introducing projection tensors for microstrains yields the macroscopic stress tensor as

$$\sigma_{ij} = \frac{3}{2\pi}\int_{\Gamma} (\sigma_N N_{ij} + \sigma_M M_{ij} + \sigma_L L_{ij})d\Gamma. \tag{8.40}$$

It is also convenient to a work-conjugate formulation for volumetric stress analogically to the formulation of the macrostress tensor σ_{ij}. A relation for the volumetric stress is then given by the equality of the virtual work of volumetric stress on the macro and on the microlevel as

$$\frac{2\pi}{3}\frac{\sigma_{kk}}{3}\delta\varepsilon_{mm} = \int_{\Gamma} \sigma_V\delta\varepsilon_V d\Gamma. \tag{8.41}$$

By introducing this formula into Eq. 8.40 the macroscopic stress tensor is obtained by

$$\sigma_{ij} = \sigma_V\delta_{ij} + \frac{3}{2\pi}\int_{\Gamma} \left(\sigma_D\left(N_{ij} - \frac{\delta_{ij}}{3}\right) + \sigma_M M_{ij} + \sigma_L L_{ij}\right)d\Gamma. \tag{8.42}$$

Constitutive relations between microstrains and microstresses can be defined in different ways. An intensive development in this area was undertaken by Bažant [123]. Originally, the constitutive relations were defined as smooth curves, but due to several insufficiencies they were replaced by the concept so-called stress-strain boundaries. In this concept, the stress is evaluated as a minimum of of the elastic prediction and the boundary stress. Also other improvements, such as shear components on the microplane and volumetric-deviatoric split of the normal stress have been introduced.

In the following a computational algorithm of the microplane model proposed by Bažant is outlined:

1. The new macroscopic strain tensor ε_{ij} and its increment $\Delta\varepsilon_{ij}$ and previous microstrains σ_N^p, σ_V^p, σ_L^p, σ_M^p for each microplane are given at the beginning of the load step.
   Then, for each microplane:

2. By using of projection tensors, $\Delta\varepsilon_N = N_{ij}\Delta\varepsilon_{ij}$, $\Delta\varepsilon_V = \frac{\Delta\varepsilon_{kk}}{3}$, $\Delta\varepsilon_D = \Delta\varepsilon_N - \Delta\varepsilon_V$, $\Delta\varepsilon_L = L_{ij}\Delta\varepsilon_{ij}$, $\Delta\varepsilon_M = M_{ij}\Delta\varepsilon_{ij}$ are obtained.

3. First, the volumetric stress is calculated. It is evaluated from elastic prediction $\sigma_V^e = \sigma_V^p + E_V\Delta\varepsilon_V$, where E_V is the elastic volumetric modulus, and from boundary values for positive (σ_V^{b+}) and negative (σ_V^{b-}) strains. Volumetric stress is then given by $\sigma_V^* = min(max(\sigma_V^b, \sigma_V^e), \sigma_V^{b+})$.

4. Analogically, the deviatoric stress is calculated as $\sigma_D = min(max(\sigma_D^{b-}, \sigma_D^e), \sigma_D^{b+})$, where $\sigma_D^e = \sigma_D^p + E_D\Delta\varepsilon_D$, E_D is the elastic deviatoric modulus, and σ_D^{b-} and σ_D^{b+} are deviatoric boundary values.

5. The normal microstress is given by the summation of volumetric and deviatoric parts as $\sigma'_N = \sigma_V^* + \sigma_D$.

6. The boundary for normal stress must be also checked and the normal stress recalculated as
$$\sigma_N = min(\sigma'_N, \sigma_N^{b+}). \tag{8.43}$$

7. After the normal stresses from all microplanes are known, compute the volumetric stress as the mean microplane normal stress over the surface of the hemisphere, but prevent this value to exceed its boundary as follows
$$\sigma_V = min\left(\frac{1}{2\pi}\int_\Gamma \sigma_N d\Gamma, \sigma_V^*\right). \tag{8.44}$$

8. For all microplanes recalculate
$$\sigma_D = \sigma_N + \sigma_V. \tag{8.45}$$

9. Compute shear stress components $\sigma_T = min(|\sigma_T^b|, |\sigma_T^e|)$, where T means the direction L or M and $\sigma_T^e = \sigma_T^p + E_T \Delta\varepsilon_T$. E_T is the elastic modulus for shear components and σ_T^p is the boundary value.

10. Update all microplane values σ_V, σ_D, σ_L, σ_M.

11. Finally, the macroscopic stress tensor σ_{ij} can be computed using Eq. 8.42.

Many aspects of these models put high requirements even on todays powerful computers. Implicit methods are not suitable with respect to microplane models and lead to long computational times. In contrast, explicit integration methods blend well with the microplane model concept. Computational times can be strongly reduced by parallelisation, which can be implemented into an existing object oriented finite element environment [127].

8.5 Cellular Automata

Cellular automata are synchronous algorithms that describe the discrete spatial and temporal evolution of complex systems by applying local (or sometimes mid-range) deterministic or probabilistic transformation rules to lattice cells with local connectivity. Cellular automata do not have restrictions in the type of elementary entities or rules they use. They can map such different situations as the distribution of the values of state variables in a finite difference simulation, the colors in a blending algorithm, the elements of fuzzy sets, or growth and decay processes of cells [128].

The local interaction of neighboring lattice points in a cellular automaton is specified through a set of transformation rules. While the original automata, proposed by Neumann, were designed with deterministic transformation rules, probabilistic transformations are conceiveable as well. The value of an arbitrary state variable ξ assigned to particular lattice site at a time $(t + \Delta t)$ is determined by its present state (t_0) (or its last few states t_0,$t_0 - \Delta t$, etc.) and the state of its neighbours. Using the last two time, steps for the evolution of a 1D cellular automaton, can be put formally by writing $\xi_j^{t_0+\Delta t} = f(\xi_{j-1}^{t_0-\Delta t}, \xi_j^{t_0-\Delta t}, \xi_{j+1}^{t_0-\Delta t}, \xi_{j-1}^{t_0}, \xi_j^{t_0}, \xi_{j+1}^{t_0})$ where $\xi_j^{t_0}$ is the value of the variable at time t_0 at node j. The positions $(j+1)$ and $(j-1)$ indicate the nodes in the neighbourhood of position j (in D). The function f specifies the set of transformation rules. If the state of the node depends only on its nearest neighbours (NN) the array is referred to as von Neumann neighbouring. If both the NN and the next-nearest neighbours (NNN) determine the ensuring state of the node, the array is called Moore neighbouring.

One typical application of cellular automata for materials-related simulations consists in mapping the values of relevant state variables onto the points of a lattice and using the local finite difference formulations of the partial differential equations of the underlying model as transformation rules. The particular versatility of cellular automata for microstructure simulations especially in the fields of recrystallisation, dendritic growth, grain growth and phase transformation phenomena is due to its flexibility in considering a large variety of variables and transformations [128].

8.5.1 Cellular Automata based Material Model for FEM Simulations

Thermo-mechanical simulations of metal-forming operations typically use the finite element method to study the evolution of deformation variables e.g. stress, strain and temperature. The relationship between the externally applied deformation and the internally evolving variables can be captured by a material model that is expressed by physically based equations. Such physically-based relations use the fundamental variables of dislocation density (ρ), subgrain size (δ) and misorientation angle (θ) to capture the local hardening and softening phenomena based on the externally applied deformation. The local effects are summed at the global structural level to arrive at the structural stress patterns. Recently, physically-based formulations have utilised the merits of artificial intelligence (AI) tools, particularly the concept of neuro-fuzzy (NF) architectures, to define the material model.

NF models work well in situations where the experimental data on the evolution rates of ρ, δ and θ are sparse or diffcult to obtain for the entire workable range of deformation conditions. To carry out simulation studies at the structural level, the physically-based formulations need to be coded in situ within the finite element solver using user-subroutines. A particular area of interest is the effect of the initial microstructure on the evolution rates of ρ, δ and θ. Experimental evidence shows that the initial distribution of grain size, particularly the grain boundaries, play an important role in defining the evolution rules. An effcient method of capturing the initial and evolving microstructural information is to use a combination of cellular automata (CA) and finite element (FE) techniques, a result often termed CAFE. It uses the scale-invariant spatial characteristic of CA to define the micro-feature and it links the CA cells to the integration point of a finite element (Fig. 8.6) [129].

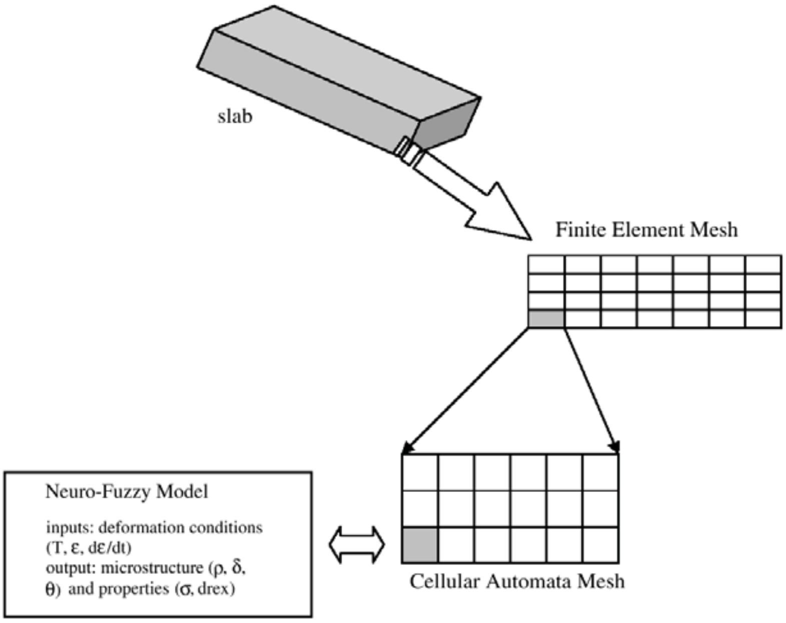

Figure 8.6: Schematic diagram of the nf-CAFE model [129].

The concept of Cellular Automata was introduced by von Neumann in the early 1940s for the simulation of self-reproducing automata and population evolution. Early developments in application were to the fields of fluid dynamics and biological processes, and recently it has been applied to the simulation of material microstructure.

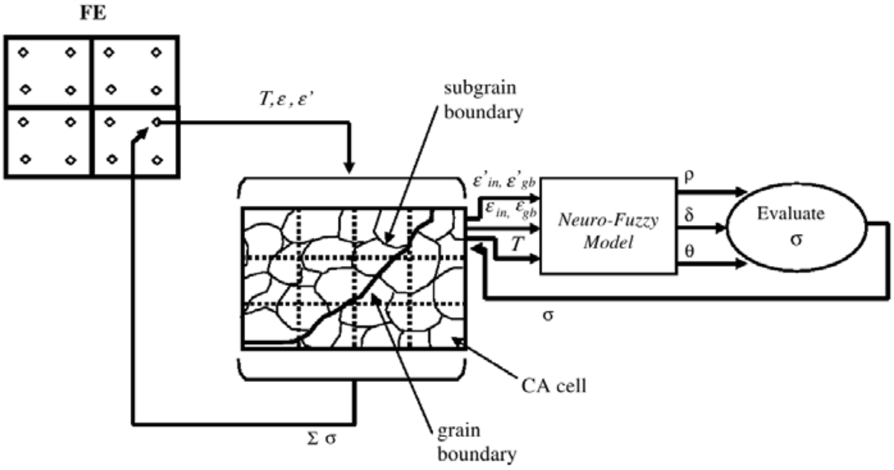

Figure 8.7: The physically-based model formulation and its linkage to each integration point of a finite element. However, the linkage is made at each CA cell and its state, i.e. whether it is a grain boundary or a grain interior [129].

In the CAFE framework, the material model is defined by the rate of evolution of ρ, δ and θ at each time increment. The rate constants used in the evolution equations of ρ, δ and θ are based on a neuro-fuzzy model. A schematic illustration of this approach is shown in Fig. 8.7 for a single element highlighted in this concept [129].

8.5.2 Monte Carlo Method

The Monte Carlo Method as known in materials community is an adaption of a method used primarily to study the statistical physics of phase equilibria. The name "Monte Carlo" was coined by Metropolis during the Manhattan Project of World War II, because of the similarity of statistical simulation to games of chance, and because Monte Carlo, the capital of Monaco was a center for gambling. Monte Carlo now refers to any method that utilises sequences of random numbers to perform statistical simulation. The main requirement to use Monte Carlo method for simulation of a physical system is that it must be possible to describe the system in terms of probability density function (PDF), also called partition function (Z). Once the PDF or Z for a system is known, then the simulation begins by random "sampling" from the PDF, and subsequently determining the desired properties of the sample by conducting some kind of a "trial". There must be a rule available, based on some reasonable mathematical and/or physical thery, to decide the outcome of such a trial. Many trials are conducted and outcomes of all of these trials are recorded. The final step in the MC method is that the behaviour of the overall system is obtained by computing the average of outcomes of the trails conducted.

The genesis of the Ising model lies in solid state physics community and the development of models for ferromagnetic materials. The Ising model [130] represents a magnetised materia as a collection of spins where only two states are possible, namelly up or down. Potts [131] later generalised the Ising model and allowed for Q states for each particle in the system, hence the term "*Q-state Ising model*". It is the Potts model that has been used most extensively to simulate mesoscopic (where the length scale is the order of the grain size) behaviour of materials such as recrystallisation, grain growth and texture evolution [128].

8.6 Experimental Simulation

Mechanical material data are commonly determined by uniaxial loading, but components are exposured to multiaxial loads in general. For this reason stresses and strains cannot be specified by a scalar value in a component part. To exactly describe stress and strain conditions in a three dimensional continuum, tensors for the stress σ and strain ε have to be introduced. Path- (ε and $\dot{\varepsilon}$) and force (σ) dimensions are coupled through a material law, in general formulation

$$\dot{\varepsilon}_p = \dot{\varepsilon}_p(\sigma, T, S_i) \tag{8.46}$$

with a composition of evolution equations for the inner variables S_i, $(i = 1,...,n)$ which denote microstructure parameter and

$$\dot{S}_i = \dot{S}_i(\sigma, T, S_i), \tag{8.47}$$

where $\dot{S}_i$ denotes the temporal variation of the microstructure parameters S_i. In multi-axially loaded componts these correlations have to be formulated with tensors [44].

Strain Rate Dependence

In the uniaxial tensile test, the technical strain ε is defined by the relation of the elongation Δl to the initial length l_0 of the specimen. At high strain rates, this relation is insufficient for a reasonable description of the actual strain condition according to the material response. For this reason, the true stress $d\hat{\varepsilon}$ is defined by the relation of the differential elongation dl to the current specimen length l:

$$\hat{\varepsilon} = \int\limits_{l_0}^{l} \frac{dl}{l} = ln\frac{l}{l_0}. \tag{8.48}$$

A strain rate in a three-dimensional continuum requires the ability to define independent elongations of a line element in all possible directions as well as variations of the angle of such a line element. A definition of a continuum after Lagrange may be as follows: A place in the deformed body R is denoted as reference configuration R_0 due to his coordinates x with relation to the coordinate system X. As reference configuration the idle state is considered. The displacement vector u describes the displacement of the point P to P'

$$x = X + u. \tag{8.49}$$

A line element dX in the reference configuration changes due to the deformation of the body into a line element dx with the following relation between dx and dX

$$dx = \frac{\partial x}{\partial X} dX = F dX. \tag{8.50}$$

Hence the definition of the deformation gradient F results in

$$F = \frac{\partial x}{\partial X}. \tag{8.51}$$

The length squares of the line elements dX and dx are defined by $(dS)^2 = dX.dX$ and $(ds)^2 = dx.dx$. The difference of these length squares $(ds)^2 - (dS)^2$ provides the basic for the definition of the Green-Lagrange strain tensor $\mathbf{E}$:

$$(ds)^2 - (dS)^2 = 2dX\boldsymbol{E}dX, \tag{8.52}$$

where **E** can be expressed with the help of the deformation gradient F

$$E = \frac{1}{2}(F^T F - I), \tag{8.53}$$

as well as by partial derivations of the displacement vector u

$$E_{ij} = \frac{1}{2}(u_{i,j} + u_{j,i} + u_{k,i}u_{k,j}). \tag{8.54}$$

The term $u_{i,j}$ determines the derivation of the component u_i by the coordinate X_j. The strain tensor ε of the geometrically linear theory results due to negligence of the multiplication term in Eq. 8.54 in

$$\varepsilon_{i,j} = \frac{1}{2}(u_{i,j} + u_{j,i}). \tag{8.55}$$

In the uniaxial tensile test, the component E_{11} of the Green-Lagrange strain tensor results by

$$E_{11} = \varepsilon_{11} + \frac{1}{2}(\varepsilon_{11})^2 \tag{8.56}$$

At strain rates of $\varepsilon_{11} = 10\%$, the maximum deviation between the tecnical strain ε_{11}, the true strain $\hat{\varepsilon}$ and the first component of the Green-Langrange strain tensor **E** according to 8.48 is about 10% [44].

Stress Rate Dependence

In the uniaxial test there is a difference between the technical stress, where the power is related to the initial cross section of the specimen and the true stress, defined as quotient from power over the current cross section. Analogical to the strain rates, also dimensions for the description of the stress condition in the three dimensional continuum have to be declared. For this purpose, a body R is cutted into two parts R_1 and R_2. The influence of R_2 onto an infinitesimal surface element ΔA of the part R_1 can be expressed by the force Δp

$$\Delta p = t\Delta A. \tag{8.57}$$

The force t related to the surface element is mentioned as stress vector. The partition of the stress vector into the direction of the components of the normal vector **n** defines the Cauchy stress tensor $\boldsymbol{\sigma}$

$$t = n\sigma, \tag{8.58}$$

which is related to the actual configuration R and represents the true stress of the deformed body. Sometimes it is advantageous to operate with stress tensors, defined in the initial configuration R_0. Suchlike stress dimension is the 1. Piola-Kirchhoff stress tensor

$$\Sigma^I = det(F)F^{-1}\boldsymbol{\sigma}. \tag{8.59}$$

As $\boldsymbol{\sigma}$ is a symmetric tensor, the asymmetry of the 1. Piola-Kirchhoff stress tensor results from the asymmetry of F^{-1}, which often is disadvantageous concerning the solution of practical problems. For this reason, the 2. Piola-Kirchhoff stress tensor Σ^{II} is introduced

$$\Sigma^{II} = \Sigma^I(F^{-1})^T = det(F)F^{-1}\boldsymbol{\sigma}(F^{-1})^T. \tag{8.60}$$

For the stress rates of a specimen with the initial cross section A_0, resulting from the force F during an uniaxial tensile test with the assumption of incompressible material behaviour, results

$$\sigma_{11} = \frac{F(\varepsilon_{11}+1)}{A_0}, \tag{8.61}$$

$$\Sigma^{I} = \frac{F}{A_0}, \tag{8.62}$$

$$\Sigma^{II} = \frac{F}{A_0(\varepsilon_{11}+1)}. \tag{8.63}$$

At a strain of $\varepsilon_{11} = 10\%$, a maximum deviation between the stress rates of about 20% occurs. During the solution of mechanical problems, it is important to esteem that the used strain- and stress tensors are conjugated ernergetically to each other. The Green-Lagrange strain tensor $\mathbf{E}$ and the second Piola-Kirchhoff stress tensor Σ^{II} satisfy this criteria. By the reason of invariation of the components of Σ^{II} against fixed body rotation, the temporal derivation of the Green-Lagrange strain tensor $\dot{\boldsymbol{E}}$ can be used as a degree of the strain rate. Thereby the polar decomposition of the deformation gradient is not necessary to perform [44].

High temperature fatigue is a very complex subject and involves the intervention of various time dependent processes such as creep, oxidation, dynamic strain ageing, mechanical instability, microstructural degradation, precipitation, etc. Furthermore, at elevated temperatures, various factors such frequency, strain rate, wave form, hold position, hold duration and strain range have been shown to exert greater influence on lifetime [132].

To represent material behaviour in a laboratory test, the thermal strains are replaced by a mechanical strain, introduced and controlled under isothermal conditions. Start-up and shut-down cycles are replaced by a symmetrical and continuous fatigue cycle of equal strain rates in tension and compression (Fig. 8.8) with a hold period at a constant peak strain to simulate the on-load perid, i.e. creep-fatigue interaction.

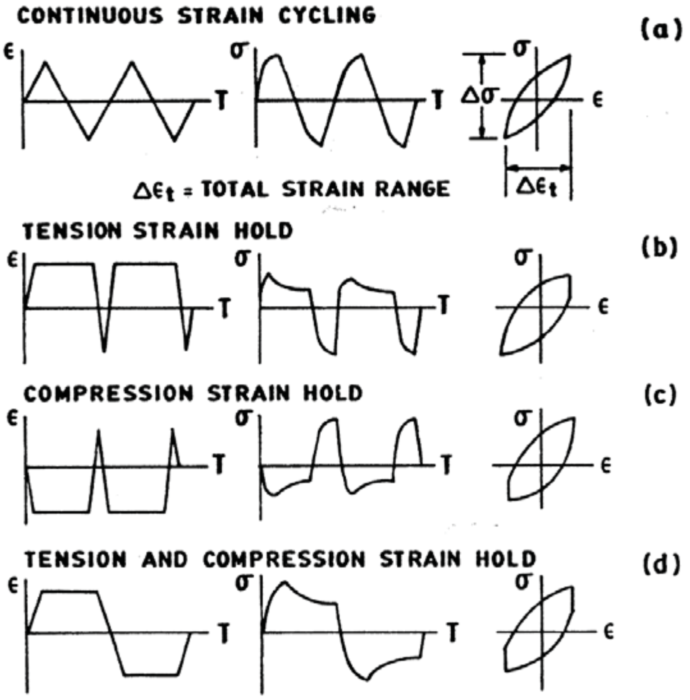

Figure 8.8: Typical waveforms for strain controlled fatigue testing [132].

Slow-fast and fast-slow strain-time wave forms (Fig. 8.9) represent another category used to evaluate creep-fatigue interaction effects [133]. In the slow-fast cycle, the tensile strain rate is less than in the compression part of the cycle, while in the fast-slow cycle, the compression strain rate is less than in tension. Tension hold alone, compression hold alone, slow-fast and fast-slow wave forms are generally considered as unbalanced cycles. Creep-fatigue interaction can also be evaluated using continuous cycling at low frequencies or strain rates.

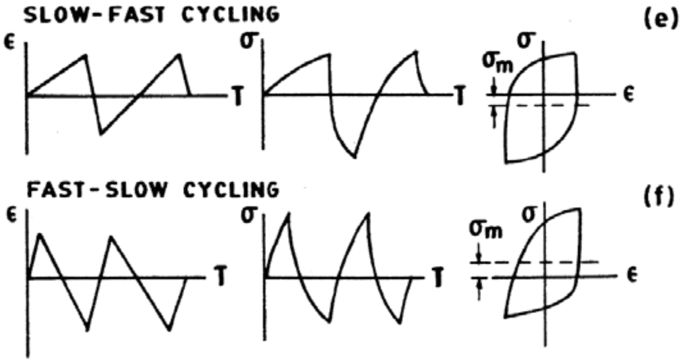

Figure 8.9: Typical waveforms for strain controlled fatigue testing [133].

The purpose of such experiments is to review the phenomenological effects of various strain-time wave forms on LCF and creep-fatigue interaction life.

Thermal and thermo-mechanical fatigue experiments to simulate creep and creep-fatigue damage are described in section 5.1.2.1.

9 Conclusion and Future Work

The aim of this literature survey is to depict, select and describe methods which are suitable for a characterisation of local damage in hot work tool steels in use. Due to the alloying concept which is the basis for the evolution of a certain structure, the required material properties can be adjusted by several heat treatment conditions. The most important fact in such materials is the secondary hardenenig effect at tempering temperatures of about 500-600°C. The application of hot work tool steels and the adjusting of required material properties by several treatment conditions as well as characteristic phases are mentioned in chapter 2. Microstructural elements like precipitations, subgrain structure and dislocations, respectively, specified by parameters, and the structure evolution during cyclic thermo-mechanical loads is displayed in chapters 3 and 4. It is from great importance to exactly know the influence of thermal and mechanical loads onto the microstructure, on which the mechanical properties depend on. Several competing hardening and softening mechanisms appear. The dominating damage mechanism in hot work tool steels is creep-fatigue, ocurring due to an overlapping of thermal and mechanical loads. This mechanism is worse than just pure fatigue, which cause cracks, or creep which cause mainly pores, the combination of such influences leads to an earlier component failure. Models to describe the damage were depicted in chapter 6. There exist void based criteria like the model according to McClintock, which is an integral approach to describe failure by void initiation and growth followed by coalescense, the Rice and Tracey model considering the ductile growth of voids in continuum plasticity, and the modified version for an application in FEM programs. The Gurson model, for example, is a yield criterion which is based on the void volume fraction. Continuum damage mechanics criteria (the concepts according to Lemaitre, Yeh and Krempl) are described in chapter 6.2. The effective stress concept according to LeMaitre introduces a damage variable, which describes the process of material damage and hence the increasing stress (i.e. effective stress) due to the decrease of the load carrying cross section can be calculated. Yeh and Krempl proposed an incremental multiaxial life prediction law based on a thermovicoplasticity law combined with a multiaxial damage accumulation law. A variety of models to determine the lifetime at cyclic high temperature loading exist, and they can be classified into four main groups, namely empiric models which predict lifetime by implementating a damage parameter, damage mechanic methods which are commonly based on the implementation of a whole damage function, physical approaches describing the damage evolution considering the movement of atoms, vacancies and dislocations, and fracture mechanical methods which describe the crack growth from an initial size until a critical, material depending parameter. With the focus on creep-fatigue simulation, several methods generating reasonable results exist. With elastic-viscoplastic models (e.g. Chaboche) coupled with FEM, the inelastic strain rate is calculated and damage accumulation can be derived. Crystal plasticity consideres the phenomena ocurring in just one crystal (i.e. grain, subgrain). Crystal plasticity coupled FEM is an application, where every finite element is meant to be one single crystal with different orientation. The whole structure is then a copound of these single crystals with resulting macroscopic response by calculation of each connected single finite element. The representative volume element method consideres a representative structure section, which can be understood as a procedure to derive the kinetics of the macro continuum with a point wise attached microstructure. In the cellular automata approach, different states of cells correspond to a different progress in damage. Such structures could be taken from EBSD analysis and implemented into the cellular automata framework. Several experimental simulation methods to evaluate creep-fatigue interaction effects , e.g. under strain controlled test conditions are mentioned.

The future work is now to analyse the material behaviour of the four Böhler hot work tool steels W300, W360, W400 and W750. These materials are tools for extrusion of light metals as well as drop forging. Tools for extrusion have to withstand creep-fatigue loads, whereas forging tools are exposured to shorter cycle times, which provides mainly thermal fatigue. Additional experimental data of these four hot work tool steels have to be ascertained. The difference in friction behaviour of nitrided tools in comparison to unnitrided ones should be evaluated by a conclusion of various measured forming pressures, stresses in the container and temperatures, respectively, for nitrided/unnitrided tools. A concept for an experimental test device simulating a forging process is required for the verification and evaluation of boundary conditions implemented into FEM simulations. To simulate the local load history of critical tool regions experimentally, the critical load until cracks occur should be determined. Thereby the GOM/ARAMIS system can be applied to measure strains at the surface as well as cracks could be detected. An interesting thing would be the investigation of damaged tool materials from industrial cooperators in the extrusion and forging branch. The transfer of important data, like process parameters and lifetime of tools would be very helpful to analyse and optimise industrial processes.

List of Figures

List of Tables

Bibliography

[1] G. Roberts, G. Kraus and R. Kennedy: “Tool Steels 5th ed.”, *ASM International, Metals Park Ohio* 1998.

[2] J. Davies: “Tool Materials”, *ASM Speciality Handbook, ASM International, Materials Park, Ohio* p. p. 251, 1995.

[3] F. Pickering: “The Properties of Tool Steels for Mould and Die Applications”, *Tool Materials for Molds and Dies, Proceedings of an international Conference* pp. 1–32, 1987.

[4] W. Jänicke, W. Dahl, H. Klärner, W. Pitsch, D. Schauwinhold, W. Schlüter and H. Schmitz: *Werkstoffkunde Stahl, Band 1*, Springer Verlag, Berlin Heidelberg New York Tokyo, 1984.

[5] J. Mayerhofer: *Werkstoffkunde der Stähle - Part: Hochlegierte Stähle*, 1998.

[6] Böhler: *Böhler Edelstahl - Handbuch*, Böhler Edelstahl GmbH, 2000.

[7] Böhler: “Böhler W400 VMR”, *Tech. rep.*, Böhler Edelstahl GmbH, 2004.

[8] V. Leskovšek, B. Šuštaršič and G. Jutriša: “The Influence of austenitizing and tempering Temperature on the Hardness and Fracture Toughness of hot-worked H11 Tool Steel”, *Journal of Materials Processing Technology, 178* pp. 328–334, 2006.

[9] J. Sjöström and J. Bergström: “Thermal Fatigue Testing of chromium martensitic hot-work Tool Steel after different austenitizing Treatments”, *Journal of Materials Processing Technology, 153-154* pp. 1089–1096, 2004.

[10] M. Terčelj, A. Smolej, P. Fajfar and R. Turk: “Laboratory Assesment of Wear on nitrided Surfaces of Dies for Hot Extrusion of Aluminium”, *Tribol. Int., 40* pp. 374–384, 2007.

[11] J. Sjöström and J. Bergström: “Microstructural Stability and Strength of chromium martensitic hot-work Tool Steels”, *Tech. rep.*, 2003.

[12] J. Martin: *Micromechanics in Particle Hardened Alloys*, Cambridge Solid State Science Series, Cambridge University Press, 1980.

[13] B. Reichert, Y. Estrin and H. Schuster: “Implementation of Precipitation and Ripening of Second-Phase Particles in the Constitutive Modelling of Creep”, *Scripta mater., 38* pp. 1463–1468, 1998.

[14] J. Hirth and J. Lothe: *Theory of Dislocations*, Krieger Publishing Company, Malbar, Florida, 1992.

[15] J. Lothe: "Theory of Dislocation Climb in Metals", *Journal of Applied Physics, 31* pp. 1077–1087, 1960.

[16] Q. Kong and Y. Li: "Investigation of the Climb of Extended Dislocations during High-Temperature Creep", *Philosophical Magazine A, 68* pp. 113–119, 1993.

[17] E. Arzt and M. Ashby: "Threshold Stress in Materials Containing Dispersed Particles", *Scripta Metallurgica,16* pp. 1285–1290, 1982.

[18] V. Vitek: "Theory of the Core Structures of Dislocations in BCC-Metals", *Crystal Lattice Defects, 5* pp. 1–34, 1974.

[19] A. Argon and S. Takeuchi: "Internal Stress in Power-Law Creep", *Acta Metallurgica, 29* pp. 1877–1884, 1981.

[20] A. Orlova, K. Miclicka and F. Dobes: "Choice of Evolution Equation for Internal Stress in Creep", *Materials Science and Engineering, A194* pp. 9–16, 1995.

[21] R. Honeycombe: *The Plastic Deformation of Metals*, Edward Arnold, London, second edition, 1982.

[22] P. Weinert: *Modellierung des Kriechens von ferritisch/martensitischen 9-12% Cr-Stählen auf mikrostruktureller Basis*, Ph.D. thesis, Technische Universität Graz, 2001.

[23] G. Gottstein and A. Argon: "Dislocation Theory of Steady State Deformation and its Approach in Creep and Dynamic Tests", *Acta Metallurgica, 35* pp. 1261–1271, 1987.

[24] J. Friedel: *Dislocations*, Pergamon Press, London, New York, Paris, 1967.

[25] A. Seeger and H. Bross: "Physik", *J. Phys. Chem. Sol, 16* p. 253, 1956.

[26] A. Seeger and S. Mader: *Physica Status Solidi, 1* p. 78, 1961.

[27] G. Gottstein: *Physikalische Grundlagen der Materialkunde*, Springer-Verlag Berlin Heidelberg New York, 2001.

[28] N. Ghoniem, J. Matthews and R. Amodeo: "A Dislocation Model for Creep in Engineering Materials", *Res Mechanica, 29* pp. 179–219, 1990.

[29] F. Garofalo: *Fundamentals of Creep and Creep-Rupture in Metals*, The MacMillan Company, 1965.

[30] F. Humphreys: "A New Analysis of Recovery, Recrystallisation and Grain Growth", *Materials Science and Technology, 15* pp. 37–44, 1999.

[31] J. Verhoeven: *Fundamentals of Physical Metallurgy*, John Wiley and Sons, New York, first edition, 1975.

[32] R. Sandström: "Subgrain Growth occurring by Boundary Migration", *Acta Metallurgica, 25* pp. 905–911, 1977.

[33] D. Hull and D. Bacon: *Introduction to Dislocations*, Pergamon Press, third edition, 1981.

[34] A. Orlova: "On the Relation between Dislocation Structure and Internal Stress measured in Pure Metals and Single Phase Alloys in High Temperature Creep", *Acta Metallurgica et Materialia, 39* pp. 2805–2813, 1991.

[35] P. Polcik: *Modellierung des Verformungsverhaltens der warmfesten 9-12% Cr-Stähle im Temperaturbereich von 550-650C*, Ph.D. thesis, Werkstofftechnik, Shaker Verlag, 1999.

[36] O. Ruano, J. Wadsworth and O. Sherby: "Harper Dorn Creep in Pure Metals", *Acta Metallurgica, 36* pp. 1117–1128, 1988.

[37] F. Roters, D. Raabe and G. Gottstein: "Work Hardening in Heterogeneous Alloys - A Microstructural Approach based on Three Internal State Variables", *Acta Materialia, 40* pp. 4181–4189, 2000.

[38] J. Chaboche: "Cyclic Viscoplastic Constitutive Equations, Part I: A Thermodynamically Consistent Formulation", *Journal of Applied Mechanics, 60* pp. 813–821, 1993.

[39] M. Ashby and D. Jones: *An Introduction to Properties, Applications and Design*, Elsevier Butterworth-Heinemann, 2005.

[40] C. Sommitsch, T. Wlanis and V. Wieser: "Modelling of Creep-Fatigue in Extrusion Dies", *Tech. rep.*, Chair of Metal Forming, Böhler Edelstahl GmbH, 2006.

[41] C. Sommitsch, R. Sievert, T. Wlanis, B. Günther and V. Wieser: "Modelling of Creep-Fatigue in Containers during Aluminium and Copper Extrusion", *J. Comput. Mat. Sci.* 2006.

[42] E. Orowan: *Dislocations in Metals*, AIME, New York, 1954.

[43] R. Rie and R. Schmidt: "Low-Cycle Fatigue unter besonderer Berücksichtigung der Temperatur und des Umgebungsmediums", *Ermüdungsverhalten metallischer Werkstoffe* pp. 397–419, 1985.

[44] R. Teteruk: *Modellierung der Lebensdauer bei thermomechanischer Ermüdungsbeanspruchung unter Berücksichtigung der relevanten Schädigungsmechanismen*, Ph.D. thesis, Universität Siegen, 2001.

[45] B. Günther and R. Sievert: "Bestimmung der Materialparameterwerte des viskoplastischen Chaboche-Modells und einer zeitlich inkrementellen Lebensdauerregel für die Hochtemperatur-Ermüdung des Werkstoffs Böhler W400 in dem Temperaturbereich von 470-590C", *Tech. rep.*, BAM-V.2 05/02, 2005.

[46] H. Sehitoglu: "Thermo-Mechanical Fatigue Life Prediction Models", *Advances in Fatigue Lifetime Predictive Techniques, ASTM STP 1122* pp. 47–76, 1992.

[47] R. Ohtani: "Substance of Creep-Fatigue Interaction Examined from the Point of View of a Crack Propagation Mechanics", *Proc. Second Int. Conf. on Low Cycle Fatigue and Elasto-Plastic Behaviour of Materials, Elsevier, London* pp. 211–222, 1988.

[48] A. Nitta and K. Kuwabara: "Thermal-Mechanical Fatigue Failure and Life Prediction", *Current Japanese Materials Research, Vol. 3,Elsevier, New York* pp. 203–222, 1988.

[49] H. Riedel: *Fracture at High Temperatures*, Springer-Verlag Berlin Heidelberg New York, 1987.

[50] A. Sinha: *Ferrous Physical Metallurgy*, Butterworths, 1989.

[51] R. Raj and A. Gosh: "Micromechanical Modelling of Creep using Distributed Parameters", *Acta Metallurgica, 29* pp. 283–292, 1981.

[52] R. Cahn, P. Haasen and E. Kramer: *Materials Science and Technology*, Materials Science and Technology, volume 5, 1991.

[53] S. Goods and L. Brown: "The Nucleation of Cavities by Plastic Deformation", *Perspectives in Creep Fracture* pp. 71–86, 1983.

[54] A. Cocks and M. Ashby: "On Creep Fracture by Void Growth", *Progress in Materials Science, 27* pp. 189–244, 1982.

[55] M. He and J. Hutchinson: "The Penny-Shaped Crack and the Plain Strain Crack in an Infinite Body of Power-Law Material", *Journal of Applied Mechanics, 48* pp. 830–840, 1981.

[56] K.-S. Cheong, M. Smillie and D. Knowles: "Predicting Fatigue Crack Initiation Through Image-Based Micromechanical Modeling", *Acta Materialia, 55* pp. 1757–1768, 2007.

[57] A. Freudenthal: *The Inelastic Behaviour of Metals*, Wiley, New York, 1950.

[58] S. Clift, P. Hartley, C. Sturgess and G. Rowe: "Fracture Prediction in plastic Deformation Process", *International Journal of Mechanical Sciences, 32* pp. 1–17, 1990.

[59] M. Cockroft and D. Latham: "Ductility and the Workability of Metals", *Journal of the Institute of Metals, 96* pp. 33–39, 1968.

[60] A. Argon, J. Im and A. Needleman: "Distribution of plastic Strain and negative Pressure in necked Steel and Copper Bars", *Metallurgical Transactions A, 6A* pp. 815–824, 1975.

[61] A. Argon, J. Im and R. Safogulu: "Cavity Formation from Inclusions in ductile Fracture", *Metallurgical Transactions A, 6A* pp. 825–837, 1975.

[62] T. Ayada and K. Mori: “Centralbursting in Extrusion of inhomogeneous Materials”, *Proceedings of the 1. International Conference on Technology of Plasticity, Advanced Technology of Plasticity, 1* pp. 553–558, 1984.

[63] S. Oh, C. Chen and S. Kobayashi: “Ductile Fracture in axisymmetric Extrusion and Drawing: Part II. Workability in Extrusion and Drawing”, *Transactions of the American Society of Mechanical Engineers, 101* pp. 36–44, 1979.

[64] K. Osakada, A. Watadani and H. Sekiguchi: “Ductile Fracture of carbon Steel under cold Metal Forming Conditions. Part I. Tension and Torsion Tests under Pressure”, *Bulletin of the Japan Society of Mechanical Engineers, 20(150)* pp. 1557–1565, 1977.

[65] K. Osakada, A. Watadani and H. Sekiguchi: “Ductile Fracture of carbon Steel under cold Metal Forming Conditions. II. Effect of metallurgical Structure”, *Bulletin of the Japan Society of Mechanical Engineers, 21(158)* pp. 1236–1243, 1978.

[66] P. Lee and H. Kuhn: “Fracture in cold upset Forging - A Criterion and Model”, *Metallurgical Transactions,4* pp. 969–974, 1973.

[67] R. Sowerby, I. O’Reilly, N. Chandrasekaran and N. Dung: “Materials Testing for cold Forging”, *Journal of Engineering Materials and Technology, 106* pp. 101–106, 1984.

[68] R. Sowerby and N. Chandrasekaran: “The upsetting and free Surface Ductility of some commercial Steels”, *Journal of Applied Metalworking, 3(3)* pp. 257–263, 1984.

[69] F. McClintock: “A Criterion for ductile Fracture by the Growth of Holes”, *Journal of Applied Mechanics, 35* pp. 363–371, 1968.

[70] J. Rice and D. Tracey: “On the ductile Enlargement of Voids in triaxial Stress Fields”, *Journal of the Mechanics and Physics of Solids, 17* pp. 201–217, 1969.

[71] M. Oyane: “Criteria of ductile fracture strain”, *Bulletin of the Japan Society of Mechanical Engineers, 15(90)* pp. 1507–1513, 1972.

[72] M. Oyane, T. Sato, K. Okimoto and S. Shima: “Criteria for ductile Fracture and their Applications”, *Journal of Mechanical Working Technology,4* 1980.

[73] A. Gosh: “A Criterion for ductile Fracture in sheets under biaxial Loading”, *Metallurgical Transactions A, 7A* pp. 523–533, 1976.

[74] A. Gurson: “Continuum Theory of ductile Rupture by Void Nucleation and growth: Part I Yield Criteria and Flow Rules for porous ductile Media”, *Journal of Engineering Materials and Technology, Transactions of the ASME, 99* pp. 2–15, 1977.

[75] V. Tvergaard: “Influence of Void Nucleation on ductile shear Fracture at a free Surface”, *Journal of the Mechanics and Physics of Solids, 30* pp. 399–425, 1982.

[76] A. Needleman and V. Tvergaard: “An Analysis of ductile Rupture in notched Bars”, *Journal of the Mechanics and Physics of Solids, 32* pp. 461–490, 1984.

[77] V. Tvergaard and A. Needleman: “Ananlysis of the Cup-Cone Fracture in a round tensile Bar”, *Acta Metallurgica, 32* pp. 157–169, 1984.

[78] S. Shima and M. Oyane: “Plasticity Theory for porous Metals”, *International Journal of Mechanical Sciences, 18(6)* pp. 285–291, 1976.

[79] R. Green: “A Plasticity Theory for porous Solids”, *International Journal of Mechanical Sciences, 14* pp. 215–224, 1972.

[80] J. LeMaitre: *A Course on Damage Mechanics*, Springer Verlag, Berlin, Heidelberg, New York, 1996.

[81] J. Lemaitre: “Local Approach of Fracture”, *Engineering Fracture Mechanics, 25(5-6)* pp. 523–537, 1986.

[82] R. Chaouadi, P. de Meester and W. Vandermeulen: “Damage Work as ductile Fracture Criterion”, *International Journal of Fracture, 66* pp. 155–164, 1994.

[83] W. Tai and B. Yang: “A new damage Mechanics Criterion for ductile Fracture”, *Engineering Fracture Mechanics, 27(4)* pp. 371–378, 1987.

[84] P. Bolt: *Prediction of ductile Fracture*, Ph.D. thesis, 1989.

[85] A. Ragab and A. Saleh: “Evaluation of constitutive Models for voided Solids”, *International Journal of Plasticity, 15* pp. 1041–1065, 1999.

[86] N. Yeh and E. Krempl: “An Incremental Life Prediction Law for Multiaxial Creep-Fatigue Interaction and Thermomechanical Loading”, *Advances in Multiaxial Fatigue, ASTM STP 1191* pp. 107–119, 1993.

[87] S. Manson and G. Halford: “Multiaxial Low-Cycle Fatigue of Type 304 Stainless Steel”, *Journal of Engineering Materials and Technology, 99* pp. 283–285, 1977.

[88] M. Brown and K. Miller: “A Theory for Fatigue Failure under Multiaxial Stress-Strain Conditions”, *Proceedings of the Institute of Mechanical Engineers, 187* pp. 217–229, 1973.

[89] S. Majumdar: “Designing Against Low-Cycle Fatigue at Elevated Temperature”, *Nuclear Engineering and Design, 63* pp. 121–135, 1981.

[90] M. Satoh and E. Krempl: “An Incremental Life Prediction Law for Creep-Fatigue Interaction”, *Material Behaviour at Elevated Temperatures and Components Analysis, ASME Pressure Vessel and Piping Division, New York, Vol.60* pp. 71–79, 1982.

[91] R. Danzer: *Lebensdauerprognose hochfester metallischer Werkstoffe im Bereich hoher Temperaturen*, Gebrüder Bornträger, Berlin-Stuttgart, 1988.

[92] L. Coffin: “Fatigue at High Temperature - Prediction and Interaction”, *Proc. Instn. Mech. Engrs., 188* pp. 109–127, 1974.

[93] L. Coffin: “The Concept of Frequency Separation in Life Prediction for Time-dependent Fatigue”, *ASME–MPC Symposium of Creep-Fatigue Interaction, MPC-3* pp. 349–363, 1976.

[94] S. Manson, G. Halford and M. Hirschberg: “Creep-Fatigue Analysis by Strain-Range Partitioning”, *Design for Elevated Temperature Environment, ASME, New York* pp. 12–28, 1975.

[95] R. Viswanathan: *Damage Mechanisms and Life Assessment of High-Temperature Components*, ASM International, Metals Park, Ohio, USA, 1989.

[96] L. Kachanov: “On Creep Rupture Time”, *Izv. Akad. Nauk SSSR, 8* pp. 26–31, 1958.

[97] Y. Rabotov: *Creep Problems in Structural Members*, North Holland Publishing Co., Amsterdam, 1969.

[98] J. LeMaitre and J. Chaboche: *Mechanique de Materiaux Solides*, Dunod, Paris, 1985.

[99] S. Murakami: “Progress of Continuum Damage Mechanics”, *JSME Int.J., 30* pp. 701–710, 1987.

[100] S. Majumdar and P. Maiya: “Wave Shape Effects in Elevated Temperature Low-Cycle Fatigue of Type 304 Stainless Steel”, *Inelastic Behaviour of Pressure Vessel and Piping Components, PVP-PB-028, ASME* pp. 43–54, 1978.

[101] C. Jaske: “A Crack-Tip-Zone Interaction Model of Creep-Fatigue Crack Growth”, *Fatigue Engng. Mater. Struct., 6* pp. 159–166, 1983.

[102] C. Brinkman: “High-Temperature Time-Dependent Fatigue Behaviour of Several Engineering Structural Alloys”, *Int. Metall. Rev., 30* pp. 235–258, 1985.

[103] S. Majumdar and P. Maiya: “A Mechanistic Model for Time-Dependent Fatigue”, *J. Engng. Mater. Techn., 102* pp. 159–167, 1980.

[104] S. Majumdar: “Thermomechanical Fatigue of Type 304 Stainless Steel”, *Thermal Stress, Material Deformation, and Thermomechanical Fatigue, ASME, NJ* pp. 31–36, 1987.

[105] J. Chaboche: “Continuous Damage Mechanics - A Tool to Describe Phenomena before Crack Initiation”, *Nuclear Engng. and Design, 64* pp. 233–247, 1981.

[106] E. Renner, H. Vehoff, H. Riedel and P. Neumann: “Creep-Fatigue of Steels in Various Environments”, *Proc. Second Int. Conf. on Low Cycle Fatigue and Elasto-Plastic Behaviour of Materials, Elsevier, London* pp. 277–283, 1988.

[107] P. Grover and A. Saxena: “Characterization of Creep-Fatigue Crack Growth Behaviour in 2 1/4 Cr-1Mo Steel”, *Int. J. Fract., Vol. 73, 4* pp. 273–286, 1995.

[108] C. Laird and G. Smith: “Initial Stages of Damage in High Stress Fatigue”, *Phil. Mag.,8* pp. 1945–1963, 1963.

[109] J. Olschewski, R. Sievert and A. Bertram: “Aspects of High Temperature Deformation and Fracture in Crystalline Materials (JIMIS-7)”, *The Japan Institute of Metals, Nagoya* pp. 641–648, 1993.

[110] G. Wassermann: *Praktikum der Metallkunde und Werkstoffprüfung*, Springer, Berlin, Heidelberg, New York, 1965.

[111] U. Cocks: “Laws for Work-Hardening and Low-Temperature Creep”, *Transactions of the ASME* pp. 76–85, 1976.

[112] J. Estrin: “Stoffgesetze der plastischen Verformung und Instabilitäten des plastischen Fließens”, *VDI Forschungsheft, 642* pp. 1–48, 1987.

[113] G. Taylor: “The Mechanism of Plastic Deformation of Crystals, Part I”, *Tech. rep.*, Theoretical Proceedings of the Royal Society, A145, 1934.

[114] U. Essmann and H. Mughrabi: “Annihilation of Dislocations during Tensile and Cyclic Deformation and Limits of Dislocation Densities”, *Phil. Mag. A40* pp. 731–756, 1979.

[115] C. Teodosiu: “A dynamic Theory of Dislocations and its Application to the Theory of the elastic-plastic Continuum”, *Proc. Conf. Fundamental Aspect of Dislocation Theory, Washington 1969, Nat. Bur. Stand. and Special Publ. 317, vol. 2* pp. 837–876, 1970.

[116] J. Harder: *Simulation der Fließvorgänge in Polykristallen*, Ph.D. thesis, 1997.

[117] A. Ma, F. Roters and D. Raabe: “A Dislocation Density based constitutive Model for Crystal Plasticity FEM including geometrically necessary Dislocations”, *Acta Materialia, 54* pp. 2181–2194, 2006.

[118] S. Kalidindi, C. Bronkhorst and L. Anand: “Crystallographic Texture Evolution in Bulk Deformation Processing of FCC Metals”, *Journal of the Mechanics and Physics of Solids, Volume 40, Issue 3* pp. 537–569, 1992.

[119] A. Ma and F. Roters: “A constitutive Model for fcc single Crystals based on Dislocation Densities and its Application to uniaxial Compression of Aluminium single Crystals”, *Acta Materialia, 52* pp. 3603–3612, 2004.

[120] E. Nakamachi, N. Tam and H. Morimoto: “Multi-scale Finite Element Analyses of Sheet Metals by using SEM-EBSD measured crystallographic RVE Models”, *International Journal of Plasticity, 23* pp. 450–489, 2007.

[121] I. Carol, M. Jirašek and Z. Bažant: “A Thermodynamically Consistent Approach to Microplane Theory. Part I. Free Energy and Consistent Microplane Stresses”, *International Journal of Solids and Structures, 38* pp. 2921–2931, 2001.

[122] G. Taylor: "Plastic Strain in Metals", *J. Inst. Metals, 62* pp. 307–324, 1938.

[123] Z. Bažant and P. Prat: "Microplane Model for brittle plastic Material: Part I: Theory, Part II: Verification", *J. Engng. Mech., 114* pp. 1672–1702, 1988.

[124] I. Carol, Z. Bažant and P. Prat: "Geometric Damage Tensor based on Microplane Model", *J. Engng. Mech. 117* pp. 2429–2448, 1991.

[125] I. Carol, P. Prat and Z. Bažant: "New Explicit Microplane Model for Concrete: Theoretical Aspects and numerical Implementation", *Int. J. Solids Struct., 29* pp. 1173–1191, 1992.

[126] E. Kuhl, P. Steinmann and I. Carol: "A Thermodynamically Consistent Approach to Microplane Theory. Part II. Dissipation and Inelastic Constitutive Modeling", *International Journal of Solids and Structures, 38* pp. 2933–2952, 2001.

[127] J. Nemeček, B. Patzak, D. Rypl and Z. Bittnar: "Microplane Models: Computational Aspects and Proposed Parallel Algorithm", *Computers and Structures, 80* pp. 2099–2108, 2002.

[128] D. Raabe, F. Roters, F. Barlat and L.-Q. Chen: *Continuum Scale Simulation of Engineering Materials*, WILEY-VCH Verlag GmbH, 2004.

[129] S. Das, M. Abbod, Q. Zhu, E. Palmiere, I. Howard and D. Linkens: "A Combined Neuro Fuzzy-Cellular Automata based Material Model for Finite Element Simulation of Plane Strain Compression", *Comput. Mater. Sci.* 2007.

[130] E. Ising: "Beitrag zur Theorie des Ferromagnetismus (Contribution to the Theory of Ferromagnetism", *Zeitschrift für Physik, 31* pp. 253–258, 1925.

[131] R. Potts: "Some generalised order-disorder Transitions", *Proc. Cambridge Philosophical Society, 48* pp. 106–109, 1952.

[132] P. Rodriguez and K. Rao: "Nucleation and Growth of Cracks and Cavities under Creep-Fatigue Interaction", *Tech. rep.*, Indira Gandhi Centre for Atomic Research, Kalpakkam, India, 1992.

[133] K. Rao: *Influence of Metallurgical Variables on Low Cycle Fatigue Behaviour of Type 304 Stainless Steel*, Ph.D. thesis, University of Madras, India, 1989.